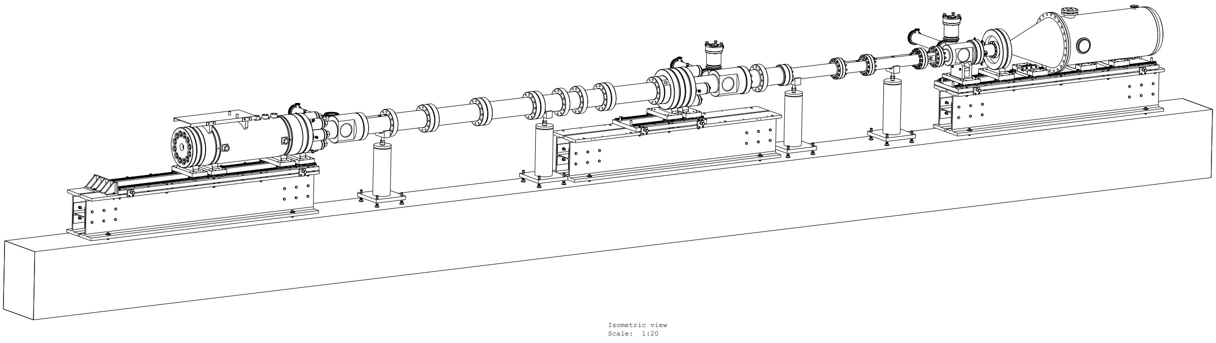

Performance design of hypervelocity shock tube facilities

Diana Zaida Felgueiras Luís

Thesis to obtain the Master of Science Degree in

Aerospace Engineering

Supervisor: Prof. Mário António Prazeres Lino da Silva

Examination Committee

Chairperson: Prof. Fernando José Parracho Lau
Supervisor: Prof. Mário António Prazeres Lino da Silva
Member of the Committee: Prof. Bernardo Brotas de Carvalho

September 2018

Dedicated to my parents and bother.

Acknowledgments

Firstly, to my supervisor, Professor Mário Lino da Silva, for introducing me to the fascinating world of atmospheric reentry and for giving me the opportunity to developed this work. Also, for his support and wise guidance.

To Fluid Gravity Engineering, for their support with the STAGG code and Alec Milne for providing his simplified wall drag theory.

To my parents, for their unconditional love and dedication. Thank you for helping me to follow my dreams around the world. And thank you for all the times you made me stop studying and go to sleep during the busiest times.

To my brother, for his support, advice, friendship and love. You have always been an inspiration and none of this would been possible without you.

To my grandparents, for being the most caring loving persons.

Finally, to my friends. Thank you for all the help and motivation during these last five years.

Resumo

Um tubo de choque cinético está em fase de qualificação no Instituto Superior Técnico, sob financiamento da Agência Espacial Europeia. O seu objetivo é estudar processos radiativos e de cinética química a alta velocidade, nas condições de uma entrada atmosférica.

Esta tese apresenta estimativas de performance para o tubo de choque ESTHER, em configuração mono e duplo- estágio. Para configuração mono-estágio, as velocidades até 8 km/s obtidas satisfazem os requerimentos para entradas em Marte, Titã e LEO. Para performances superiores, usa-se a configuração duplo-estágio que prevê atingir velocidades até 14.5 km/s, simulando missões de regresso à Terra e entradas em Vénus. No entanto, a configuração duplo-estágio tem dificuldade em atingir velocidades mais baixas e, como tal, para certas simulações deve recorrer-se a técnicas em que a performance da instalação é propositadamente degradada.

A exploração de planetas Gigantes Gasosos tem sido considerada um objetivo prioritário para futuros programas de exploração. No entanto, a reprodução das condições exatas de entrada atmosférica é extremamente difícil, devido à massa destes planetas. Considerando uma mistura H2/He, velocidades máximas de 18.4 km/s são previstas. Como tal, técnicas alternativas como alterar a fração de diluente de hélio e néon foram consideradas e verificou-se um aumento da temperatura pós-choque, o que permite reproduzir condições de entrada.

A combinação de altas velocidades com os curtos tempos de teste tornam essencial um sistema de deteção preciso. Este consiste em quatro sensores, uma placa FPGA de rápido desenvolvimento, um conversor ADC rápido e um sistema de condicionamento de sinal, detalhados nesta tese.

Palavras-chave: hipervelocidade, tubo de choque, performance, entrada em planetas, planetas Gigantes Gasosos, sistema de deteção

Abstract

A new kinetic shock tube is being commissioned at Instituto Superior Técnico under funding from the European Space Agency. Its main goal is to support planetary exploration missions, by studying high-speed radiative and chemical process kinetics relevant to planetary entries.

This thesis focuses on the performance estimates made for ESTHER shock tube in both single and double diaphragm configurations. For single diaphragm configuration, the predicted velocities up to 8 km/s satisfy the requirements for most Mars, Titan and LEO entries. For higher performance, using a double diaphragm configuration, ESTHER is expected to reach 14.5 km/s, simulating Earth return missions and Venus entries. However, double-stage configuration makes slower velocities difficult to achieve, thus some entries must be reproduced resorting to a few performance tweaking.

More recently, there has been renewed interest in exploring Gas Giants. However, experiments in ground facilities are difficult, due to high entry velocities imposed by their mass. When considering a H2/He mixture, velocities up to 18.4 km/s are expected to be achieved. Hence, alternatives as changing the helium and neon diluent fractions have been considered. These two changes increase the post-shock temperature, allowing important flight condition phenomena to be reproduced.

Combining the high velocities obtainable with the short test times, an accurate trigger system is essential. The ESTHER streak camera trigger system proposes the use of four sensors, a FPGA rapid development board, a FMC fast ADC converter and a signal conditioning system, which are discussed in detail here.

Keywords: hypervelocity, shock tube, performance, planetary entry, gas giants entry, trigger system

Contents

List of Tables

List of Figures

Nomenclature

Greek symbols

β	Parameter dependent on the boundary layer development layer.
χ	Molar fraction.
δ	Boundary layer thickness.
δ_r	Characteristic boundary layer displacement thickness.
γ	Ratio of specific heats.
μ	Viscosity.
ν	Kinematic viscosity.
ω_n	Cutoff frequency.
ρ	Density.
τ	Test time.
τ_w	Wall friction.
τ_{tr-int}	Characteristic relaxation time between the translational and internal modes.

Roman symbols

$\mathcal{M}$	Molecular weight.
$\mathcal{R}$	Ideal gas constant.
Re	Reynolds number.
A	Area.
a	Speed of sound.
C_f	Coefficient of friction.
d	Diameter.
E	Energy.

G	Universal gravitational constant.
g	Equivalent factor defined by Alpher and White.
h	Enthalpy.
L	Location of the Friedlander blast wave.
M	Mach number.
m	Mass
p	Pressure.
R	Specific gas constant.
r	Radius.
S_w	Momentum source term per unit length.
T	Temperature.
t	Time.
u	Velocity.
x	Length.

Subscripts

∞	Free stream conditions.
l_m	Development distance of the boundary layer.
t_d	Time onset of the Friedlander blast wave.
$v_{c,1}$	First cosmic velocity.
$v_{c,2}$	Second cosmic velocity.
0	Free stream conditions directly downstream of the shock wave.
1	Working tube initial state.
10	Tail of unsteady expansion driver gas state.
11	Driver tube initial state.
12	Nozzle gas state.
2	Post-shock state.
3	Unsteadily expanded test gas state.
3a	Unsteadily expanded test gas state for single diaphragm with variable area shock tubes.

3b	Steadily expanded test gas state for single diaphragm with variable area and convergent geometry shock tubes.
3b’	Steadily expanded test gas state for single diaphragm with variable area shock tubes.
4	Intermediate throat state/driver tube initial state for single diaphragm shock tubes.
5	Reflected gas state.
6	Intermediate post-shock state.
7	Intermediate pre-shock state.
8	Unsteadily expanded intermediate gas state.
9	Driver throat state.
e	Free stream conditions between the shock wave and the contact surface.
i	Ideal.
int	Internal modes.
r	Reflected.
s	Main shock conditions.
s7	Intermediate shock conditions.
sp	Species.
tr	Translational modes.
w	Wall

Acronyms

ADC Analog-to-Digital Converter

ADST Arc-Driven Shock Tube

AEL Arbitrary Euler Lagrangian

CARDC China Aerodynamics Research & Development Center

CEA Chemical Equilibrium with Applications

CFD Computational Fluid Dynamics

CFD zero-crossing Constant Fraction zero-crossing Discriminator

CS Contact Surface

CUBRC Calspan-University of Buffalo Research Center

DAC Digital-to-Analog Converter

DLR German Aerospace Center

DPP Digital Pulse Processing

EAST Electrical Arc Shock Tube

ECL Emitter-Coupled Logic

ESA European Space Agency

ESTHER European Shock Tube for High Enthalpy Research

FIRE Flight Investigation of the Reentry Environment

FMC FPGA Mezzanine Card

FPGA Field-Programmable Gate Array

GASL General Applied Science Laboratory

HEG High Enthalpy shock tunnel Göttingen

HIEST High Enthalpy Shock Tunnel

HVST HyperVelocity Shock Tube

IEAv Instituto de Estudos Avançados

IEPE Integrated Electronics Piezo-Electric

IPFN Instituto de Plasmas e Fusão Nuclear

ISRO Indian Space Research Organisation

IST Instituto Superior Técnico

ISTC International Science and Technology Center

IUSTI Institute Universitaire des Systèmes Thermiques Industriels

JAXA Japan Aerospace Exploration Agency

LENS Large Energy National Shock-tunnel

LEO Low Earth Orbit

MIPT Moscow Institute of Physics and Technology

NASA National Aeronautics and Space Administration

ONERA French Aerospace Lab

PCB Printed Circuit Board

PCIe Peripheral Component Interconnect express

PE Piezo-Electric

STAGG Shock Tube And Gas Guns

SW Shock Wave

TPS Thermal Protection System

TsAGI Central Aerohydrodynamic Institute

VKI Von Karman Institute for Fluid Dynamics

Chapter 1

Introduction

This chapter introduces the project. A basic contextualization of the topic is presented by discussing space exploration and detailing the characteristic of probes that entered the atmosphere of different planets at velocities over 6 km/s. The objectives of this thesis and a summary of each chapter are also be presented.

1.1 Motivation

In 1942, Germany launched a C2 rocket vertically and broke the 100 km altitude barrier, transcending the ”Kárman line” [1]. Since then, Space continues to capture the hearts and minds of many. The last five decades have witnessed close-up space exploration. People have been sent to the Moon and back during the Apollo program, capsules have entered on Venus, Mars, Jupiter and Titan, studying their atmospheres, the Habayusa probe has landed on an asteroid, taking a sample and bringing it back home, and after performing rendezvous with the 67P/Churyumov-Gerasimenko comet, a probe has landed on its surface, during the Rosetta mission [2]. Voyager spacecraft have been sent primarily to explore Jupiter and Saturn and their larger moons, but in August 2012, Voyager 1 made the historic entry into interstellar space, being currently much further away from the Earth and the Sun than Pluto [3].

The ability to provide simulations over planetary entry vehicles is essential to the success of the Solar System exploration. When dealing with an entry scenario, the flow is generally not simply hypersonic, but *hypervelocity*. According to Stalker [4]:

> *”’Hypervelocity’ is a term that was originally coined to describe flows that are both hypersonic and high velocity, rather than merely hypersonic, and it is used in that context here. Hypervelocity aerodynamics arose as a field of research in fluid dynamics when it became necessary to understand the aerodynamics of vehicles entering the Earth’s atmosphere. The velocities involved in such reentry maneuvers ensure that the enthalpy of air, after crossing the strong bow shock that is formed ahead of the vehicle, is sufficient to cause dissociation of the air molecules.”*

In a hypersonic flow field, a strong bow shock forms ahead of the forebody of the spacecraft and the flow field is hot enough for intermolecular collisions to cause the flow to dissociate and eventually ionize behind the bow shock. The shock heated gas transfers heat to the body by convection and radiation. While convection can be predicted well, radiation heating predictions still have uncertainties larger than 30% when using state-of-the-art models [5].

To tackle the challenges encountered during planetary entries and due to the extreme costs of performing flight experiments, combined efforts of computation simulations and experimental measurements are essential. Test facilities to simulate planetary entry generally either choose to simulate a scaled version of the real flight condition for a very short period of time or some specific phenomena of the real flight condition for a longer period of time.

Impulse facilities as shock tubes and shock tunnels are used for hypersonic and hypervelocity testing because, even if the test times are extremely short, they allow the stagnation enthalpy and Reynolds number of a true flight condition to be recreated. Arc-jets, plasma torches and plasma wind tunnels, although having a relatively low velocity, provide test times long enough for the test model to reach temperatures at which hot-wall and ablation tests can be performed.

To study high speed flows in excess of 10 km/s, the European Shock-Tube for High Enthalpy Research (ESTHER) is currently under the last phase of commissioning at Instituto Superior Técnico, Lisbon. This facility is a combustion driver shock tube, where research in plasma radiation of superorbital speed shocked flows will be carried to simulate the high pressure and temperature conditions of spacecraft entry in different atmospheres.

Recently, there has been renewed interest in future Jovian planets entry probes. Jupiter, Saturn, Uranus and Neptune are the giants of the Solar System and they define the dominant characteristics of the planetary system. They contain over 99% of the Solar System's mass and total angular momentum [6] and:

> *"The giant planet story is the story of the Solar System."* [7]

Future space missions to Uranus and Saturn have been identified as high priorities, by the United States National Research Council's survey *"Vision and voyages for planetary science in the decade 2013-2022"* [6]. However, entering the atmosphere of a Gas Giant is a challenging engineering problem. Entry speeds into the Gas Giants are of the order of 20-50 km/s [8], resulting in extreme heating environments in the shock layer. Nevertheless, Galileo probe has entered successively into Jupiter's atmosphere, in December 1995, with a velocity of 47.5 km/s [9].

1.2 Topic overview

Reentry vehicles designed for Space exploration are usually equipped with thermal protection systems made of ablative material. In order to properly model and predict the aerothermal environment of the vehicle, it is imperative to account for the gases presents in the planet atmosphere.

1.2.1 Atmospheric compositions

The Solar System planets fall into two categories: four small, rocky inner planets and four large, fluid, outer planets. The innermost planet, Mercury, possesses only a thin exosphere made up of atoms blasted off the surface by the solar wind and striking meteoroids. Mercury's exosphere is composed mostly of oxygen, sodium, hydrogen, helium and potassium [10]. The other inner planets - Venus, Earth and Mars - have substantial atmospheres, rocky surfaces and interiors that contain large abundances of heavy elements. Their atmospheres are geometrically thin, compared to the planetary radius [11].

The four outermost planets known as Gas Giants or Jovian planets - Jupiter, Saturn, Uranus and Neptune - have very deep atmospheres. This is primarily the result of being formed at a distance from the Sun where the temperature at the time of planet formation fell below the freezing point of water, allowing the rapid accumulation of mass as icy material [11]. These planets have become massive enough to attract and hold large quantities of the elements that remained gaseous, including the most abundant, hydrogen and helium.

Despite the diversity of planetary climates, the basic atoms are the same: hydrogen, oxygen, carbon and nitrogen. These elements are combined into compounds like oxygen (O_2), carbon dioxide (CO_2), nitrogen (N_2) and water (H_2O), in the inner Solar System, and hydrogen (H_2), methane (CH_4) and ammonia (NH_3), in the outer Solar System. The percentages of each compound of the inner and outer planets and their mean molecular weight are presented in tables 1.1 and 1.2, respectively.

The largest moon of Saturn, Titan, is an unique case of a moon in the Solar System with a thick atmosphere, composed by 98.5% nitrogen and 1.5% methane [12]. Its mean molecular weight can be assumed as 27.82 g/mol [13].

Table 1.1: Atmospheric compositions of the terrestrial planets (by volume), from NASA Planetary Fact Sheets [14]

Planet	% N_2	% O_2	% CO_2	% Ar	Trace components	Mean molecular weight (g/mol)
Venus	3.5	-	96.5	-	SO_2, Ar, H_2O	43.45
Earth	78.08	20.95	-	0.9	CO_2	28.97
Mars	2.7	0.13	95.32	1.6	CO, H_2O, NO	43.34

Table 1.2: Atmospheric compositions of gas giants terrestrial planets (by volume, uncertainties in brackets), from NASA Planetary Fact Sheets [14]

Planet	% H_2	% He	% CH_4	Trace components	Mean molecular weight (g/mol)
Jupiter	89.8 (± 2.0)	10.2 (± 2.0)	-	CH_4, NH_3	2.22
Saturn	96.3 (± 2.4)	3.25 (± 2.4)	-	CH_4, NH_3	2.07
Uranus	82.5 (± 3.3)	15.2 (± 3.3)	2.3	-	2.64
Neptune	80.0 (± 3.2)	19.0 (± 3.2)	1.5% (± 0.5)	-	$2.53-2.69$

1.2.2 Planetary entry speeds

The contrast in planetary masses leads to an order of magnitude range in atmospheric entry speeds, from 5 km/s to over 50 km/s [15]. For entries from circular orbits, the initial entry speed is in the order of the first cosmic velocity [16]. This first cosmic velocity is known as the orbital speed and it is given by

$$v_{c,1} = \sqrt{\frac{Gm_{body}}{r_{body}}}, \tag{1.1}$$

where G is the universal gravitational constant ($G = 6.67408 \times 10^{-11}$ m^{3}kg$^-$1s^{-2}) and m_{body} and r_{body} are, respectively, the mass and radius of the celestial body. The initial hyperbolic entry velocity is in the order of the second cosmic velocity, which corresponds to the velocity needed to escape from the gravitational field of a celestial body. This second cosmic velocity can be related to the first cosmic velocity by

$$v_{c,2} = \sqrt{2}v_{c,1}. \tag{1.2}$$

The results for the firsts cosmic velocities for the different Solar System bodies are summarized in table 1.3.

Table 1.3: First and second cosmic velocities, based on [14].

Celestial body	Mass (kg)	Radius (km)	First cosmic velocity ($v_{c,1}$, in km/s)	Second cosmic velocity ($v_{c,2}$, in km/s)
Venus	4.87e24	6052	7.33	10.36
Earth	5.98e24	6378	7.91	11.19
Mars	6.42e23	3394	3.55	5.03
Jupiter	1.90e27	71398	42.14	59.60
Saturn	5.69e26	60300	25.09	35.48
Titan	1.34e23	2574	1.87	2.64
Uranus	8.68e25	25559	15.06	21.29
Neptune	1.02e26	24300	16.74	23.67

However, according to previous missions and the literature, Venus yields a minimum entry speed of about 11 km/s [15]; Earth's reentry speeds can vary between 7.8 km/s for entries from low Earth orbit (LEO) and 12.9 km/s achieved by the Stardust capsule [17], the fastest up to date. Mars although being slightly more distant from Earth than Venus's, has a much smaller mass, thereafter, Martian atmospheric entry speeds are much slower than at Venus, begin around 5.7 km/s [18].

Jupiter entry speeds can vary between 47.3 km/s (equatorial orbit, in prograde direction) to 71.5 (from an equatorial orbit, in retrogade direction) [19]; Saturn and Uranus proposed entry speeds are around 27 km/s [20] and 22.3 km/s [21] and Neptune entry speeds are up to 34 km/s [18]. Titan's relatively low mass contributes to lower entry speeds possibly as low as 5 km/s [15].

Thereafter, comparing the proposed entry speeds with the cosmic velocities, the latter are slightly underestimated.

1.2.3 Hypervelocity space capsules for planetary entry

When designing space capsules for planetary entry, an understanding of the aerothermodynamics behind the body in various atmospheres is essential. Usually, these probes travel at hypervelocity and are shaped as blunt bodies to reduce excessive heating rates.

Blunt body vehicles are comprised of a large heat shield, usually a high temperature insulator or an ablative material [22], that protects a smaller crew cabin or robotic probe payload from the high levels of heating encountered during atmospheric reentry. The geometry of the heat shield produces large amounts of aerodynamic drag that decelerate the vehicle from orbital or interplanetary speeds [22]. Blunt bodies also have detached shock waves that spread the heat of reentry over a relatively large volume. The air flow near the surface of blunt vehicles tends to inhibit convective heat transfer and, thus, the heating rate for blunt vehicles is relatively low [23].

A brief overview of the planetary mission entry vehicles that reached orbital or superorbital velocities during reentry and their scientific objectives is discussed below.

Project FIRE (Flight Investigation of the Reentry Environment) was undertaken by NASA to investigate the heating environment of vehicles entering Earth's atmosphere at Lunar return velocities [22]. The second and final flight was successfully conducted in 1965 with ballistic reentry (zero angle of attack) occurring at a velocity of 11.35 km/s.

The FIRE II flight vehicle (figure 1.1) was an Apollo-type geometry with three layers formed by phenolic-asbestos heat shield sandwiched between beryllium calorimeters [24]. The first heat shield had a nose radius of 0.935 m and a diameter of 0.672 m [25]. The 66° angle conical afterbody section was made of a fiberglass shell supporting the heat shield [26].

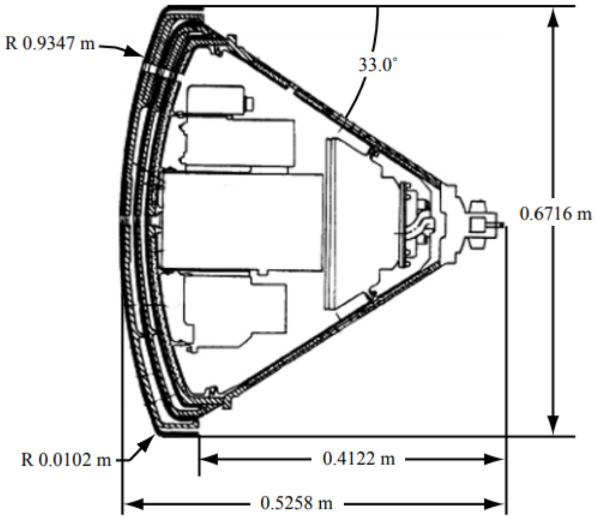

Figure 1.1: Geometry of the Fire II capsule, extracted from Liechty et al. [27].

In 1959 the Apollo program began sponsoring several dedicated flight tests to study the heating environment of orbital and superorbital entry probes. Once the design of the Apollo Command Module was decided, four flight tests were conducted. Apollo missions AS-201 and AS-202 were designed as high heat rate and heat load tests [28] and reentered Earth's atmosphere in 1966, at velocities of

7.67 km/s and 8.29 km/s, respectively [29]. Apollo 4 and Apollo 6 were primarily intended to perform qualification tests for the heat shield [28] and to qualify the entry system for Lunar return by entering at an angle of attack of 25°. The entry velocities were 10.73 km/s and 9.60 km/s, respectively, in 1967 and 1968 [30].

The Apollo entry configuration was a blunted cone with a spherical segment base. The forebody consisted of a spherical section with a radius of 4.694 m and the afterbody consisted of a 33° conical section, blunted to a 0.231 m radius at the aft end. The maximum diameter of the capsule was 3.912 m [29]. Both forward and aft heat shields were continuous structures coated with an ablative material and the central heat shield (crew compartment) consisted of a series of externally applied segments which were mechanically fastened to the primary structure [28].

The Command Module was an axisymmetric vehicle with the center of gravity offset from the body axis [31], due to variations in the thickness of the aft heat shield ablative coating [28]. This arrangement produced the amount of lift necessary to ensure a sufficiently wide entry corridor and to exercise control of the landing point. The blunted design produced the amount of drag necessary to efficiently dissipate the kinetic energy [32].

Between late 1960's until early 80's, the Soviet space program launched several Venera missions to Venus. The objectives of the missions were to return data from the Venusian atmosphere, to make a landing on the surface and to continue to return data after landing [33]. In October 1967, Venera 4 successively entered the Venusian planet, with an entry velocity of about 10.7 km/s [34]. This was the first man-made object known to have landed on any planet, even though it was no longer operational. Venera 7 reached Venus in December of 1970, becoming the first spacecraft to return data (including pictures of the planet surface, among other things) after landing on another planet [33].

Venera 4 had a different thermal control system to avoid the overheating problems of the type experienced by Veneras 2 and 3. The landing probe weighted 383 kg and had a glass-fibre/polymer heat and a double parachute system to enable it to soft-land on the surface of Venus [34]. This capsule was also designed to float in the hypothesis of Venus having a liquid surface.

In 1978, NASA launched the Pioneer Venus probe spacecraft to explore the atmosphere of Venus. The main objective was to investigate the solar wind, map the surface through a radar imaging system and study the characteristics of the upper atmosphere and ionosphere [35].

The Pioneer Venus consisted of two vehicles: the Orbiter and the Multiprobe. The Orbiter was launched in May 1978 and was inserted in a elliptical orbit around the planet, in December 1978 [36], investigating the plasma and observing reflected sunlight from the cloud layers at a variety of wavelengths [35, 37]. The Pioneer Venus Multiprobe was launched in August 1978 and was composed by 5 separate probes: the probe transporter, referred to as the Bus; a large atmospheric entry probe, Sounder; and three small probes [35]. The large and the three small probes entered the planet in December, 1978, nearly simultaneously at widely dispersed points above the planet: two small probes entered on the nightside and one small and the large probe entered on the dayside of the planet [38]. The three small probes entered the atmosphere with a velocity of 11.54 km/s [39].

The large probe, Sounder, was 1.5 m in diameter [38] and comprised a spherical pressure vessel, a forward aeroshell heat shield and an aft cover [36]. The blunt cone-shaped aeroshell had a heat shield made of ablative carbon phenolic coating [38]. The probe entered the planet at about 11.5 km/s near the equator being decelerated by a deployed parachute [36], in order to have a descent rate consistent with the small probes [40].

The three small probes were identical to each other and were designated North Probe, Night Probe and Day Probe. These probes consisted of spherical pressure vessels surrounded by a forward conical heat shield and afterbody. The aeroshell was a 45° blunt cone made of titanium which used a bonded carbon phenolic ablative coating as a heat shield. The probes had a mass of 90 kg and a diameter of 0.8 m [41].

In October 1989, the Galileo project was launched. Its purpose was to conduct a comprehensive exploration of the Jovian system, including remote observations of the planet and its satellites by an orbiting vehicle and to make direct measurements of the characteristics of the Jovian atmosphere by the entry probe [42]. Besides, it became the first spacecraft to visit asteroids and the only to provide direct observations of a comet colliding with a planet. Throughout its Venus flyby, in February 1990, it also captured infrared images of the Venusian clouds [43].

The Galileo consisted of two vehicles: an orbiter and an atmospheric probe. The orbiter was the first spacecraft to be placed into Jupiter's orbit. The probe was released from the orbiter in July 1995 and entered Jupiter's atmosphere in December 1995, in the same direction of the planetary rotation, in order to lower its relative entry speed to 47.5 km/s [9].

The probe was 1.25 diameter and 0.86 m in height [44] and was composed by two major segments: a deceleration module and a descent module. The deceleration module consisted of the fore and aft heat shields and the thermal control hardware needed during atmospheric entry. The ablative forebody heat shield was made from a carbon phenolic material and the afterbody heat shield was composed of a phenolic nylon material [44], protecting the 45° blunted-cone probe [9].

Mars Pathfinder was launched in December 1996 and landed on the surface of Mars in July 1997 [45]. Pathfinder primary objective was to demonstrate a low-cost, reliable system for entering the Martian atmosphere and placing the first robotic rover to the surface of the planet [46]. The spacecraft entered Mars atmosphere directly from the interplanetary transfer trajectory with an inertial speed of 7.26 km/s [47].

The Pathfinder aeroshell consisted of a forebody heat shield and an aft body backshell. The aeroshell diameter was 2.65 m and the forebody shape was a 70° half-angle sphere–cone with a nose radius of 0.6638 m and a shoulder radius of 0.0662 m. The forebody ablative material was a super lightweight ablator and the backshell was thermally protected with the spray-on version of the same material [47].

In October 1997, Cassini-Huygens was launched, arriving at Saturn in July 2004 [48]. In December 2004, the Huygens probe was separated from the Cassini spacecraft [49] and one month later, the probe entered Titan's atmosphere at a velocity of 6.2 km/s [39]. This mission was designed to explore the Saturnian system and, by entering and descending Huygens into Titan's atmosphere, to study Saturn's largest moon.

The Huygens probe was a 6° half-angle sphere-cone with a nose radius of 1.25 m, a diameter of

2.7 m [50] and weighted around 318 kg [48]. The forebody heat shield thermal protection system was composed of a blend of silica fibres reinforced by phenolic resin [50].

In February 1999, the Stardust was launched to collect samples of dust and gases, while doing a close flyby to comet Wild-2 [51] and then it returned back to Earth. In January 2006, the entry capsule was released from the main spacecraft and reentered Earth's atmosphere at 12.9 km/s, being the fastest Earth reentry capsule until date [17].

The Stardust capsule was approximately 0.8 m in diameter with a 60° half-angle sphere cone for the forebody heat shield and a 30° truncated afterbody cone. Its heat shield was composed by phenolic impregnated carbon ablator instead of traditional carbon phenolic due to its lower weight [51].

In August 2001, the Genesis spacecraft was launched to collect solar wind samples from the Sun-Earth Lagrange point, L1, and to return them to Earth for analysis. In 2004, after completing its sampling phase, the spacecraft released its sample return capsule, which protected the science canister from the extreme aerothermodynamic heating during reentry: it was a 60° half-angle blunt cone constructed from phenolic impregnated carbon ablator - as for the Stardust capsule - and the backshell was covered with a super lightweight ablator material [52]. The Genesis return capsule reentered Earth's atmosphere at a velocity of 10.8 km/s [39].

Hayabusa was an asteroid exploration mission launched in August 2003 and the first mission to return a sample of material from the surface of a near-Earth object. In November 2005, the Hayabusa spacecraft retrieved a sample from Itokawa asteroid [53] and in January 2010, the sample return capsule was released from the main spacecraft, performing a ballistic reentry into Earth's atmosphere at a velocity of 12.04 km/s [54]. During reentry, the sample return capsule was also used to characterize the aerothermodynamic environment with time-resolved measurements of optical emission, shock-heated gases ahead of the capsule and the trailing wake [54]. Hayabusa's sample return capsule was a 45° sphere cone with a diameter of 40 cm and its thermal protection system was made entirely of carbon phenolic [53].

1.3 Objectives

As discussed before, most of the missions sent to celestial bodies have as a primary objective the study of the atmosphere for the planet of interest. However, while preparing such missions, ground tests are essential to ensure their success, namely during the most complicated phase: atmospheric entry.

The overall aim of this thesis is to estimate the performance of the new European Shock-Tube for High Enthalpy Research (ESTHER). The specific objectives are:

1. Simulating entry conditions for different planetary atmospheres.
2. Investigating the possibility of tweaking gas composition to achieve higher post-shock temperatures within the ESTHER facility.
3. Elaborating $x - t$ diagrams to analyse the interaction of the shock wave with the expansion waves and verify the location and time of the formation of a blast wave.

4. Implementing a wall loss algorithm to estimate the losses expected to occur for the different simulations.
5. Predicting the rise time and attenuation of a signal using the trigger system specific tailored for hypersonic regimes in the ESTHER shock tube.

1.4 Thesis outline

This thesis is organised as follows:

Chapter 2 provides a brief introduction of the ground facilities used to study aerothermodynamics of hypervelocity flows. It also discusses the facilities available worldwide for reaching superorbital and orbital velocities and briefly mentions the facilities that simulate suborbital velocities. Finally, a brief comparison between the performances of different facilities over different atmospheres is also presented.

Chapter 3 presents the underlying theory of ideal shock tubes. Equations governing single and double diaphragm shock tube flows with constant and variable area ratios are summarized. Disturbance effects, such as blast wave formation, wall boundary layer effects and diaphragm rupture time are also addressed.

Chapter 4 provides a detailed study on the ideal aerodynamic design of the ESTHER shock tube. Results for different test atmospheres are then presented, taking into consideration disturbance effects. Gas substitutions to simulate Gas Giants's entry conditions at lower shock speeds are also studied. Finally, the facility performance and its limitations are discussed, by analyses of the shock tube performance envelopes.

Chapter 5 presents a review of the initial trigger system for the facility and its drawbacks. The updated trigger system to be implemented on ESTHER shock tube is then explained and the algorithm is implemented into a representative signal from an expansion tube.

Chapter 6 provides the conclusions and achievements of this thesis and recommendations for future work.

Chapter 2

Hypervelocity facilities outlook

Space travels between our planet Earth and outer Space remain the pinnacle of exploration. Many unmanned missions have been sent to orbit, have traversed the atmosphere or landed on the surface of celestial bodies and some have even crossed the border of the solar system with no expectation of return. Nevertheless, many missions are designed to return to Earth, carrying either humans or scientific payload from Space.

To ensure the success of such missions, the flow environment must be simulated using CFD codes and validated against ground facilities testing. This chapter explains the type of hypervelocity shock tube facilities available worldwide, their configurations and what they are typically used for.

2.1 Ground facilities

For most of the planetary exploration missions, high flow speeds, high enthalpy chemical kinetics and plasma radiation effects are key to study the aerothermodynamics of hypersonic flows. Depending on the type of phenomena or the processes to be analysed, these conditions may be simulated using shock tubes, shock tunnels or expansion tubes, which must be able to generate non-equilibrium flows.

The first shock tube was constructed by Vieille [55], while studying combustion and detonation in tubes. In a shock tube, after the rupture of the diaphragm, a shock wave is generated. This wave accelerates the test gas and its temperature, pressure and density change abruptly. Therefore, physical and chemical processes can start and evolve to their equilibrium state [56].

Shock tubes have the indisputable advantage of generating the faithful post-shock conditions of planetary entries. Shock tube experiments generally monitor radiative emission/absorption to infer the properties of the shocked flow. However, as reported by Mirels [57, 58], due to low density effects, the separation between the moving shock wave and the contact surface travelling behind significantly decreases with pressure, which makes it difficult to establish flows over test models.

Shock tunnels make use of the shock tube capability of compressing and heating the test gas, but a nozzle is added at the end of the shock tube. At the exit of the divergent part of the nozzle, the flow becomes hypersonic at low temperature. Thus, to simulate real flight conditions by generating hypersonic flows around bodies, shock tunnels may represent an appropriate choice [56]. However, both reflected and non-reflected shock tunnels are limited in the stagnation enthalpy that can be simulated due to the energy added to the flow across a shock wave. This is because at very high shock speeds, the flow exists as a highly dissociated plasma, which is useful to study plasma and blunt body heat transfer behind shock waves but not for aerodynamic testing. Such facilities are generally limited to Earth orbit velocities and below [59].

The expansion tube was first proposed by Resler and Broxsom [60] in the 1950's and has the configuration of a conventional shock tube with addition of an expansion section attached at the downstream end of the driver tube, containing an acceleration gas [61]. After initial shock processing of the test gas in the shock tube, an unsteady expansion fan adds more energy to the final test flow, therefore the kinetic energy of the gas is increased while the temperature of the gas remains relatively low [62]. This type of facility is to be used to generate very high Reynolds number flows since the flow is never stagnated [62], which reduces dissociation and ionization [63]. However, this has the disadvantage of having much shorter test times and developing large boundary layers in the resulting test flow [63].

Another type of ground testing facilities used to study hypersonic phenomena are generally relatively low velocity and long duration, such as arc-jets, plasma torches and plasma wind tunnels. These are high enthalpy test facilities which have test times long enough for the test model to reach temperatures at which hot-wall and ablation tests can be performed. However, while they can recreate flow stagnation enthalpy, they cannot recreate the velocity, or the other upstream properties of a real entry flow field.

The following review focuses primarily on the worldwide facilities used to investigate chemical kinetics and radiation absorption and emission, such as encountered during atmospheric reentry at superorbital velocities. Other facilities capable of reaching orbital and suborbital velocities will also be mentioned. A global outlook of all available hypersonic facilities is presented in figure 2.1.

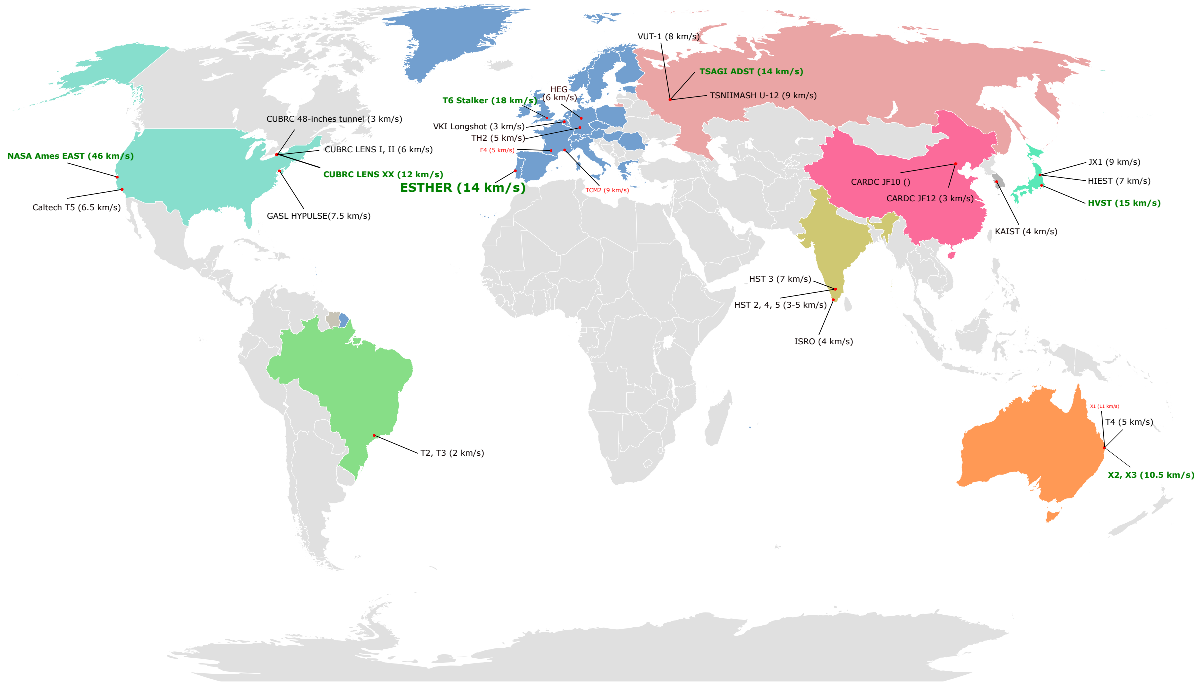

Figure 2.1: World outlook of hypersonic facilities.

2.1.1 Superorbital flows facilities

Superorbital velocities are arbitrarily considered here as capable of exceeding 10 km/s. Currently, the only facilities able to reach these velocities are: Ames EAST shock tube (U.S.A.); X2 and X3 expansion tubes (Australia); CUBRC LENS XX expansion tube (U.S.A.); HVST shock tube (Japan); and TsAGI ADST shock tube (Russia). In Europe, two hypervelocity facilities are currently being developed and constructed: the ESTHER shock tube (Portugal) and the T6 Stalker tunnel (United Kingdom).

Built in 1965, the Ames Electric Arc Shock Tube (EAST) is the only shock tube in the United States capable of simulating shock-heated gas environments at very high enthalpies (reservoir enthalpy is up to 29 MJ/kg [64]). This facility is used to investigate the effects of radiation and ionization associated with the shock waves encountered during atmospheric reentry [65].

The EAST assembly (figure 2.2) consists of three primary components: the driver section; the driven tube; and the dump tube & dump tank. The driver and driven section are separated by the main diaphragm. At the first section, the driver gas is heated within a confined space, using an electric discharge (arc) struck inside the driver. Consequently, the pressure increases, causing the burst of the aluminium diaphragm [66]. After diaphragm rupture, a shock wave propagates into the driven tube and an expansion fan propagates upstream into the driver gas. When the shock wave reaches the end of the driven tube, it bursts the downstream thin aluminium foil diaphragm [65] and the pressure differentials between the driven tube and the dump tank forces the gas to move into the dump tube and be held in the dump tank. Posteriorly, the dump tank is vented to the atmosphere.

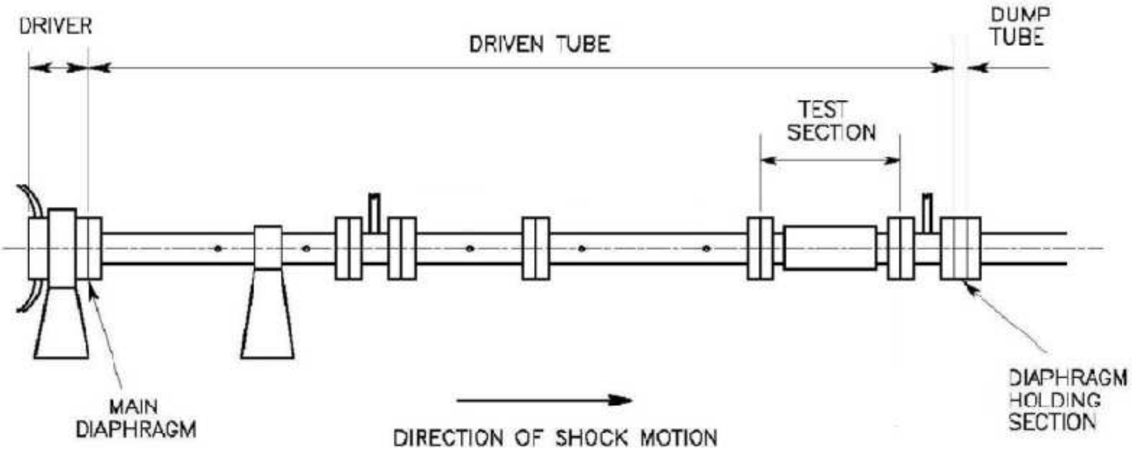

Figure 2.2: Schematic view of EAST facility at NASA Ames Research Center, adapted from [67].

The driver chamber is 26.4 cm long and the driven section consists of a 10.16 cm diameter and 9 m length aluminium tube. Attached is the dump tube that consists of an aluminium tube with 7 m length and 10.16 cm diameter [66]. The arc discharge driver can generate temperatures above 10 000 K for much less than one millisecond [64], resulting in shock waves that can reach speeds up to 46 km/s [66], depending on the initial operating conditions. An inconvenient of this high energy driver is the poor shot reproducibility, since electrical arcs are inherently unstable by nature and difficult to reproduce in the same exact conditions.

In Australia, the University of Queensland hosts several hypersonic facilities. However, only the expansion tubes X1, X2 and X3 can reach superorbital velocities.

Similarly to Ames EAST, the X1, X2 and X3 expansion tubes comprise three primary structural assemblies: a free piston driver; a driven tube, divided into sealed compartments as the secondary driver, shock tube and acceleration tube; and the test section & dump tank [68]. The first contains a heavy piston, inside a large diameter steel compression tube. Initially, a light gas at low pressure fills the volume between the piston and the steel diaphragm and behind it, the reservoir is filled with a large volume of high pressure air. By compressing the light gas, the diaphragm ruptures and a strong shock wave is produced. That shock wave travels through the shock tube, placed downstream of the steel diaphragm, compressing and accelerating the test gas until it reaches the second diaphragm, which ruptures easily: this diaphragm is only strong enough to maintain the initial pressure difference between the two tubes. Then, the shock wave propagates into the acceleration tube, downstream of the tertiary diaphragm, at a faster speed due to its lower density medium [69]. Immediately downstream of the driven tube exit, the test section where the experiments occur is placed. The dump tank is used to store the gases that are generated during the experiment.

In 1987, the small shock tunnel, TQ, was converted to an expansion tube and renamed X1. This X1 free piston driven expansion tube used multiple diaphragm sections [69]. The acceleration tube diameter was 38 mm and the test time was limited to the order of tens or hundred of microseconds [70]. This facility could reach up to 10.8 km/s in air [71] but due to its very short test time, larger facilities were projected and X1 was decommissioned in 2011 [72].

The X2 free piston driven expansion tube (figure 2.3) was commissioned in 1995 [69]. It is a 23 m long facility and its driven tube has 85 mm diameter, which allows experiments in larger models. This facility is primarily used to study radiative heating during atmospheric reentry, being capable of reaching 10.3 km/s in air and having a test time of about 50 ms [64].

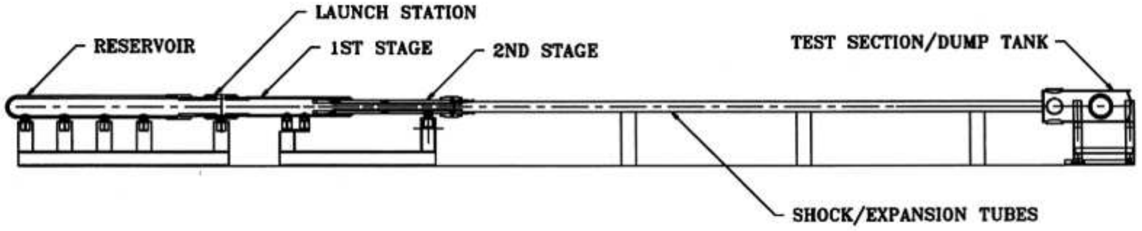

Figure 2.3: Schematic view of X2 expansion tube at University of Queensland, extracted from [73].

The X3 facility (figure 2.4) was originally commissioned in January 2001 and is a large superorbital free piston driven expansion tube. The total length of the facility is 69 m, comprising a 14 m compression tube, 10 m driven tube, 12 m secondary driver, 25 m acceleration tube and a 2 m test section. The exit diameter of the acceleration tube is 182.6 mm. The dump tank has a length of 5 m and 1.2 m diameter [69]. This facility has a running time of 1 ms and the flow speed can reach 10 km/s in air, with stagnation enthalpies up to 100 MJ/kg [74].

Another American hypersonic facility is the Large Energy National Shock Tube (LENS), from the Calspan-University of Buffalo Research Center (CUBRC). CUBRC operates four tunnels in the LENS

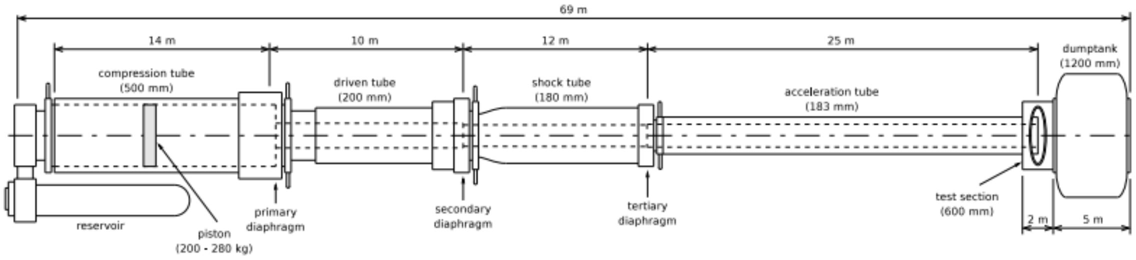

Figure 2.4: Schematic view of X3 expansion tube at University of Queensland, extracted from Jacobs et al. [69].

supersonic and hypersonic ground test complex: a 48-inch shock tunnel; two short duration, high enthalpy shock tunnels, LENS I and LENS II; and an expansion tunnel called LENS XX, which is the only of the four capable of simulating hypervelocities. The construction of the latter was completed in 2009 [75], providing a research and testing capability for investigating real gas effects, shock layer chemistry, viscous interactions and ablation effects on the performance of hypervelocity vehicles [76].

The LENS XX expansion tube is comprised of the driver, driven and acceleration tubes and a downstream test section. A test shot proceeds as follows: the driver section is electrically heated [75], which increases the gas pressure, rupturing the first diaphragm. At this point, the test gas is accelerated by a shock wave, breaking the second diaphragm. This gas is further accelerated through an unsteady expansion in the acceleration tube, reaching velocities up to 12.2 km/s [77]. This facility is considered the largest known expansion tunnel in the world with a length of more than 73 m and a inner diameter of 10.16 cm, and a nozzle expansion into a 2.4 m test section [75].

The Japan Aerospace Exploration Agency (JAXA) currently operates the HyperVelocity Shock Tube (HVST), a free piston double diaphragm shock tube, investigating thermochemical nonequilibrium phenomena [78] and, particularly, radiation emitted from the highly heated region, behind the shock wave [64]. This shock tube is composed of five sections: an air reservoir; the free piston compression tube; a high and a low pressure compression tubes; and a vacuum tank. The reservoir can be filled with air up to 0.98 MPa [78].

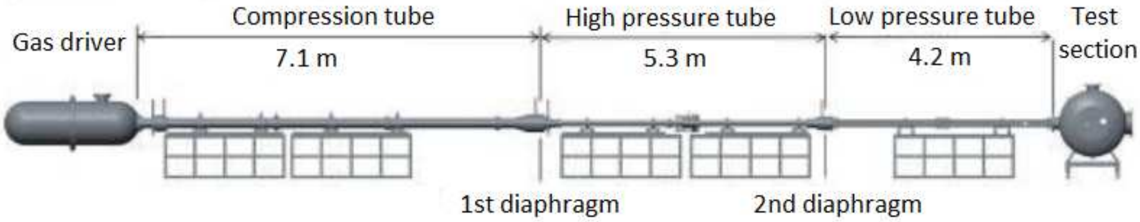

Figure 2.5: Schematic view of HVST facility at JAXA, adapted from Nomura et al. [79].

Similarly to the expansion tubes from Australia, the compressed air in the reservoir forces the free piston to move down the compression tube, compressing the driver gas. This compression tube is separated from the high pressure tube by the first diaphragm, that breaks once it reaches its rupture pressure. At that moment, a shock wave is generated and propagates in the high pressure tube. Once it reaches the end of that tube, the shock wave is reflected and the second diaphragm ruptures, generating a stronger shock wave in the low pressure tube.

HVST has about 23 m length. The compression tube has 5.1 m length and 15 cm diameter. The high pressure tube has a length of 4.7 m and a round cross section with 8 cm diameter. Differently from the other tubes composing this facility, the low pressure tube has a square cross section with 7 cm side and 4.175 m length and is made of aluminium alloy to reduce emissions from impurities [78]. This facility can reach up to 15 km/s in air [80].

In Russia, the Central Aerohydrodynamic Institute (TsAGI) hosts the ADST shock tube, an arc-driven shock tube, whose configuration and current status are unknown. Based on the results obtained from the ISTC project, this facility allows the investigation of ionization and radiation processes behind a shock wave in air in the range of 8 to 14 km/s [81]. It may also be used to measure electron concentration and temperature behind a shock wave and radiation intensity [71].

Currently a new kinetic shock tube is being developed at Instituto Superior Técnico (IST), Lisbon, under funding of the European Space Agency (ESA). The European Shock Tube for High Enthalpy Research (ESTHER) is being developed to study radiation and chemical kinetics relevant to planetary entries [82]. This shock tube (figure 2.6) is a piston-free combustion driver section at initial pressure up to 100 bars and a final pressure of 600 bars [83]. An intermediary compression tube is connected to the combustion chamber through a primary diaphragm, which will be filled with helium gas at pressures between 0.01 bar and 1 bar [83]. The compression tube is connected to the shock tube test section through a secondary diaphragm. The latter will be filled with a test gas at pressures of about 0.1 mbar [83]. A dump tank will recover all the gases flowing in the wake of the shock wave.

The combustion chamber is 1.6 m in length with an internal diameter of 200 mm and is made in low carbon super-duplex steel [83]. The compression tube is 5 m long and has an internal diameter of 130 mm. Its end sections manufactured in super-duplex stainless steel [83], which also has a low carbon content, limiting adsorption. The shock tube section has 4 m length from the secondary diaphragm to the window and an internal length to the dump tank of 5.4 m [82]; an internal diameter of 80 mm and is also made in duplex stainless steel [83]. As discussed in this work, this facility is expected to simulate flows up to 14 km/s in air.

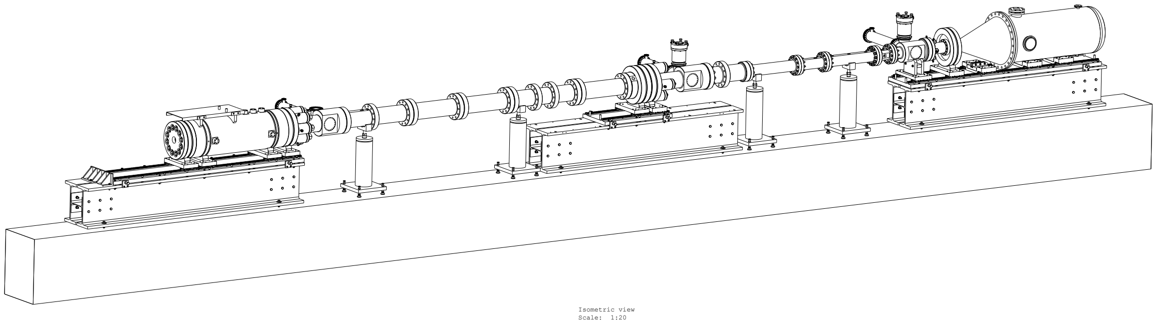

Figure 2.6: Isometric view of ESTHER shock tube at IST.

Another ground test facility is likewise under development in Europe. The T6 Stalker tunnel (figure 2.7) has been a joint collaboration between the University of Oxford and the University of Queensland

Centre for Hypersonics. The tunnel is formed by coupling the decommissioned T3 free piston driver to the barrels, nozzle and test section of the Oxford Gun Tunnel. The result is a facility that allows operations as either a reflected shock tunnel, an expansion tunnel (both of which for testing models) or as a shock tube, for shock layer radiation studies [84].

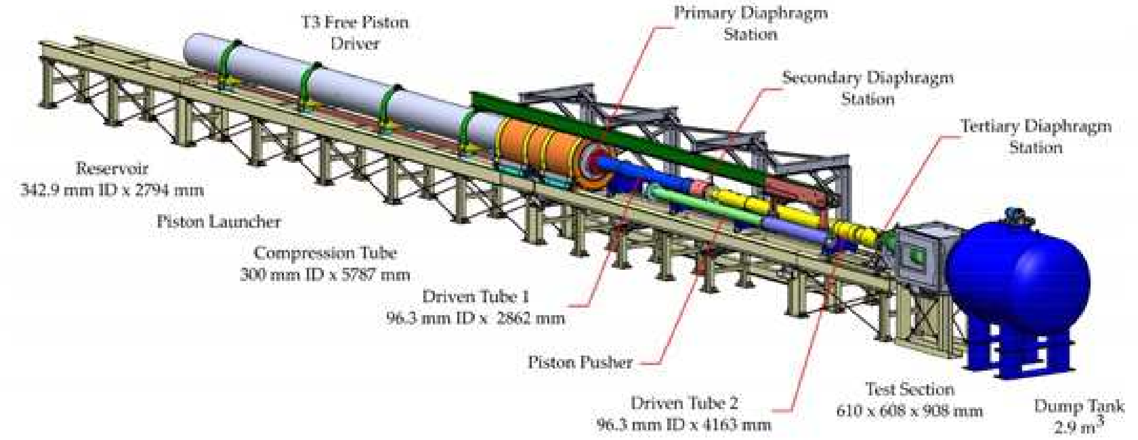

Figure 2.7: Schematic view of T6 Stalker tunnel, extracted from [85].

A Stalker free piston driver is advantageous as it creates the heated gas using a transient compression process [86], thus containment of the high pressure and temperature gas is required for only a very short time, reducing the mechanical and thermal design constraints. The driver gas is compressed via a free piston stroke to the rupture of the primary diaphragm. The driver section has a length of 6.0 m and a diameter of 300 mm. The driven part of the tunnel consists of two driven tubes, the first with 1.75 m length and the second with 4.24 m. Both have the same diameter of 96.3 mm [84].

For speeds in the range of $2-6$ km/s, the facility may be operated in reflected shock tunnel mode. Above 6 km/s, it can be operated as an expansion tunnel and this last mode is capable of reaching speeds up to 15 km/s [84]. The shock tube mode may be used for tests that require longer flow durations at speeds above 4 km/s but cannot accept a test fas that is chemically contaminated. This shock tube configuration is claimed to be able to generate shock speeds up to 18 km/s [84].

2.1.2 Orbital flows facilities

There are other facilities spread around Europe, America and Asia, which are capable of reaching orbital velocities, within 6 to 10 km/s. These will be briefly mentioned hereafter.

In 1956, the U-12 shock tube was installed at the Central Research Institute of Mechanical Engineering, Japan. This facility was designed to investigate aerophysics, physico-chemical kinetics, shock wave processes and aerodynamics [87]. The speed achievable by the shock waves can be up to 9 km/s [64].

Since 1990, Caltech operates the T5 facility, a free piston shock tunnel [88]. Its purpose is to generate very high enthalpy flows at high density to simulate chemical nonequilibrium effects encountered in the aerodynamics of transport vehicles to and from space [88]. This facility can generate shock waves with velocities up to 6.5 km/s [64].

The German Aerospace Center (DLR) HEG shock tunnel was commissioned in 1991 [89] and is currently the only operative European facility capable of reaching orbital velocities. HEG is a free piston driven shock tunnel for simulations of entry flows up to 6 km/s and may simulate flows within a wide range of altitudes [90]. This facility was designed to study the influence of high temperature effects such as chemical and thermal relaxation on the aerothermodynamics of entry vehicles [89]. However, in Europe, most of the available data on radiation has been obtained using the TCM2 free piston shock tube from IUSTI Marseille. This facility was built in 1992 and was the only European facility capable of performing experiments on chemical kinetics and thermal relaxation for planetary entries, expected to produce shock velocities in the range of 2-9 km/s [91]. TCM2 was decommissioned in 2006, for safety reasons, after breaking when testing superorbital reentry conditions at just over 9 km/s [81], consequently stopping shock tube reentry activities in Europe.

Since its construction in 1992, LENS I has been used to study aerothermal and aero-optical phenomena associated with the design of missiles, capsules and screamjet propulsion vehicles. This facility is capable of evaluating viscous interaction and real gas phenomena over hypersonic vehicles in high Mach number and low Reynolds number range. CUBRC LENS I can reach velocities up to 6 km/s [77].

Another American facility is the GASL HYPULSE facility, from NASA, operating as a reflected shock tunnel, since 1996 [92]. This facility was designed to study the development of hypersonic combustion technology and real gas effects in reentry aerodynamics [93]. GASL HYPULSE has produced flows with velocities up to 7.5 km/s [94].

In 1998, the JF-10 detonation-driven high enthalpy shock tunnel was installed in the Institute of Mechanics, Chinese Academy of Sciences, Beijing, for exploring reentry physics [72]. Since the same year, JAXA operates the free piston high enthalpy shock tunnel HIEST, at Kakuda Space Center, Japan. This facility aims at producing high-fidelity aerodynamic data for design of lifting reentry vehicles [95], investigating boundary layer transition over reentry capsule models and performing aeroheating studies [96]. HIEST can test flows up to 7 km/s [64]. Around 2000, the JX-1, a free piston driven expansion tube was installed at Tohoku University, Japan, to produce hypervelocity flows, reaching speeds up to 9 km/s [64].

In 2003, the Indian Institute of Science, Bangalore commissioned the free piston driven hypersonic shock tunnel HST3. This facility is capable of reaching velocities up to 7 km/s [64]. This shock tunnel is not only used for research in hypersonic aerodynamics but also for synthesizing new materials as well as studying the surface chemical reactions using various substrates and test gases [97].

VUT-1 is a shock tube from MIPT, Moscow, Russia and is used to investigate kinetic data of nonequilibrium dissociation and recombination processes and other chemical reactions [71]. This facility consists of a combustion driven shock tube, connected to a nozzle and was designed to reach speeds up to 8 km/s [64]. Its operational status is presently unclear.

2.1.3 Suborbital flows facilities

A few other relevant facilities exist, however, these are tailored for suborbital hypersonic flows and will not be discussed in detail.

In Europe, the operational facilities are: the VKI Longshot free piston tunnel testing up to 3 km/s [98], RWTH hypersonic shock tube TH2 reaching flow velocities up to 4.8 km/s [99] and the ONERA F4 hotshot wind tunnel[1] capable of reaching up to 5 km/s [100]. In U.S.A, CUBRC 48-inch tunnel and LENS II operate at suborbital velocities, both reaching up to 3 km/s [76]. However, with additional components, the latter can be operated as an expansion tunnel, being able to reach velocities up to 6 km/s [77]. Brazil operates the IEAv T2 and T3 hypersonic shock tunnels reaching velocities of 2 km/s [101, 102]; Australia has the T4 shock tunnel testing up to 5 km/s [103]; and South Korea has the KAIST shock tube reaching up to 4 km/s [104]. CARDC JF-12 shock tunnel is a Chinese hypersonic facility that can reproduce flight conditions until 3 km/s [105]. Finally, India operates one shock tube at India Institute of Sciences, in Madras, and one shock tunnel at ISRO (Indian Space Research Organisation), both reaching up to 4 km/s and three more shock tunnels HST2, HST4 and HST5, capable of reaching, respectively, 3, 4 and 5 km/s. Information about all the Indian facilities can be found at [106].

2.2 Performance envelopes

To analyse the operation range of different facilities, performance envelopes were obtained reporting data from different simulations reported in the literature. Figure 2.8 shows the ambient conditions used by various research in simulated atmospheres. Figure 2.8a gathers data from simulations with Air and pure N_2 as test gases, figure 2.8b from Venus and Mars (N_2-CO_2) and pure CO_2, figure 2.8c from Gas Giants (He-H_2), pure He and He-Ar mixture and figure 2.8d for Titan atmosphere (N_2-CH_4).

EAST shock tube data was extracted from Grinstead et al. [65], which was obtained compiling different test conditions and respective results. The air boundary represents the atmospheres of Earth, Mars, Venus, Titan, and pure molecular gases such as nitrogen. The H_2/He boundary represents Gas Giants's atmospheres. The results from EAST shock tube using Titan mixture were extracted from Jacobs [107]. Data for the different CUBRC LENS facilities was extracted from Holden [77]. However, their results for the shock speed are expressed in terms of altitude, thus, the "Earth Atmosphere Model" from NASA [108] was employed to find the pressure at the corresponding altitude.

From Kendall et al. [109] and Smith and Mee [110], data from simulations at the X1 expansion tube is reported; and from Jacobs [107], McGilvray [111], Brandis [18] and Gu et al. [112] at the X2 expansion tube. HVST shock tube data was extracted from Jacobs [107], Fujita et al. [113], Abe [80] and Yamada et al. [114]. Jacobs [107] also presented results for TCM2 shock tube, that was completed using data from [115]. KAIST data was also obtained from [115]. Finally, VUT-1 shock tube data was extracted from [115, 116] and from Jacobs [107].

Figure 2.8 also presents the trajectory characteristics of past successful missions in the different planetary atmospheres. For Earth, the Space Shuttle and Apollo reentry trajectories were extracted from Morgan et al. [117]; and return mission reentry trajectories from Herdrich et al. [16]. For Mars, the Mars Pathfinder, Phoenix, Viking and MSL entry trajectories were reported by Edquist et al. [118], while the Exomars entry trajectory profile was obtained from Gülhan et al.'s work [119]. Whenever the velocity

---

[1] recently decommissioned

was expressed in function of altitude, the ”Mars Atmosphere Model” from NASA [120] was employed. Finally, the Huygens entry trajectory data was obtained from Wright et al. [50].

Tests for entry into Earth’s atmosphere have been conducted in the majority of the hypervelocity facilities. From figure 2.8a, LENS I produces shocks with the lowest speeds, reaching approximately 6 km/s for the lowest test pressures. Follow, by ascending order, VUT-1, X2, X1 LENS XX and HVST. The reported results corroborate the information presented in section 2.1.3. EAST is the facility that can reach higher shock speeds, up to 24 km/s, for Air.

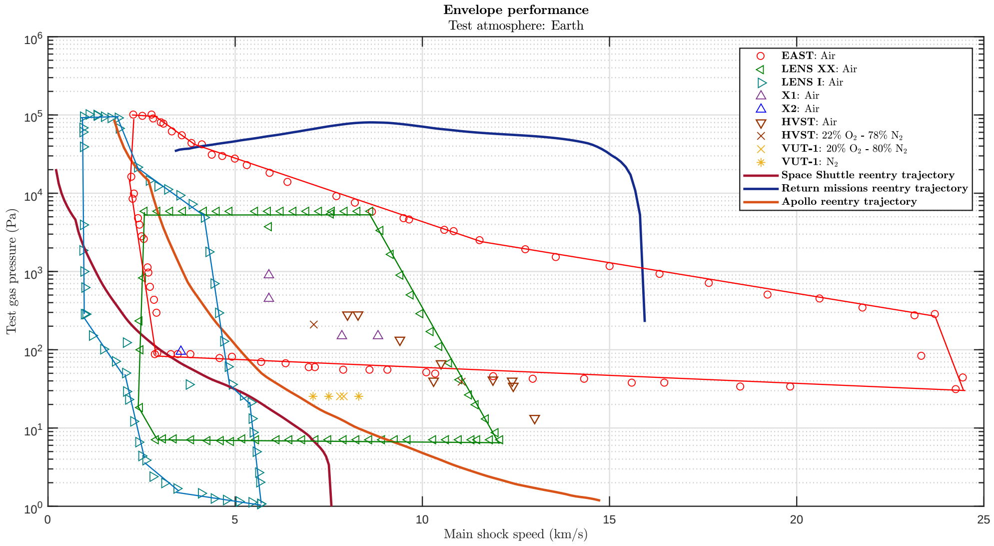

(a) Test mixtures: Air and pure N_2

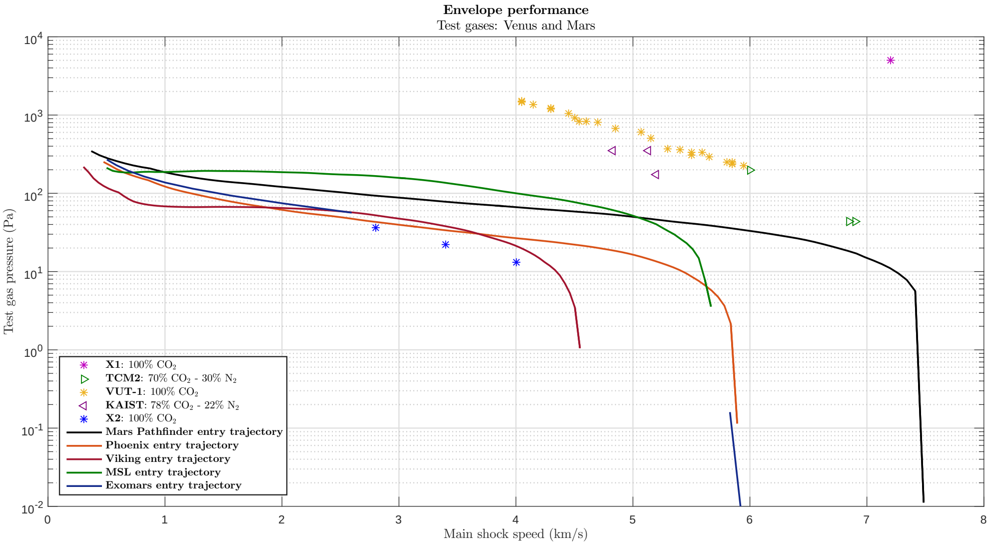

(b) Test mixtures: Venus and Mars and pure CO_2

As shortly discussed above, arc-driven shock tubes, as EAST, are conventional shock tubes with a hot and high sound speed driver gas divided from the driven gas, by a high pressure diaphragm. The electrical discharge is used only to heat the driver gas, which is confined at a small chamber, and is over long before the diaphragm opens, thus isolating the electrical and gas dynamic behaviour [121]. The electrical discharge heats either hydrogen or helium to a temperature of about 8000 K for hydrogen

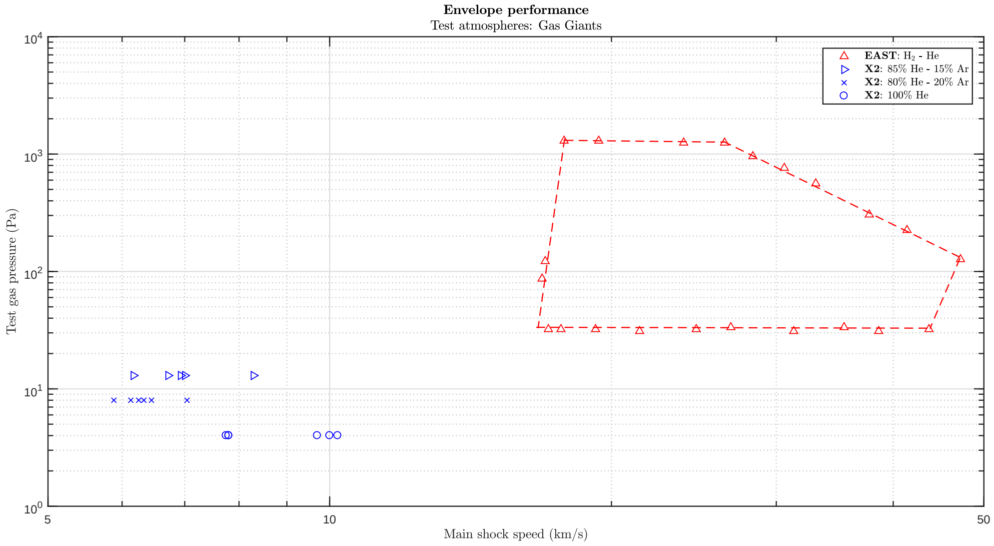

(c) Test mixtures: Gas Giants and pure He

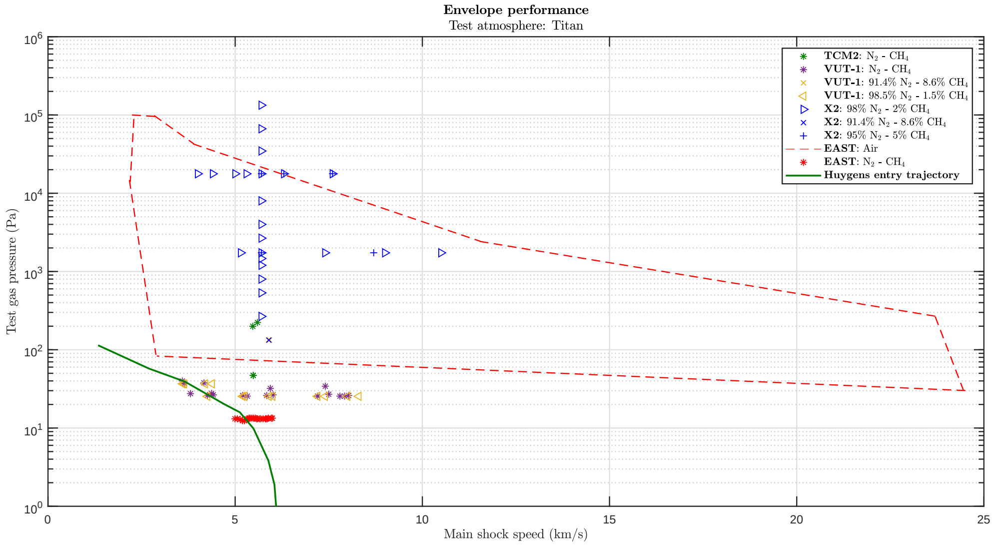

(d) Test mixtures: Titan

Figure 2.8: Performance envelopes for different hypervelocity facilities and different test gases.

and about 20 000 K for helium, without causing melting or ablation of the materials, due to very short discharge times [122]. Hence, EAST produces the highest shock speeds. However, this type of facility has the drawback of having low degree of repeatability between shocks, since an electrical arc is an inherently unstable process difficult to replicate exactly.

Data from VUT-1 and X2, from figure 2.8b (100% CO_2), clearly evidences the expected behaviour of velocity increasing as working pressure decrease. Experiments using pure CO_2 and CO_2 and N_2 mixture, result in the lowest range of obtainable shock speeds, because the gas test is heavier.

As expected, the highest shock velocities are obtained by EAST operating with a mixture of H_2 and He as test gas, being capable to reach velocities between about 15 km/s and 48 km/s (figure 2.8c). Overall, shock velocities in light gases, as H_2 and He, are appreciably higher for the same facility operating parameters, since the impedance of light gases is less than that for heavier gases.

Chapter 3

Shock tube theory

A shock tube is a facility that generates high temperature gas flows of very short duration. In its simplest configuration, the shock tube consists of two sections separated by a diaphragm which permits differential pressurization. However, this simple shock tube cannot generate shocks with high Mach numbers. This limitation may be overcome when using a double diaphragm shock, where the driven gas is heated by an auxiliary shock wave.

By employing different gases and pressures, a wide range of conditions may be achieved. The trade-off for the versatility of the shock tube is the short duration of the test. Therefore, it is critical to establish the duration of the tests as a function of the tube geometry and general operating parameters.

In this chapter, the underlying theory of shock tubes with different configurations is discussed. The ideal one-dimensional fluid dynamic model is employed to establish the shock tube performance thermodynamic and non-ideal effects are also addressed, namely wall boundary layer effects, the formation of blast waves and the non-instantaneous rupture of the diaphragm.

3.1 Basic principles of ideal shock tubes

3.1.1 Single diaphragm with constant area shock tubes

The simplest shock tube configuration consists of two chambers, with unitary area ratio, separated by a single diaphragm and closed at both ends. The diaphragm separates the driver section on the left and the working section on the right. Those are the high pressure and low pressure, commonly referred as regions 4 and 1, respectively. Initially, the chambers are filled with gases at rest.

After the diaphragm ruptures, the gas in the driver section expands towards the working section, causing a normal shock wave. As the shock wave propagates to the right with velocity u_s, it increases the pressure of the gas behind it (region 2) and induces a mass motion with velocity u_2. The test and driver gases are separated by a contact surface, which also moves with velocity u_2 and has pressure p_2. Across this contact surface, the pressure and velocity are preserved, $p_3 = p_2$ and $u_3 = u_2$, and the entropy changes discontinuously. Simultaneously, the expansion waves move into the high pressure section, continuously decreasing the pressure in region 4 to a lower pressure value, p_3, behind the expansion wave.

The flow field developed after diagram removal is represented in figure 3.1.

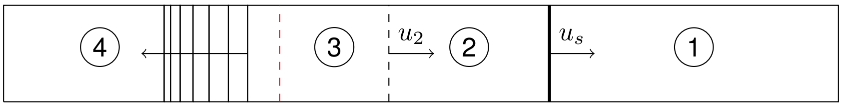

Figure 3.1: Flow diaphragm of a constant area ratio shock tube [not at scale].

Moving normal shock waves

For the one dimensional normal shock wave, the continuity, momentum and energy equations are given in equations A.1 to A.3, from annex A. The temperature, density and pressure ratios equations across the shock wave are detailed in equations A.5 to A.10. Based on these equations, the shock velocity is given in terms of the pressures ratio, p_2/p_1, by

$$u_s = a_1\sqrt{\frac{\gamma_1+1}{2\gamma_1}\left(\frac{p_2}{p_1}-1\right)+1}. \tag{3.1}$$

Along with the initial conditions of the driver and driven gases, the ratio p_4/p_1 determines the strengths of the incident shock and expansion waves that are set up after the diaphragm is ruptured. This ratio is denominated by diaphragm pressure ratio. Based on equations A.11 and A.12, the diaphragm pressure ratio is given by

$$\frac{p_4}{p_1} = \frac{p_2}{p_1}\left\{1-\frac{(\gamma_4-1)\left(\frac{a_1}{a_4}\right)\left(\frac{p_2}{p_1}-1\right)}{\sqrt{2\gamma_1\left[2\gamma_1+(\gamma_1+1)\left(\frac{p_2}{p_1}-1\right)\right]}}\right\}^{-\frac{2\gamma_4}{\gamma_4-1}}. \tag{3.2}$$

For a given diaphragm pressure ratio p_4/p_1, the incident shock strength p_2/p_1 will be stronger as a_1/a_4 is smaller. As $a=\sqrt{\gamma RT}=\sqrt{\gamma(\mathcal{R}/\mathcal{M})T}$, being γ the specific heats ratio, $\mathcal{R}$ the perfect gas constant and $\mathcal{M}$ the molar mass of the gas, the speed of sound is faster in a hot light gas than in a cold heavy gas. Thus, to maximize the incident shock strength for a given p_4/p_1, the driver gas should be a low molecular weight gas at high temperature (hence high a_4) and the test gas should be a high molecular weight gas at low temperature (hence low a_1).

The strength of the incident expansion wave is given by the pressure ratio p_3/p_4. Knowing that $p_2 = p_3$:

$$\frac{p_3}{p_4} = \frac{p_3}{p_1}\frac{p_1}{p_4} = \frac{p_2}{p_1}\left(\frac{p_4}{p_1}\right)^{-1} = \left\{1-\frac{(\gamma_4-1)\left(\frac{a_1}{a_4}\right)\left(\frac{p_2}{p_1}-1\right)}{\sqrt{2\gamma_1\left[2\gamma_1+(\gamma_1+1)\left(\frac{p_2}{p_1}-1\right)\right]}}\right\}^{\frac{2\gamma_4}{\gamma_4-1}}. \tag{3.3}$$

Incident and reflected expansion waves

As explained before, when the diaphragm is removed, an expansion wave is created. The head of this expansion wave moves to the left into region 4. There, the mass-motion velocity is zero, hence the head of the wave propagates to the left with a velocity $u_4 - a_4 = 0 - a_4 = -a_4$.

Within the expansion wave, the induced mass motion is u and it is directed towards the left. Also, the temperature, and hence a, is reduced inside the wave. Therefore, although the head of the wave advances into region 4 at the speed of sound, other parts of the wave propagate at slower velocities. Thus, the expansion wave spreads out as it propagates down the tube. The solution for a simple centred expansion wave, at any local point in the wave can be found from equations A.16 to A.19.

When the head of the unsteady expansion wave reflects at the left wall of the driver section, it starts propagating to the right and interacts with the incident left-running wave, accelerating. This region of mixed left- and right-running waves is called a non simple region. A simple region consists of one family of characteristics given by straight lines, which can only be the case when the wave is propagating into a uniform region. In contrast, a non simple region has both families of characteristics as curved lines. This becomes a numerical problem, where the characteristic lines and the compatibility conditions (the Riemann invariants) are pieced together point by point.

Since the head of the reflected expansion wave has a higher velocity than the incident shock wave, the lengths of the driver and driven sections must be chosen to guarantee that the arrival of the reflected expansion at the end of the shock tube does not occur before the observation point and is delayed as much as possible. This will be discussed later.

Reflected shock wave

Assume that the moving wave is incident on a flat end wall. In front of the incident shock, the mass motion $u_1 = 0$ and behind the incident shock, the mass velocity is u_2 towards the end wall. Once the incident shock reaches the right wall, a reflected normal shock wave is created. The subscript 5 refers to the reflected gas properties. The mass motion behind the reflected shock wave must be zero, i.e., $u_5 = 0$. Thus, the zero-velocity boundary condition is preserved by the reflected shock wave.

The reflected shock propagates into the gas ahead of it with a Mach number

$$M_r = \frac{(u_r + u_2)}{a_2}, \tag{3.4}$$

from the reflected shock equations A.13 through A.15 and considering a calorically perfect gas, a relation between M_r and M_s can be written as

$$\frac{M_r}{M_r^2 - 1} = \frac{M_s}{M_s^2 - 1}\sqrt{1 + \frac{2(\gamma_1 - 1)}{(\gamma_1 + 1)^2}(M_s^2 - 1)\left(\gamma_1 + \frac{1}{M_s^2}\right)}. \tag{3.5}$$

Consequently, the velocity of the reflected wave is given by

$$u_r = a_2 M_r - u_2. \tag{3.6}$$

Shock tube length

The distance x_{test} between the diaphragm and the test section determines the useful flow duration in the shock tube. However, the length of the driver tube, x_4 must be sufficiently large, so that the disturbances reflected from the high pressure end of the tube do not affect the useful flow. Moreover, the length of the working section, x_1, should also be long enough so the reflected wave from its ends does not affect the flow in the test section.

The necessary length of the low pressure section, x_1, in terms of x_{test} and the shock Mach number M_{s1} depends on the flow characteristics in the regions 1 and 2 and also on the type of reflection of the shock from the end of the tube. For strong shocks, according to Walenta [123], the minimum length for the driver section, x_4, is

$$\left(\frac{x_4}{x_{test}}\right)_{min} = \frac{2}{4u_3/a_4}\left[\frac{\gamma_4+1}{(\gamma_4-1)+2}\left(1-\frac{\gamma_4-1}{2}\frac{u_3}{a_4}\right)\right]^{\frac{\gamma_4+1}{2(\gamma_4-1)}} . \tag{3.7}$$

Another semi-empirical relation determines that stable shock conditions will be achieved only at a length of 40 diameters [124].

3.1.2 Single diaphragm with variable area shock tubes

A schematic diagram of a shock tube with a convergent geometry at the diaphragm is represented in figure 3.2.

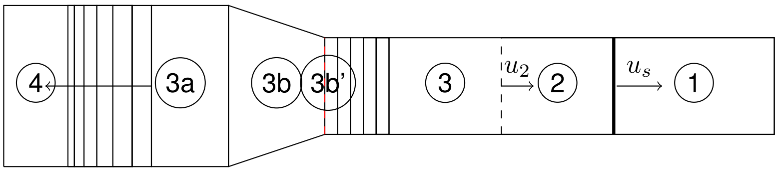

Figure 3.2: Flow diagram of shock tube with convergent geometry [not at scale].

After diaphragm removal, the energy is extracted from the driver gas through an unsteady expansion from state 4 to state 3a. This transition section presents three possibilities: i) if it is uniform, i.e., if it connects equal areas, state 3a and 3b coalesce and denote the state at the diaphragm location; ii) if the cold flow is supersonic, this state is the point in an unsteady expansion at which the Mach number becomes unity. Finally, iii) if the transition is monotonically convergent, the flow from 3a to 3b is a steady nozzle flow and the convergent flow at 3b may be either subsonic or sonic.

For the following analysis, except across the shock itself, isentropic processes and ideal gas behavior are assumed. Based on Alpher and White [125] and considering the general case of a convergent-divergent diaphragm section, the pressure ratio p_4/p_1 may be expanded as

$$\frac{p_4}{p_1} = \frac{p_4}{p_{3a}}\frac{p_{3a}}{p_{3b'}}\frac{p_{3b'}}{p_{3b}}\frac{p_{3b}}{p_3}\frac{p_3}{p_2}\frac{p_2}{p_1} \tag{3.8}$$

where p_4/p_{3a} is the ratio required to accelerate the driver gas through an unsteady expansion from rest to the Mach number M_{3a}; $p_{3a}/p_{3b'}$ is the ratio required to bring the driver gas by a steady expansion from M_{3a} to $M_{3b'}$; $p_{3b'}/p_{3b}$ is the ratio required to bring the gas by a steady expansion from $M_{3b'}$ to M_{3b} through an area ratio $A_{3b'}/A_{3b}$; and p_{3b}/p_3 is the ratio needed from an unsteady expansion from M_{3b} to M_3. At the contact surface, $p_3 = p_2$.

Applying equation A.20 across the non-steady expansion wave (regions $4 - 3a$ and $3b - 3$) and remembering that $u_4 = 0$, equation A.21 through the supersonic nozzle (region $3a - 3b$) and the pressure boundary condition, $p_3 = p_2$, and employing equations A.23 to A.26 yields

$$\frac{p_4}{p_1} = \frac{1}{g}\frac{p_2}{p_1}\left[1 + \frac{\gamma_4 - 1}{2}M_3\right]^{\frac{2\gamma_4}{\gamma_4 - 1}} = \frac{1}{g}\frac{p_2}{p_1}\left[1 - \frac{u_2}{a_1}\frac{a_1}{a_4}\frac{\gamma_4 + 1}{2}g^{-\frac{\gamma_4 - 1}{2\gamma_4}}\right]^{-\frac{2\gamma_4}{\gamma_4 - 1}} \tag{3.9}$$

where the quantity g (equation A.27) is the equivalence factor defined by Alpher and White [125].

For subsonic cold flow (the assumption of isentropy excludes a transition to subsonic flow through a shock), the transition section is a subsonic nozzle with $M_{3b} = M_3$, $p_{3b} = p_3$ and $a_{3b} = a_3$. Equations A.23, A.26 and A.27 reduce to three simultaneous equations in g, M_3 and M_{3a}, which can be solved iteratively with an initial guess of a_4, a_1 and M_s. For this subsonic case, only the ratio A_4/A_1 matters and the existence of a minimum section is irrelevant.

For supersonic cold flow, $M_3 \geq 1$, one must have $M_{3b'} = 1$ (or $M_{3b} = 1$ if the section is monotonically convergent so that $A_{3b} = A_1$ is the minimum area). The usual relationships between area ratio and Mach number in supersonic nozzles apply, as used in obtaining 3.9, to give M_{3a} and M_{3b}. From these M_3, g and p_4/p_1 follows.

As discussed before, the distance x_{test} between the diaphragm and the test section determines the useful flow duration in the shock tube. For this type of configuration, according to Walenta [123], the minimum relation between the driver section and the test section is given by

$$\left(\frac{x_4}{x_{test}}\right)_{min} = \frac{M_{3a} + 1}{4\frac{u_3}{a_4}}\left[\frac{\gamma_4 + 1}{(\gamma_4 - 1)M_{3a} + 2}\left(1 - \frac{\gamma_4 - 1}{2\bar{k}}\frac{u_3}{a_4}\right)\right]^{\frac{\gamma_4 + 1}{2(\gamma_4 - 1)}}, \tag{3.10}$$

where $\bar{k}$ is given by equation A.28.

3.1.3 Double diaphragm shock tube

A simple shock tube cannot generate shocks with extremely high Mach numbers and, in consequence, the gas temperature attainable in such a tube is low. To increase the shock Mach number, the ratio of sound speeds in the driver and working gases must be increased. This can be achieved by using different gases and heating the driver gas.

Cross-sections area reduction at the diaphragm is also equivalent to an increase of the driver gas temperature. This causes a steady expansion wave in the driver gas in the subsonic region of the flow which is thermally more efficient than an unsteady expansion.

When the first diaphragm ruptures, a primary shock wave with velocity u_{s7} is produced, processing it to a contact surface with velocity u_6 and creating expansion waves. When the primary shock wave reaches the second diaphragm, it is reflected and the pressure and temperature increase. Once the diaphragm opens, a main shock wave is produced, with a velocity u_{s1} greater than the velocity of the primary shock wave. Based on the initial conditions, properties in region 11 (driver section), region 7 (intermediate section) and region 1 (working section), before the diaphragm removal, are known.

For a double diaphragm shock tube, both lengths of the driver and intermediate sections need to be long enough, so that the disturbances do not affect the useful flow.

Shock tube with cross-section area reductions at both diaphragms

For the general case of a double diaphragm shock tube with two cross-section area reduction and according to Walenta [123], it is assumed that the second diaphragm is sufficiently weak, so that it bursts immediately when hit by the primary shock wave. Moreover, both primary and main shock waves are assumed strong enough, so the flow in region 3 and 8 is supersonic and the primary shock reflects from the area reduction also as a shock. Finally, steady acceleration to the sonic speed in the cross-section area reductions is assumed to occur isentropically.

A representation for the different zones after the burst of both diaphragms can be found in figure 3.3 and the equations are derived in section A.3.

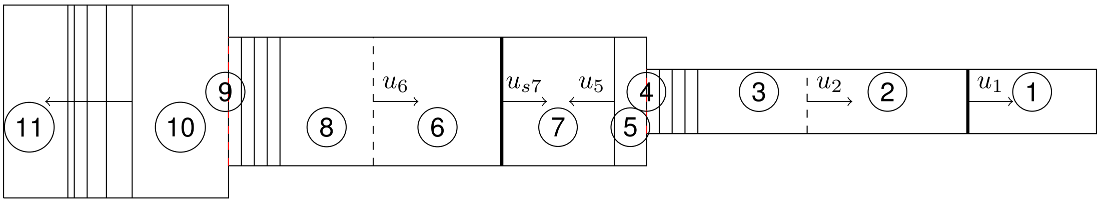

Figure 3.3: Flow diagram of a double shock tube with two cross-section area reductions [not to scale].

For the case of a tube with two cross-section area reduction, the following conditions need to be satisfied, to avoid flow interferences:

a) the head of the expansion wave, reflected from the end of the driver section, must not overtake the primary contact surface before it intersects with the shock reflected from the second diaphragm;

b) the wave, generated at the intersection of the primary contact surface with the shock reflected from the second diaphragm must not overtake the main contact surface before the test section.

Based on the first condition, the ratio x_{11}/x_7 should be larger that a certain minimum value, depending on the shock Mach number M_{s7}. The ratio can be written as

$$\left(\frac{x_{11}}{x_7}\right)_{min} = \left(\frac{M_{10}+1}{4}\right)\frac{a_{11}}{a_7}\left(\frac{1+\frac{U_R}{M_{s7}a_7}}{X\frac{a_6}{a_7}}\right)\left\{\frac{\gamma_{11}+1}{k\left[(\gamma_{11}-1)M_{10}+2\right]}\left[k-\frac{\gamma_{11}-1}{\gamma_7+1}\frac{a_7}{a_{11}}\left(M_{s7}-\frac{1}{M_{s7}}\right)\right]\right\}^{\frac{\gamma_{11}+1}{2(\gamma_{11}-1)}}, \tag{3.11}$$

where

$$\frac{U_R}{a_7} = \frac{u_6}{a_7}\left(\frac{X}{M_6}-1\right). \tag{3.12}$$

To obtain a close form for the expression $(x_7/x_{test})_{min}$, one has to assume that the wave generated at the intersection of the primary contact surface with the shock reflected from the second area reduction behaves like a characteristic line. Based on this assumption, $(x_7/x_{test})_{min}$ can be calculated from

$$\left(\frac{x_7}{x_{test}}\right) = \frac{1}{2\frac{u_3}{a_7}\phi}\left(\frac{\gamma_7+1}{2}-\frac{\gamma_7-1}{2}\frac{\frac{u_3}{a_7}}{\frac{a_4}{a_7}}\right)^{\frac{\gamma_7+1}{2(\gamma_7-1)}}, \tag{3.13}$$

where

$$\phi = \frac{\gamma_7 - 1}{\gamma_7 + 1} \frac{\left[1 + \frac{2}{(\gamma_7 - 1) M_{s7}^2}\right]}{X \frac{a_6}{a_7}} \left[1 + \frac{\frac{U_R}{a_7}}{(1 + M_5) \frac{a_5}{a_6} \frac{a_6}{a_7}}\right]. \tag{3.14}$$

Shock tube with cross-section area reduction only at the second diaphragm

The assumptions for this case are identical to those made in the previous case. However, in this case, the flow in region 8 does not need to be supersonic. The same equations may also be implemented, only considering that the variable k becomes constant, such that $k = 1$. Therefore, equations A.32 and A.33 are no longer necessary.

Shock tube with cross-section area reduction only at the first diaphragm

For this case, only the assumption considering that the primary shock wave is strong enough, such that the flow in region 8 is supersonic, remains necessary. The equations are detailed in section A.3.

Shock tube with constant areas

For this case, equations from the previous case can be applied, only replacing the variable k by 1, whenever necessary. Therefore, equations A.32, A.33 and condition A.47 are no longer necessary. This means that only the conditions to guaranty that the liquefaction of the gas does not occur are required. Moreover, the assumptions concerning the flow in regions 3 and 8 are not necessary.

3.2 Performance enhancement

As seen in chapter 1, entry flight in the hydrogen-helium atmospheres of the outer planets occurs at extreme velocities where the flow if fully dissociated and significantly ionized. Most of the ground test facilities cannot achieve such performances with the notable exception of the EAST shock tube. Thereafter, other venues must be explored to potentially allow the simulation of entry conditions in ground facilities. Two solutions were proposed by Stalker and Edward [126]: replacing helium by neon, a heavier gas; or utilising a higher amount of helium diluent than the actual entries.

Their first proposal was to use hydrogen and neon alternatively to the original hydrogen and helium mixture. If used in sufficient concentrations, neon increases the molecular weight of the test gas mixture to an extent that allows blunt body flows to have hot enough post-shock temperatures, allowing to reproduce the ”real” dissociation and ionization degree of hydrogen. They found that, until the post-shock temperature became so hot that the neon itself began to ionise, the substitution held.

Stalker and Edward also proposed an increase of the amount of helium diluent in the flow field. They showed that, due to its large ionization energy, the helium in the hydrogen-helium flow field acted as an ’inert diluent’ and collision partner for the hydrogen molecules and atoms. When increasing the amount of helium diluent in the flow field, they concluded that an approximately 19 km/s flight equivalent velocity flow condition can be used to simulate the shock layers for proposed entries into Uranus and Saturn, and potentially even faster entries. This has been studied recently by James et al. [127].

3.3 Disturbance effects

In an ideal shock tube, the shock wave propagates with velocity u_s and the contact surface with velocity u_2, both at constant pace. However, in an actual shock tube, the presence of a wall boundary layer alters the velocity of the main shock wave and of the main contact surface. This wall boundary layer between the shock and the contact surface removes mass from this region, causing the shock to decelerate and the contact surface to accelerate. Consequently, the flow becomes non-uniform and the separation distance, l, decreases below the ideal value, reducing the effective test time.

3.3.1 Wall boundary layer

The effect of boundary layer formation behind a shock wave has been studied by many authors. Trimpi and Cohen [128], Mirels [129], Dem'yanov [130] and Spence and Woods [131] presented wall boundary layer theories that were primarily concerned with the unsteady motion of the shock. They all introduced small perturbations to the flow variables, as a way to represent the displacement effect of the boundary layer.

Both Trimpi and Cohen and Mirels assumed a one-dimensional small perturbation theory using the acoustic approximation. The firsts introduced a wall friction term in the moment equation and an entropy production term arising from wall heat transfer and viscous dissipation in the energy equation. They were able to show that the shock was attenuated by unsteady waves which were continuously generated by the effects of viscosity and heat transfer throughout the entire flow field behind the shock. Mirels criticized their formulation arguing that these effects were confined to the wall boundary layers due to the change of the entropy, that they had considered as being convected downstream with the ideal flow velocity. In the linearised equations of motion, Mirels introduced only a mass addition term in the continuity equation. Moreover, he stated that the unsteady waves which were generated in the inviscid core should be attributed to the radial component of the velocity at the edge of the boundary layer. However, Trimpi and Cohen's process implied a thick boundary layer, while Mirels assumed a thin boundary layer.

Despite of these differences, both Trimpi and Cohen's and Mirels's theories predicted the same order of attenuation and an agreement with experiments for weak shocks. Moreover, it is important to note that these two theories are inadequate to represent the behaviour of strong shocks, since their assumption neglects the flow in the rarefaction wave, which must be considered as the shock strength increases.

The Mirels formulation was also used by Dem'yanov, who obtained a closed form solution for the case of laminar boundary layer development between the shock and the interface but neglected disturbances originating in the cold flow. He showed that the growth of the hot flow boundary layer caused the shock to decelerate and the interface to accelerate.

Spence and Woods [132] presented a theory which considered only the hot flow. They assumed axial symmetry and carried out a detailed derivation of the linearised unsteady conservation equations, confirming Mirels' formulation for flows where the boundary layer thickness is much smaller than the tube diameter. They also extended Dem'yanov's basic method of solution to cover the case of a turbulent hot flow boundary layer.

In 1959, Duff [133] observed that in a low pressure shock tube, at a certain point, the separation between the contact surface and the shock wave reaches a maximum value and that, after the limiting value, they both start to move with equal and constant velocity. This revealed that the duration of the hot flow - i.e. the test time - tended to a finite limit as the distance from the diaphragm increased. He also deduced that the limiting time varied as the square of the shock tube diameter for laminar boundary layer growth behind the shock. The same mechanism was proposed by Anderson [134] for the reduction of shock tube test time. Anderson also predicted the variation of shock tube test times with distance from the diaphragm, under the assumption that the shock wave moved at constant velocity.

Roshko [135], Hooker [136], Mirels [57, 137] and Ackroyd [138] theories sought to predict only the duration of the hot flow, while satisfying the condition of mass continuity between the shock and the contact surface.

Roshko and Hooker studied the limiting flow effect both experimentally and theoretically. Based on the experimental data, Roshko was able to confirm the validity of the basic theory. Analytical studies by Roshko, posteriorly expanded and modified by Hooker, were based on the computations of boundary layer parameters. Roshko used a simplified model assuming that the contact surface moves with a constant velocity and that the free stream has a uniform velocity profile. Later, Mirels modified this model to account for acceleration of the contact surface, flow non-uniformities and real gas effects. Ackroyd's theoretical predictions also shown good agreement with Duff's experimental measurements obtained at low shock Mach number in Argon.

Mirels theory

According to Mirels [57], in a conventional shock tube, the separation between the contact surface and the shock wave decreases as the distance to the diaphragm increases (as illustrated in figure 3.4). Mirels theory takes into account the non-uniform flow between the shock and the contact surface. The coordinate system used considers that the shock wave is stationary and the wall moves with velocity u_w. In this system, the flow between the shock and the contact surface is steady. The boundary layer is also considered thin relative to the tube radius.

Consider the shock is located at $l = 0$ and the free stream portion of the contact surface at $l = l_m$. Following Mirels notation, the flow upstream of the shock is denoted by subscript ∞ and moves with the same velocity as the wall, u_w. The subscript e represents the free stream conditions between the shock and the contact surface and the subscript 0 the free stream conditions directly downstream of the shock. The percentage of mass flow in the boundary layer increases with l such that all the mass flow is in the boundary layer at l_m and the free stream is stationary at that location.

In a circular cross-section tube with diameter d, the mass flow past the contact surface is given by

$$\dot{m}_c = \pi d \rho_{w,0}(u_w - u_{e,0})\delta_r, \tag{3.15}$$

where $\rho_{w,0}$ and $u_w - u_{e,0}$ are characteristic boundary layer densities and velocities, respectively, and δ_r the characteristic boundary layer thickness. In the case of a laminar boundary layer, the thickness δ_r

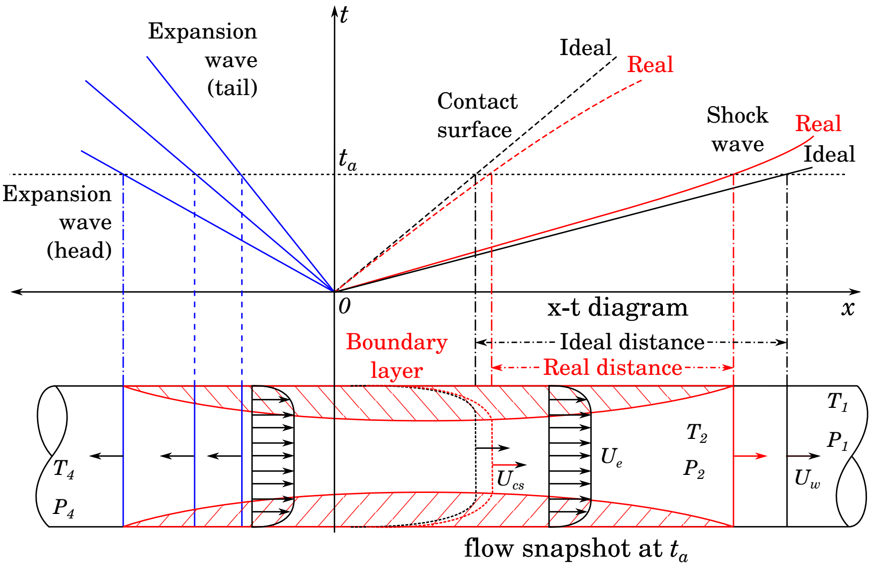

Figure 3.4: Boundary layer development [not to scale].

can be written as

$$\delta_r = \beta \left(\frac{\nu_{w,0} l_m}{u_w - u_{e,0}} \right)^{\frac{1}{2}}, \tag{3.16}$$

where $\nu_{w,0}$ is the kinematic viscosity at the wall, corresponding to the wall temperature T_w, l_m is the development distance of the boundary layer and β is a parameter that depends on the boundary layer development in the tube.

Past the contact surface, the flow out of region 2 is given by

$$\dot{m}_c = \pi d \beta \rho_{w,0} (u_w - u_{e,0}) \left(\frac{\nu_w l_m}{u_w - u_{e,0}} \right)^{\frac{1}{2}} \tag{3.17}$$

and, at the same time, gas is being added to region 2, at a rate $\dot{m}_s$ given by

$$\dot{m}_s = \rho_{e,0} u_{e,0} \frac{\pi d^2}{4}. \tag{3.18}$$

Equating equations 3.17 and 3.18, l_m yields

$$l_m = \frac{d^2}{16\beta^2} \left(\frac{\rho_{e,0}}{\rho_{w,0}} \right)^2 \frac{u_{e,0}^2}{u_w - u_{e,0}} \frac{1}{\nu_{w,0}}. \tag{3.19}$$

To find an accurate estimate of β, first, Mirels considers the boundary layer to develop in an uniform external stream and, then, uses the concept of local similarity.

Applying the uniform free stream, l_m is found such that the excess mass flow through the boundary layer equalled the mass flow trough the shock. Based on numerical values, Mirels reached a correlation for the results of β_0 within 2% given by

$$\frac{\beta_0}{C_{e,0}^{0.37}} = 1.135 \left(\frac{2(W-1)}{1+1.022W} \right)^{\frac{1}{2}} \left(1 + \frac{1.328 + 0.890W}{ZW - 1} \right), \tag{3.20}$$

where $C_{e,0} = [(\rho_e \mu_e)/(\rho_w \mu_w)]_0$ corrects for variable $\rho\mu$ and $W \equiv u_w/u_{e,0} = \rho_{e,0}/\rho_\infty$, is valid for all σ. $Z = (\gamma+1)/(\gamma-1)$ is used for an ideal shock and for the case of a strong non ideal shock ($W \gtrsim Z$), Z is replaced by W. Regardless of the precise value of σ and of the viscosity law, Mirels considers this relation sufficiently accurate for most gases encountered in shock tubes. However, the obtained β_0 is too small and, consequently, l_m is overestimated.

To improve the β estimate, the variation of the free stream conditions was taken into account. In the local similarity approximation, the development of the boundary layer and the variation in the free stream properties are dealt simultaneously.

For the local similarity concept, Mirels assumes that the boundary layer profile at each l corresponds to a boundary layer associated with a uniform free stream and a wall velocity u_w. Initially, the origin of this boundary layer, l_i, is unknown. To be chosen, the excess flow in the boundary layer at each l is considered to have the correct local value. It is also assumed that the boundary layer growth at each section is the same as for the corresponding uniform free stream boundary layer.

Based on an approximate analytical integration, for strong shocks, β_1 yields

$$\frac{\beta_1}{\beta_0} = \left\{ \frac{1+1.002W}{2(W-1)^2} \frac{1}{(3.022W-1)\ln\left(\frac{W}{W-1}\right) - 3.022} \right\}^{\frac{1}{2}} = \frac{W}{W-1}[1+O(W^{-2})], \tag{3.21}$$

for known values of β_0.

Test time

The test time in real shock tube flows, defined by Hooker [136] as ”the spatial or temporal extent of shocked gas uncontaminated by driver gas” is always lower than the one predicted by the ideal shock tube theory. While in an ideal shock tube, both shock wave and contact surface propagate with constant velocities, in an actual shock tube, the presence of a wall boundary layer alters the velocity of the main shock wave and of the main contact surface.

Mirels [57] characterized the test time, τ, which corresponds to the difference in time between the arrival of the shock and the arrival of the contact surface, at a fixed value of x. Defining $\bar{\tau} \equiv u_w \tau / l_m$ as the test time at x divided by the test time at $x \to \infty$,

$$\bar{\tau} = T_b, \qquad X = X_b - \frac{T_b}{W}, \tag{3.22}$$

where X_b and T_b are corresponding values of X and T, respectively given by

$$X \equiv \frac{x_s}{W l_m} \equiv \frac{u_{e,0} t}{l_m} = \frac{\int_0^{\bar{\delta}} \frac{\bar{\delta} d\bar{\delta}}{V H_e^2}}{\int_0^1 \frac{\bar{\delta} d\bar{\delta}}{H_e^2}}, \qquad T \equiv \frac{l}{l_m} = \frac{\int_0^{\bar{\delta}} \frac{\bar{\delta} d\bar{\delta}}{H_e^2}}{\int_0^1 \frac{\bar{\delta} d\bar{\delta}}{H_e^2}}. \tag{3.23}$$

For strong shocks, the external free stream remains fairly uniform and the excess mass flow in the boundary layer grows approximately as $l^{\frac{1}{2}}$. With some formula manipulation, Mirels reached the relation between X and $\bar{\tau}$, which is given by

$$-X = 2\left[\ln\left(1-\bar{\tau}^{\frac{1}{2}}\right)+\bar{\tau}^{\frac{1}{2}}\right]+\frac{\bar{\tau}}{W}, \tag{3.24}$$

allowing the calculation of the test time, $\bar{\tau}$, at x.

3.3.2 Wall drag effects on shock velocity

As the boundary layer grows, the speed of the shock wave is reduced through drag effects. Milne [139] developed a simplified theory to estimate the effects of the shock-boundary layer interaction by adding a source term to the ideal case. For a circular cross-section tube of working diameter d_1, the momentum source term per unit length of tube is given by

$$S_w = \frac{4\int_0^{d_1}\tau_w dz}{d_1^2} = \frac{4\tau_w}{d_1}, \tag{3.25}$$

where d_1 is the diameter of the working section and τ_w the wall friction, that is expressed as function of the coefficient of friction, C_f, and the ideal speed and density of the shock, respectively, u_s and ρ_s,

$$\tau_w = C_f\frac{\rho_s u_s^2}{2}. \tag{3.26}$$

The coefficient of friction is parametrized in terms of the Reynolds number, Re, by

$$C_f = \begin{cases} 64/\text{Re} & \text{if Re} < 1200 \\ 0.316/\text{Re}^{\frac{1}{4}} & \text{if } 1200 < \text{Re} < 10^5 \\ 0.00332 + 0.221/\text{Re}^{0.237} & \text{if Re} > 10^5 \end{cases} \tag{3.27}$$

where Re is given by

$$\text{Re} = \text{Re}_0 u_s = \left(\frac{d_1}{\nu}\right)u_s, \tag{3.28}$$

since $\text{Re}_0 = d_1/\nu$, where ν corresponds to the kinematic viscosity

$$\nu = \mu\frac{\sqrt{\frac{T_s}{3000}}}{\rho_s} \tag{3.29}$$

and the viscosity μ, a function of the gas in the shock tube, is typically approximated by 10^{-4} [139].

Given these parameters, the momentum source term can be added to the velocity equation, to be calculated iteratively by

$$u_{losses}(i) = u_{losses}(i-1) - \frac{S_w dx}{\rho_s} \tag{3.30}$$

being $u_{losses}(i-1)$ the velocity in the previous step, each distanced by a value dx from the previous. This way, the velocity of the shock accounting with the influence of the wall boundary layer can be predicted.

3.3.3 Blast wave formation

As previously explained, a shock tube in its traditional configuration consists of high pressure gas in the driver section which is suddenly released by the rupture of a membrane, leading to shock structure comprising a shock wave, a contact discontinuity and a family of expansion waves. What is experimentally observed is that, for sufficiently long shock tubes, this wave structure eventually evolves into a shape resembling an air blast wave [140].

To study the formation of the blast wave, the wave interactions taking place upon the reflection of the head expansion wave at the left end wall needs to be considered. When the reflected head wave reaches the right-propagating shock, it marks the onset of the Friedlander wave form in the shock tube. The determination of the location of the onset of the wave form only requires tracking the evolution of the head wave (figure 3.5). Note that this algorithm was developed only for single diaphragm configurations, hence the notation from section 3.1.1 is followed.

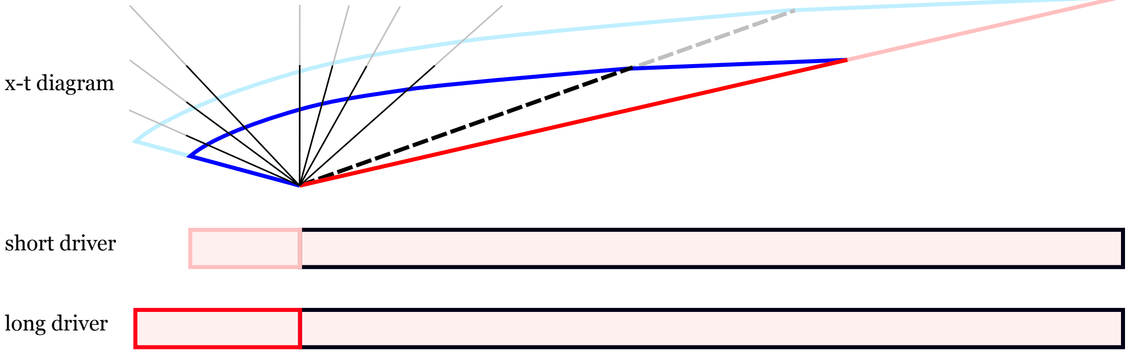

Figure 3.5: Blast wave formation [not to scale].

The location of the Friedlander wave is given by

$$L = L_4 + u_s t_d \tag{3.31}$$

where L_4 is the length of the driver section, u_s is the shock speed and t_d is the time of onset of the Friedlander wave, given by

$$t_d = \frac{2L_4 a_2}{a_4(u_2 + a_2 - u_s)} \left(\frac{p_4}{p_2}\right)^{\frac{\gamma_4+1}{4\gamma_4}}. \tag{3.32}$$

In this expression, a_2 and a_4 are the sound speeds, and p_2 and p_4 the driver pressures, respectively behind the shock and initially at the driver section. γ_4 is the specific heat ratio in the driver section. The shock speed u_s can be obtained by equation 3.1, once the pressure ratio p_4/p_1 is known from equation 3.2. The velocity behind the shock u_2 can be computed through equation A.11 and the shock speed a_2 by the following expression

$$a_2 = a_1 \sqrt{\frac{p_2}{p_1} \frac{\frac{\gamma_1+1}{\gamma_1-1} + \frac{p_2}{p_1}}{1 + \frac{\gamma_1+1}{\gamma_1-1}\frac{p_2}{p_1}}}. \tag{3.33}$$

3.3.4 Secondary diaphragm rupture

Numerous theories have been proposed to model the diaphragm rupture process. The *ideal rupture* model (figure 3.6a) is usually used as a first approach and considers the secondary diaphragm to be infinitely thin and massless, to rupture instantaneously on impact by the primary shock and, therefore, to have no impact on the flow.

However, in reality, the diaphragm interferes with the flow during and after rupture, affecting both the strength of the primary shock reflection generated and the rate of expansion experienced by the test gas, that is forced to stagnate. Consequently, the test flow conditions deviate from the ideal one. The two most widely used approaches are the *diaphragm inertia* and *holding time* rupture models, that take into account the finite rate opening time of the secondary diaphragm.

The *diaphragm inertia* model (figure 3.6b) was proposed by Morgan and Stalker [141] and acknowledges the influence of diaphragm inertia in limiting the rate of expansion. This model assumes that the diaphragm breaks instantaneously once the primary shock hits it and then it stays together as an obstacle in the flow field. The reflected shock is weakened over time through interaction with expansion waves caused by diaphragm acceleration.

To determine the effect of heat losses and the non ideal rupture of the light secondary diaphragm on the driver performance, Kendall et at. [109] developed an experiment in the X1 expansion tube. Their study compared experimental shock speed data around the secondary diaphragm to both Morgan and Stalker's [141] original inertia diaphragm model and Petrie-Repar [142] numerical inertial diaphragm model that solved the unsteady one-dimensional Arbitrary Euler Lagrangian (AEL) equation for inviscid compressible flow during the shock reflection process. Kendall et al. concluded that Petrie-Repar's model simulated the diaphragm rupture better than Morgan and Stalker's [141]. However, after the first 30 μs, the trajectories computed by the AEL code diverged and the shock speed was underpredicted. Hence, Kendall et al. stated that this meant that *"the diaphragm inertial model, in its current form, is not complete"*.

Wegener et al. [143] studied the rupture of a light cellophane diaphragm in an expansion tube. They impulsively subjected the diaphragm to a large pressure differential via a shock wave and recorded holographic images at various times during the rupture process. It was found that the initially curved diaphragm broke peripherally after impact by the shock wave and, upon rupture, the diaphragm flattened out and became planar. After propagating about a quarter of a tube diameter downstream, it began to fragment in the centre, concluding that the mechanism of the cellophane diaphragm rupture in the expansion tube is fragmentation. Wegener et al. [143] also verified that the trajectory of the diaphragm and gas interface was well approximated by the diaphragm inertial model for a short time after rupture, losing then accuracy gradually. After half a tube diameter downstream, the interface accelerated more than predicted due to a reduction in the diaphragm mass caused by fragments falling behind.

To examine the effect of diaphragm thickness and material on flow disturbance due to diaphragm rupture, Furukawa et al. [144] performed an experiment in the Japanese JX-1 free piston driven expansion tube, using the shadowgraph technique and wall pressure measurements. The secondary diaphragm separating the shock tube and the acceleration tube was a sheet made either of Mylar or cellophane. They tested a 23 μm thick cellophane and 3 and 25 μm thick Mylar and observed radiation emission behind the diaphragm for both cellophane 23 μm and Mylar 25 μm diaphragms, which evidenced stagnation of the test gas. In these cases, because of the interaction with the rupture diaphragm segments, the transmitted shock wave was slowed down after the diaphragm rupture and the shock speed was decreased. Only for Mylar 3μm, the shock wave remained planar and the transmitted shock wave almost keep its incident speed even after rupture. Nevertheless, Furukawa et al. [144] considers that the experimental trajectory was reproduced well by the *diaphragm inertia* model, although the model still underestimates the shock wave speed.

The *holding time* rupture model (figure 3.6c), proposed by Haggard [145], notes the time of arrival of the primary shock at the secondary diaphragm and, after a specific time, the diaphragm is instantaneously removed. The *holding time* secondary diaphragm rupture model underestimates the test gas recombination through the unsteady expansion [69]. However, it provides a simple pre-rupture flow field.

Wilson [146], Roberts et al. [147] and Bakos and Morgan [148] employed this *holding time* model and verified that produces pressure disturbances near the secondary diaphragm observed in experiments. Roberts et al. also made a study on the effect of the secondary diaphragm thickness and diaphragm deformation and estimated diaphragm rupture time numerically and experimentally. Moreover, Bakos and Morgan demonstrated the limitations of the *holding time* model through comparison with an inertial diaphragm model.

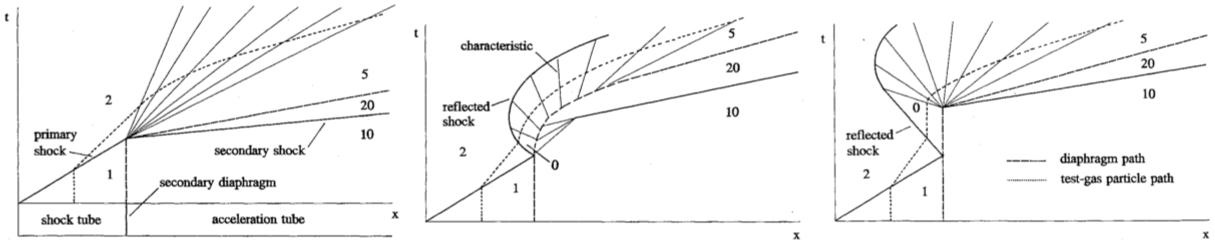

(a) *Ideal rupture* (b) *Diaphragm inertia* (c) *Holding time.*

Figure 3.6: Rupture models illustrations by Bakos and Morgan [148]

3.4 Nozzle flow

A shock tube can be used as an aerodynamic facility by adding a nozzle section within the entrance to the dump tank and adding the necessary windows. This has the advantage of larger area-cross section wherein scale models may be placed facing the flow. After the initial shock wave expands and crosses the model, the moving test gas is further expanded and accelerated, with the corresponding decrease in temperature, pressure and density. Another important effect is that chemical reactions are quickly frozen due to the steep decrease in density and temperature occurring over the expansion, so that the gas composition may be on a first approach assumed to be the same than the pre-shocked one. The useful test time then corresponds to the time between the initial shock wave (black thick line in figure 3.7) and the contact wave (dashed black line in figure 3.7) crossing with the test model.

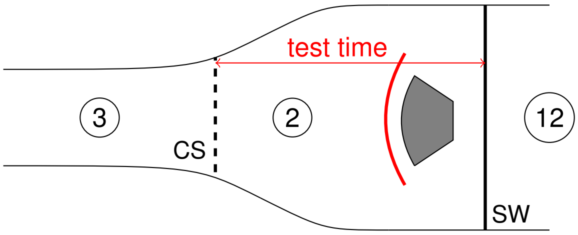

Figure 3.7: Nozzle design.

The new gas conditions may be estimated in a first approach resorting to the quasi-1D nozzle equations:

$$\frac{A_2}{A_{12}} = \frac{M_{12}}{M_2}\left(\frac{1+\frac{\gamma-1}{2}M_2^2}{1+\frac{\gamma-1}{2}M_{12}^2}\right)^{\frac{\gamma+1}{2(\gamma-1)}}, \tag{3.34}$$

$$\frac{p_2}{p_{12}} = \left(\frac{1+\frac{\gamma-1}{2}M_{12}^2}{1+\frac{\gamma-1}{2}M_2^2}\right)^{\frac{\gamma}{\gamma-1}}, \tag{3.35}$$

$$\frac{T_2}{T_{12}} = \left(\frac{1+\frac{\gamma-1}{2}M_{12}^2}{1+\frac{\gamma-1}{2}M_2^2}\right). \tag{3.36}$$

This approach is generally sufficiently good if the effective nozzle cross section is taken, accounting for boundary layer effects [149] as leading to a smaller effective nozzle area-cross-section.

A somewhat similar case occurs for an expansion tube (figure 3.8), where the gas is expanded and accelerated as it enters a second test section with a larger area A. This results in better performance and faster shock waves.

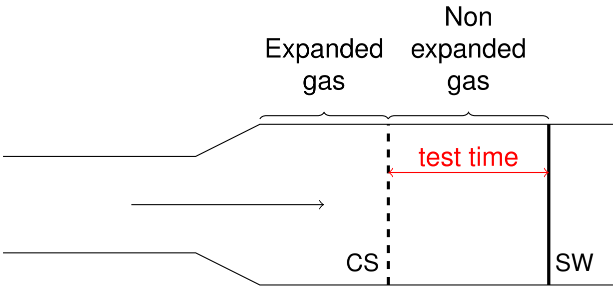

Figure 3.8: Expansion tube design.

Nevertheless, a few difficulties arise whenever expansions are being considering in shock tube facility. As the gas expands throughout the nozzle or the expanding cross section, the gas density inevitably decreases by a non-negligible amount (in the supersonic regime), and at a microscopic level, the rate of collisions between molecules also decreases. Molecules and atoms have both translational and internal degrees of freedom[1] which account for the total energy of the gas [150]:

$$E_{gas} = \sum_{sp} E^{sp} = \sum_{sp}(E^{sp}_{tr} + E^{sp}_{int}). \tag{3.37}$$

When there are enough collisions between the gas atoms and molecules, the translational and in-

---

[1] electronic excitation (atoms and molecules), vibration and rotation (just molecules), within the Born-Oppenheimer approximation

ternal degrees are said to be in equilibrium, with the same characteristic temperature T. However, if the rate of collision decreases enough, nonequilibrium between these different degrees of freedom start being noticeable, since the translational mode requires much less collisions than internal modes to effectively redistribute energy and achieve thermodynamic equilibrium [151]. The relaxation of the internal modes with translation, in the framework of a Boltzmann equilibrium of the internal states, may on a first approach be described by the Landau-Teller equation [152]:

$$\frac{\mathrm{d}E_{int}^{sp}}{\mathrm{d}t} = \rho_{sp} \frac{E_{int}^{sp}(T) - E_{v}^{sp}(T_{int})}{\tau_{tr-int}^{sp}} \tag{3.38}$$

with τ_{tr-int} being the characteristic relaxation time between the translational and internal modes.

As the expansion of a gas proceeds and the density correspondingly decreases, the energy exchange between translational and internal modes slows down, as the consequence of the ρ_{sp} term getting smaller, up to a point where T_{int} starts lagging behind T, up to a point where T_{int} may even freeze to a value intermediate to T_2 and T_{12}.

This evidences a conceptual difficulty with this kind of facilities: the thermodynamic state of the moving, post-shock gas is uncertain, as it experiences an expansion that may or may not have disturbed the thermodynamic equilibrium state of this gas. Note that this problem does not occur with a reduction of the area-cross section, since in this case the gas is only compressed, ρ have nowhere to go but up and the energy exchange processes are by definition fast enough to maintain thermodynamic equilibrium for the moving gas. Even in the case of an expansion tube, the only conditions where the test gas may be rigorously considered as being in thermal equilibrium is the state 2 between the shock wave and the contact surface. The gas moving behind the contact surface experiences an expansion (see figure 3.8) and therefore its thermal equilibrium condition is not able to be properly ascertained.

All in all, the remarks above do not imply that this sort of facilities may not provide accurate results. As long as awareness to this particular situation exists, one may deploy additional experimental and numerical diagnostics to try to determine the exact internal temperature of the nozzle flow and experiments carried out will then provide accurate validation test cases as long as the value for T_{int} is reported and accordingly used in numerical reconstruction models. This is a situation akin to the one encountered in the determination of plasma plume properties in continuous plasma wind tunnels where a hot plasma is expanded through a nozzle and then typically used for TPS testing.

The differences between a real flow and a simulated nozzle flow (besides models size) are conceptually presented in figure 3.9.

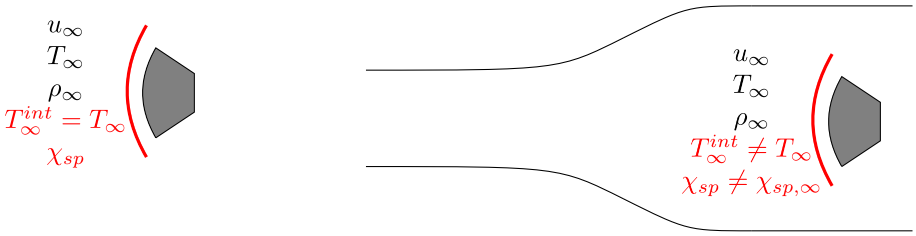

(a) Real entry (b) Nozzle

Figure 3.9: Real entry and nozzle properties.

Chapter 4

Application to the ESTHER shock tube design

The ESTHER shock tube is currently being commissioned at Instituto Superior Técnico, Lisbon, to support European planetary exploration missions. The requirements for this new shock tube call for a facility capable to overcome the current state-of-the-art with an emphasis on superorbital flow regimes. Therefore, a high performance facility is required, which demands a detailed analysis of the facility design.

This chapter presents estimations for the ESTHER shock tube performance in both single and double stage configuration. First, a explanation of the chosen area ratio is presented and then, for the optimal configuration at different working pressures, the influence of the driver and intermediate pressures in the shock speed are discussed. Moreover, an analysis of Earth, Mars, Titan and Gas Giants' atmospheres, introducing disturbance effects, as the formation of a boundary layer, Friedlander blast wave and the delay caused by the diaphragm opening, is performed, concluding about the losses when comparing with the ideal case. These effects are also represented in $x-t$ wave diagrams.

Finally, a performance envelope for the ESTHER shock tube is designed taking into consideration the best and worst performance of the shock tube to obtain the maximum range of shock speeds for different atmospheres.

4.1 Aerodynamic design

To evaluate ESTHER performance,it is worthwhile first, to consider the effect of the driver to driven sections ratio. Both single and double diaphragm configurations with an area contraction between the driver and the working sections are modelled. Then, the influence of the driver pressure, for a double diaphragm configuration, is analysed. Finally, as the optimized pressure ratios are highly dependent on the intermediate pressure, the influence of the intermediate pressure is studied. All results are obtained using the STAGG code.

The STAGG code (Shock Tubes and Gas Guns), developed by Fluid Gravity Engineering Ltd., was designed to predict the performance of shock tubes. STAGG can model single or double diaphragm gas driven shock tubes, with or without convergent sections at either diaphragms. The model is based on the work of Alpher and White [125], Walenta [123] and Mirels [57]. The calculations of shock speed and pressure, at various points in the shock tube, are based on the assumption of an isentropic and inviscid gas, the conservation of mass and energy and the sonic condition at the narrow points of convergent sections [13]. These shock speeds are calculated based on the chosen gas type, temperature and pressure for both driver and working sections. Losses are not included in these calculations and will be discussed later.

As discussed in chapter 3, fast shock speeds require very high driver to working section pressure ratios (p_{11}/p_1). It is also advantageous to have a high ratio between the corresponding gas sound speeds (a_{11}/a_1). Hence, a hot and light gas in the driver section is required, such as hydrogen (H_2). However, the ignition of a premixed mixture of hydrogen and oxygen leads to a detonation for H_2 molar fractions as low as 20% [83]. The dilution by an inert gas is then necessary and can be achieved by adding helium (He) into the mixture, with the advantage of keeping a low mixture molar mass. Therefore, a mixture of 7:2:1 of He, H_2 and O_2, that is available in STAGG's directory, is used for the simulations.

Unless clearly specified in the simulations, the driver has a molar mass of 7.1 kg/mol, γ of 1.56 and a temperature of 2800 K; the working temperature is 300 K (room temperature). For a double diaphragm configuration, the intermediate section has a molar mass of 4.0 kg/mol, γ of 1.667 and temperature of 300 K. The driver temperature is considered to be 2800 K due to the experiences of Hendershot [153], during the development of the Convair shock tunnel.

The test gases are simulated using thermochemical files contained in STAGG's directory, generated by the NASA CEA code [154], including Air, Mars, Titan and Gas Giants. Air is simulated by a molar composition of 78% N_2, 21% O_2 and 1% Ar; Mars by 95.7% CO_2, 2.7% N_2 and 1.6% Ar; Titan by 98.5% N_2 and 1.55% CH_4; and Gas Giants by 90% H_2 and 10% He.

CEA stands for Chemical Equilibrium with Applications and it considers thermochemical equilibrium for the working gas as a worst case estimate. This is a limit condition for chemically reacting flows. The other one is frozen flow. Both of these flows are isentropic (ignoring friction and heat losses) [155]. Whereas in frozen flow there are no chemical changes, in equilibrium flow there are reactions occurring at a high rate[1] and the process may be assumed to be reversible (isentropic).

Equilibrium flow implies infinite chemical and vibrational rates. However, such flows never occur in nature as all chemical reactions are vibrational energy exchange need certain number of molecular collisions to occur [155]. Frozen flow implies zero reaction rates and, as a result, the chemical composition remains constant throughout space and time.

4.1.1 Single diaphragm design with area change

For a single diaphragm shock tube, the shock speed gains due to area ratio change between the driver and working sections are presented in figure 4.1. The results are shown for three different working pressures (10, 25 and 100 Pa) and for different atmospheres (Earth, Mars, Titan and Gas Giants).

---

[1] essential infinite

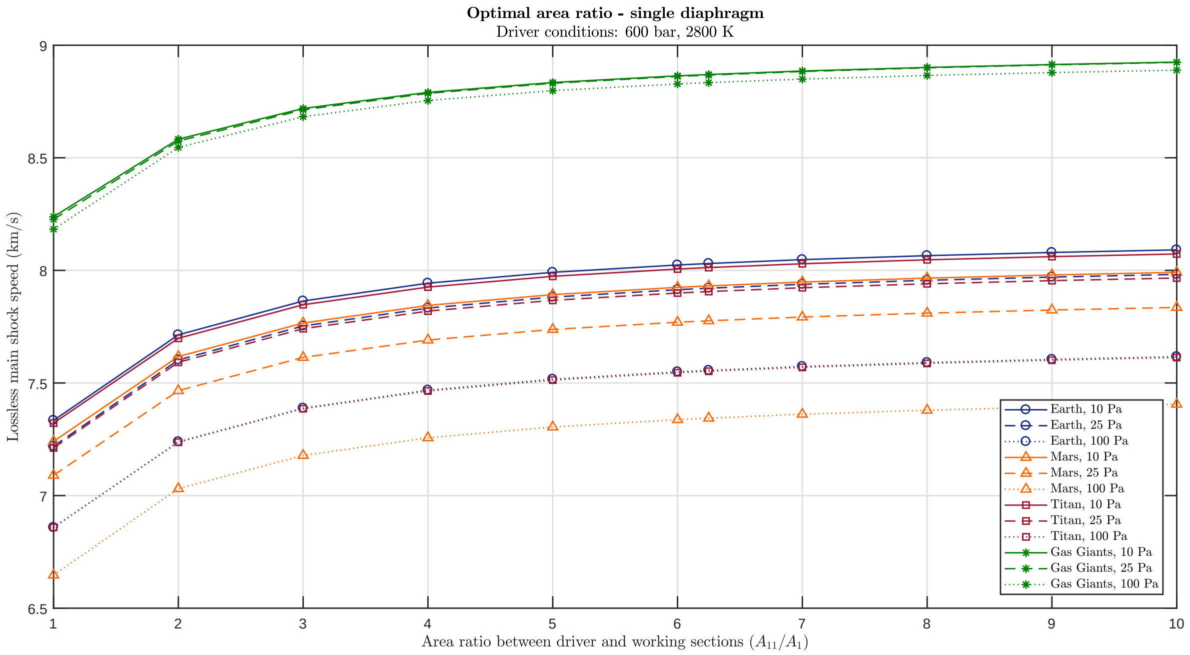

Figure 4.1: Effect of area ratio on shock speed - single diaphragm configuration.

In this example, the shock speed increases in average around 5.4% for a 2:1 area ratio, 8.6% for a 4:1, 9.9% for a 6.25:1 and 10.7% for a 10:1 area ratio. Although these are continuous gain increments for higher area ratios, the gains become progressively less and a trade-off between cost of build against performance is required. Therefore, a area ratio of 6.25:1 was chosen, as a practical upper limit as with the Convair shock tunnel [124].

For working pressures of 10 Pa, 25 Pa and 100 Pa, increasing the area ratio from 1 to 10 increases the shock speeds, respectively, around 10.3%, 10.6% and 11.06%, for Earth and Titan's atmosphere, 10.4%, 10.5% and 11.4%, for Mars' and 7.7%, 7.8% and 7.9% for Gas Giants'. Hence, for the same atmosphere, the gain is more significant for test gases at higher pressures and for the same test gas pressure, the gains are higher for lower working test gas γ.

4.1.2 Double diaphragm design with area change

Given the overall driver to working sections diameter ratio, the compression tube must be optimized to provide the highest working section shock speed. As previously discussed, an overall driver to working area ratio of 6.25 is considered. The obtained shock speeds consider an optimal intermediate pressure, calculated by STAGG.

From figure 4.2, and independently of the test gas type and pressure, the optimal driver to intermediate area ratio occurs at about 2 for the 6.25:1 overall ratio. This corresponds to an intermediate to working area ratio of about 3.

The ESTHER shock tube internal diameter was selected to be 80 mm. This size is justified by the ease of access and manipulation of optical windows or sensors inside the tube [124], based on direct experiences from operations of the VUT-1 and TCM2 shock tubes. Thus, for a 80 mm diameter shock

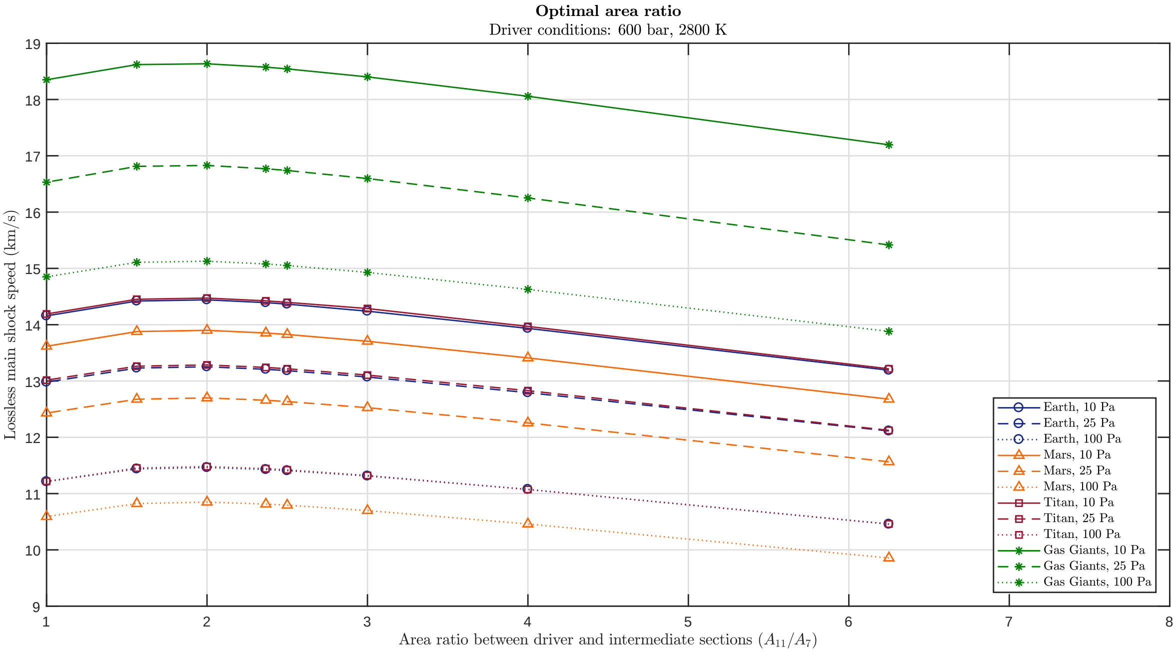

Figure 4.2: Effect of area ratio on shock speed - double diaphragm configuration.

tube, the second stage internal diameter should be 138.5 mm. Taking a rounded down number, as a way of reducing cost and simplifying manufacture, this gives the diameter of each of ESTHER sections: 80 mm for the working, 130 mm for the intermediate and 200 mm for the driver sections.

4.1.3 Driver section performance

Figure 4.3 shows the shock speed gain as a function of the driver pressure for a single diaphragm with an area ratio of 6.25:1 and a double diaphragm with ESTHER configuration, shown in figures 4.3a and 4.3b, respectively. The intermediate pressures are also considered optimal and calculated by STAGG. Only Earth, Mars and Gas Giants' atmospheres are represented since, for a single diaphragm configuration, shock speeds using Titan's atmosphere are only marginally lower than for Earth's (figure 4.1) and, for a double diaphragm atmosphere, marginally higher (figure 4.2).

From figure 4.3, the maximum shock speed is achieved for a maximum driver pressure (as would be expected). Moreover, as expected, the obtainable maximum shock speed is also higher for higher driver to working pressure ratios. However, a maximum working driver pressure of 600 bar after combustion must not be exceeded due to ESTHER's mechanical design constrains [124].

For a single diaphragm configuration (figure 4.3a), the shock speed gain for a working pressure of 10 Pa is 3.2% and 4.3% and for a working pressure of 100 Pa is 10.0% and 11.2%, for Earth and Mars' atmospheres, respectively.

From figure 4.3b and for a driver pressure of 600 bar, the lossless shock speed reaches up to 14.39 km/s for Earth and around 13.85 km/s for Mars. Comparing the lowest and highest driver pressures, for a working pressure of 10 Pa, there is a gain of 14.9% and 15.8% and for a working pressure of 100 Pa, a gain of 19.1% and 20.1%, for Earth and Mars, respectively.

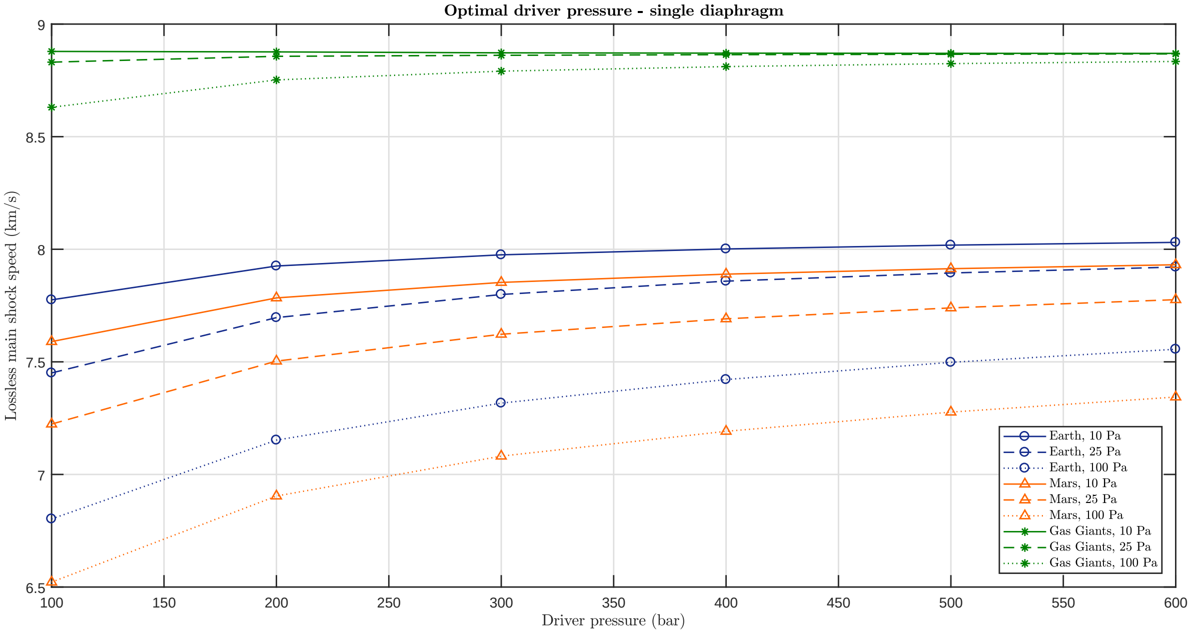

(a) Single diaphragm

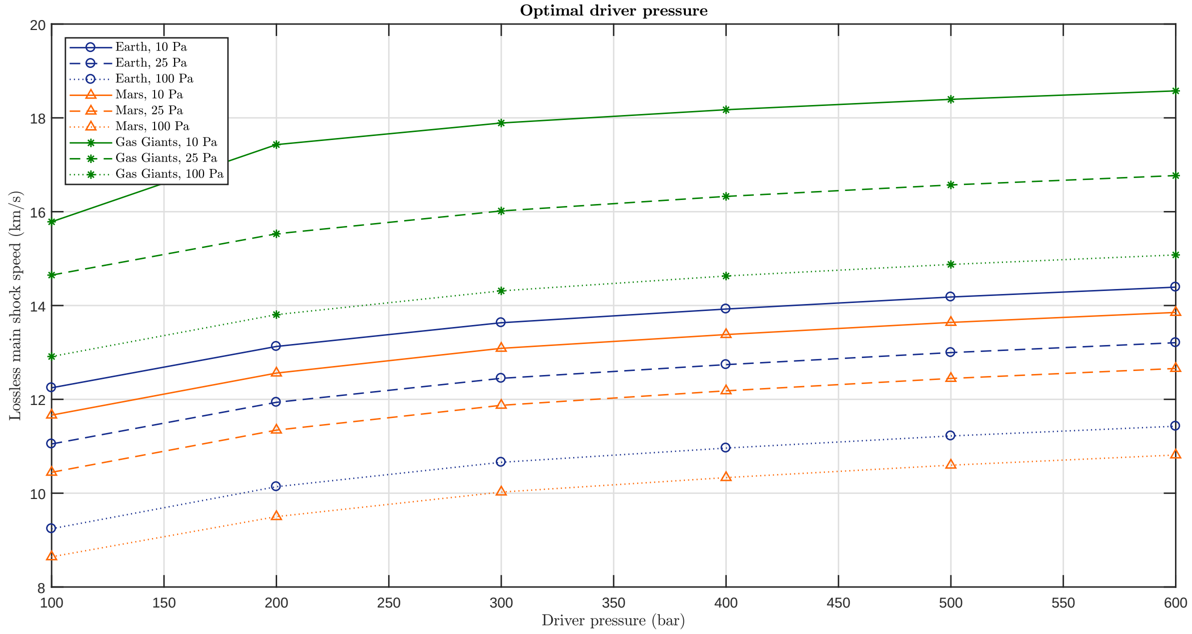

(b) Double diaphragm

Figure 4.3: Effect of driver pressure on shock speed.

Comparing both single and double configuration, for a working pressure of 10 Pa, the gains vary between 36.5% (low driver pressures) and 44.2% (high driver pressures) and for 100 Pa, the gains vary between 24.5% (low driver pressures) and 33.9% (high driver pressures). Summarizing, adding an intermediate section can increase the gains significantly. When comparing the gains of adding an intermediate section, these are higher for low working pressures and for higher values of γ.

4.1.4 Intermediate pressure optimization with constant area

As verified in the previous section, there are significant gains when adding an intermediate section to a shock tube. Additionally, the maximum gain for the shock speed is obtained for a certain value of the intermediate pressure [156]. A two stage shock tube provides a considerable performance gain, if the second stage pressure is optimal.

In figure 4.4, a shock speed peak for an optimum intermediate pressure is clearly seen. However, that peak changes with the driver and working properties. For the same driver conditions, the optimal intermediate pressure is increased at higher working pressures. When decreasing the driver pressure and keeping the same working pressure, the optimum intermediate pressure decreases.

For a driver pressure of 600 bar (figure 4.3b), comparing the worst and best shock speeds, for a 10 Pa working section, the shock speed gain is around 28.4% for Earth's atmosphere and around 31.9% for Mars'; when increasing to 100 Pa, the gains are around 50.2% for Earth's and 54.9% for Mars'.

4.1.5 Intermediate pressure optimization with area change

In section 4.1.2, the influence of the area change in the shock speed due to an intermediate section was analysed. It was concluded that, for an optimal driver to working area ratio, the gains are significant. Thereafter, the optimal area ratio previously chosen is taken into account to study the gains when comparing to the unitary area ratio case (section 4.1.4).

For this configuration, at a 10 Pa working pressure, the shock speed gains are around 29.3% for Earth's atmosphere and 33.6% for Mars'; and for a 100 Pa working pressure, the gains are 50.2% for Earth's and 54.5% for Mars'.

As expected, figures 4.4 and 4.5 have the same pattern. Comparing the latter with figure 4.4a (same driver conditions), for the same initial atmosphere, the shock speeds have an overall gain of around 20% when using the optimized area ratio instead of a unitary one.

4.2 Disturbance effects

In this section, the influences caused by the area ratio changes for the cases with one and two diaphragms are analysed, taking into account disturbance effects, such as the formation of a wall boundary layer and a blast wave. Regarding wall losses, both Milne and Mirels' theories are applied. For the test section, Earth, Mars, Titan and Gas Giants' gases are considered.

Table 4.1 summarizes the initial properties considered for the driver and intermediate sections. Each of the section pressures depends on the atmosphere to be simulated and are discussed in their respec-

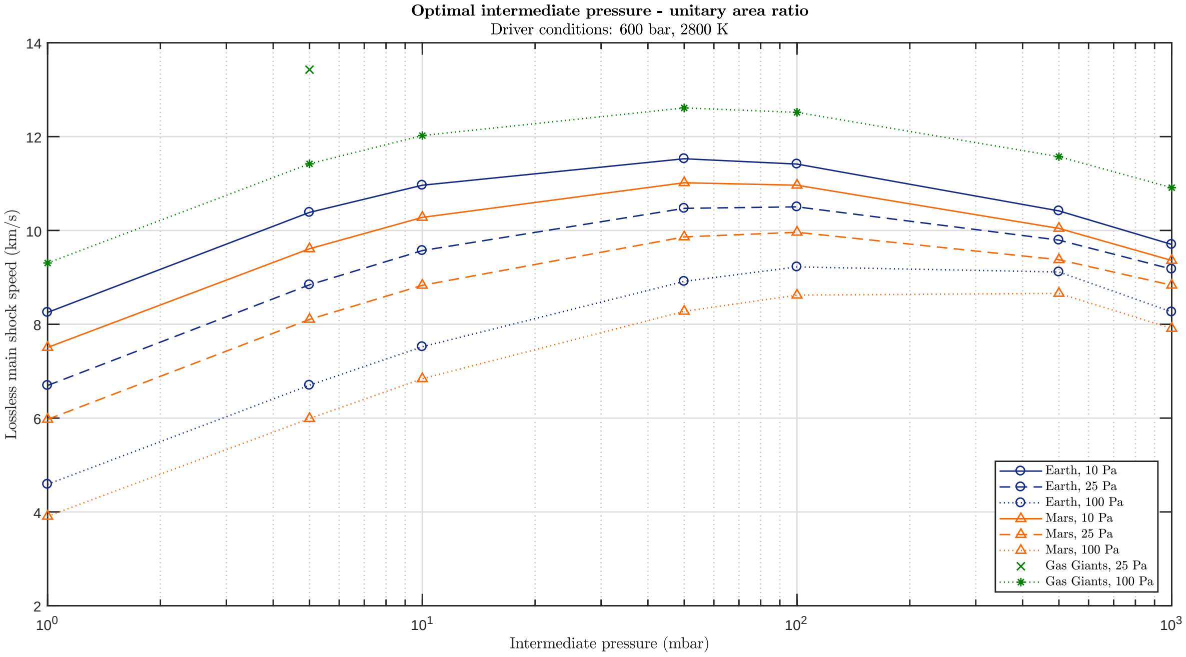

(a) Driver pressure: 600 bar

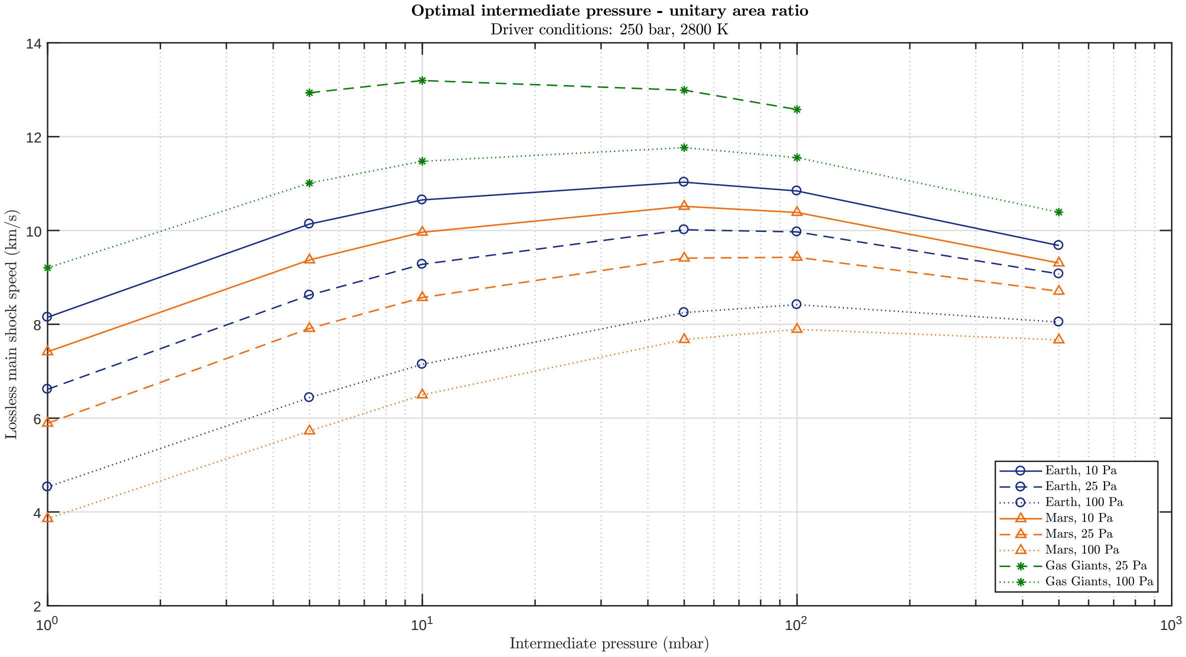

(b) Driver pressure: 250 bar

Figure 4.4: Effect of intermediate pressure on shock speed - unitary area ratio.

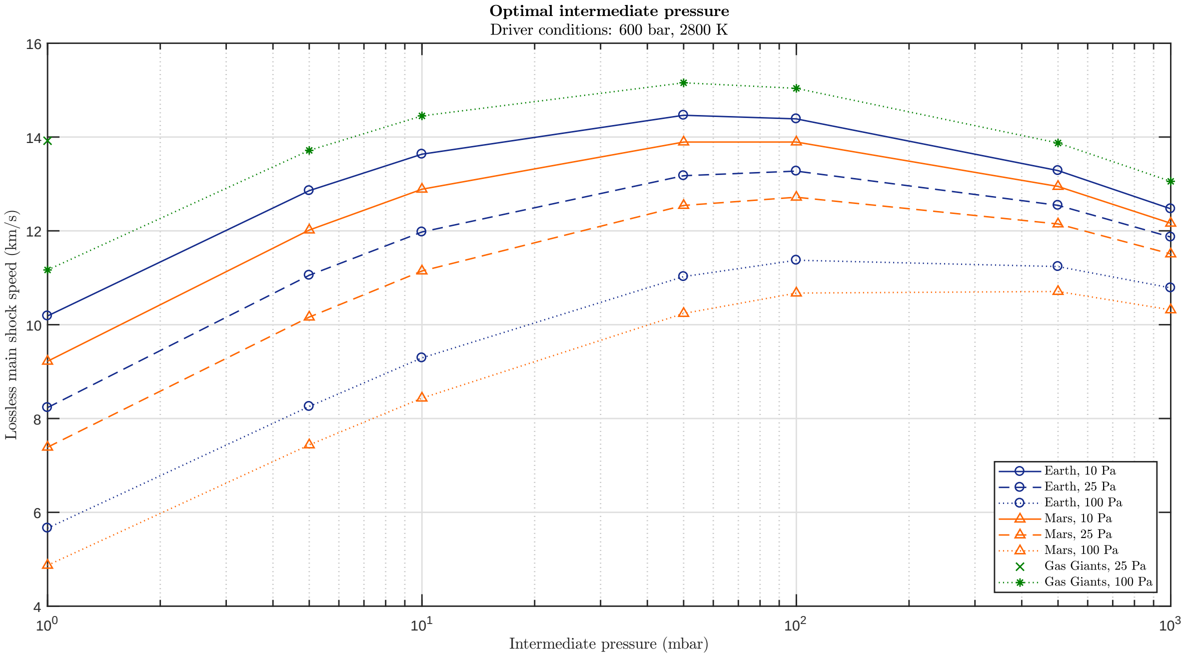

Figure 4.5: Effect of intermediate pressure on shock speed.

tive subsection. The temperature of the working pressure is 300 K and the specific heat ratio and the molar mass are use directly from the CEA file, instead of the values introduced by the user [13].

Table 4.1: Initial properties considered.

	Section	
	Driver (state 11)	Intermediate (state 7)
Temperature (T, in K)	2800	300
Specific heats ratio (γ)	1.56	1.667
Molar mass ($\mathcal{M}$, in g/mol)	7.1	4.0
Gas composition	7:2:1 He:H_2:O_2	Ideal [2]

4.2.1 Test atmosphere: Earth

The initial selected properties correspond to the best performance, for Earth's atmosphere, as predicted in section 4.1. The driver pressure is 600 bar. The simulated gas composition is 78% N_2, 21% O_2, 1% Ar. Each intermediate pressure is calculated, using STAGG code, to obtain the optimal value for the given driver conditions, applying the relations from section 3.1.3, based on Walenta [123]. Alongside the respective area ratio for each possible shock tube configuration, the intermediate pressure obtained for each case is represented in table 4.2.

---

[2] The intermediate section gases in double diaphragm tubes must be ideal in the current version of STAGG, which is a good approximation if Helium is used [13].

Table 4.2: Intermediate pressures for Earth's atmosphere.

Configuration	Area ratio (first diaphragm, A_{11}/A_7)	Area ratio (second diaphragm, A_7/A_1)	Intermediate pressure (p_7, in mbar)
1	1	-	-
2	6.25	-	-
3	1	1	102.7
4	6.25	1	108.8
5	1	6.25	91.0
6	2.3667	2.6406	98.4

Lossless case

As discussed previously, for the configurations of a double diaphragm shock tube, past a certain time the primary shock wave reaches the second diaphragm. After a short delay, this diaphragm breaks and a main shock wave is generated, with greater velocity than the primary shock wave. This can be analysed in table 4.3.

Table 4.3: Results with no losses for Earth's atmosphere.

Configuration	Intermediate shock speed (u_{s7}, in km/s)	Intermediate Mach number (Ma$_7$)	Working shock speed (in km/s)	Working Mach number (Ma$_1$)	Test time: inviscid (in μs)
1	-	-	7.333	21.1	33.4
2	-	-	8.030	23.3	29.4
3	6.857	6.7	11.817	34.0	20.5
4	7.629	7.4	13.191	38.0	18.0
5	6.943	6.8	14.156	40.8	16.3
6	7.413	7.3	14.392	41.5	16.0

Based on this table, for a single diaphragm configuration, the working shock speed increases 8.68% when changing the area ratio from 1 to 6.25 (configurations 1 and 2). When adding another section and, consequently, another diaphragm, the working shock speed increases 37.9% while keeping the area ratios equal to 1 (comparing configuration 1 and 3).

Comparing the cases with single and double diaphragms, both with optimal area ratio (configurations 2 and 6), the shock speed gain is 44.2%. However, for all the previous cases, the inviscid test time decreases approximately by the same percentage.

Boundary layer effects

On the case of an actual shock tube, there is a development of a wall boundary layer that alters the velocity of the main shock wave and main contact surface. The boundary layer effects on the driver gas can be neglected since, in these cases, the shock is strong. Applying Milne's [139] theory (equations from section 3.3.2), the losses for the shock wave throughout all the working section are computed and, then, subtracted to the shock velocity on the lossless case, obtaining the working speed and wall loss velocity (columns 2 and 3 from table 4.4), at the observing point, 4 meters after the position where the main shock wave is generated.

Table 4.4: Results with wall losses for Earth's atmosphere.

Configuration	Working shock speed (with wall losses, in km/s)	Wall loss velocity (in m/s)	Test time: viscous (Milne [139]) (in μs)	Test time: viscous (Mirels [57]) (in μs)
1	7.279	55.0	33.0	4.0
2	7.976	54.8	29.1	3.5
3	11.763	53.7	20.4	2.7
4	13.138	53.4	17.9	2.7
5	14.103	53.3	16.2	2.7
6	14.339	53.2	15.9	2.8

Then, there are two possible methods to estimate the test time accounting for wall losses. First, by calculating the contact surface velocity using the same algorithm as implemented for the shock velocity (from section 3.3.2) and replacing the ideal shock velocity, u_s, temperature, T_s, and density, ρ_s, respectively, by the ideal contact surface velocity, u_2, temperature, T_2, and density, ρ_2. When applying this algorithm, the test time may be obtained by subtracting the inverses of the contact surface velocity and shock speed, both with losses, reaching the final values from column 4 in table 4.4.

The other method uses Mirels' theory, from section 3.3.1, which computes the test time based on correlations from experimental observations. These results are presented in column 6 from table 4.4. As Mirels [57] mentions, for this approach it was assumed that the flow between the shock and contact surface is steady at each instant but that the contact surface is receding from the shock, which is *"somewhat in error but should give at least qualitatively correct results"*. He also states that *"it appears that the present estimates for β_1 are correct for about 10% from $M_s \geq 5$"* and *"additional experimental data are required to define β"*.

For both approaches, the pattern is the same: as the working shock speed increases, the test time decreases. However, the test time obtained in each method differs substantially. To study the influence of the initial driver to working pressure ratio on the wall losses and test times, the initial working pressure has been changed.

Initial working pressure change

To analyse the boundary layer effect for an initial driver to working pressure ratio lower than the previous case, the working pressure is increased to 25 Pa and 100 Pa. The driver pressure is kept unchanged at 600 bar. Only configurations 2 and 6, which correspond to ESTHER single and double diaphragm configurations, are analysed. The working pressure and respective optimal intermediate pressure are summarized in table 4.5 and the results obtained for the shock speeds and test times, both with and without losses are presented in table 4.6, for each case of working pressures.

Table 4.5: Intermediate pressures for Earth's atmosphere.

Intermediate pressure (p_7, in mbar)	Working pressure (p_1, in Pa)
151.6	25
294.1	100

Table 4.6: Results, with and without wall losses, for Earth's atmosphere.

(a) Single diaphragm configuration.

Working pressure (p_1, in Pa)	Lossless working shock speed (in km/s)	Test time: inviscid (in μs)	Working shock speed (with wall losses, in km/s)	Wall loss velocity (in m/s)	Test time: viscous (Milne) (in μs)	Test time: viscous (Mirels) (in μs)
25	7.921	31.0	7.877	43.6	30.7	7.7
100	7.556	35.4	7.525	30.9	35.2	17.5

(b) Double diaphragm configuration.

Working pressure (p_1, in Pa)	Lossless working shock speed (in km/s)	Test time: inviscid (in μs)	Working shock speed (with wall losses, in km/s)	Wall loss velocity (in m/s)	Test time: viscous (Milne) (in μs)	Test time: viscous (Mirels) (in μs)
25	13.208	18.6	13.165	42.5	18.7	5.3
100	11.427	24.3	11.397	30.3	24.3	12.0

As expected, the comparison with the same configurations shows that, when decreasing the initial pressure ratio (p_{11}/p_1), the shock speeds decrease and, consequently, the test time increases. Nevertheless, these changes are not proportional. Comparing the gains for a working pressure change from 10 Pa to 25 Pa, for single and double diaphragm configurations respectively, there is only an decrease of 1.3% and 8.2% for the shock speeds, while there is an increase of the viscous test time of 5.2% and 14.7% (by Milne's theory) and 54.5% and 50% (by Mirels' theory). Increasing the working pressure 10 times to 100 Pa, for both single and double diaphragm configurations, the shock speed decreases 5.8% and 20.5% and the viscous test time increases 17.4% and 34.5% (by Milne's theory) and 80.0% and 76.9% (by Mirels' theory).

This significant difference in the viscous test time calculated by Mirels' theory may be related with the working pressure difference and, consequently, to the decrease of the Mach number, since Mirels' theory is deducted for weak shock speeds.

Initial driver pressure change

To obtain weaker shock speeds, the initial driver pressure is decreased to 250 bar. All the other properties remain unchanged, except the intermediate pressures that are optimized for this driver pressure. The optimized intermediate pressures, for working pressures of 10 Pa, 25 Pa and 100 Pa, are shown in table 4.7. The obtained results are summarized in table 4.8.

Table 4.7: Intermediate pressures for Earth's atmosphere.

Intermediate pressure (p_7, in mbar)	Working pressure (p_1, in Pa)
65.7	10
101.4	25
197.1	100

Comparing the results obtained for a driver pressure of 250 bar with the ones for a driver pressure of 600 bar, for a single diaphragm configuration, the differences are relatively small. For working pressures

Table 4.8: Results, with and without wall losses, for Earth's atmosphere.

(a) Single diaphragm configuration.

Working pressure (p_1, in Pa)	Lossless working shock speed (in km/s)	Test time: inviscid (in μs)	Working shock speed (with wall losses, in km/s)	Wall loss velocity (in m/s)	Test time: viscous (Milne) (in μs)	Test time: viscous (Mirels) (in μs)
10	7.956	29.8	7.901	54.8	29.4	3.6
25	7.757	31.8	7.714	43.6	31.6	7.9
100	7.248	37.5	7.217	31.0	37.4	18.5

(b) Double diaphragm configuration.

Working pressure (p_1, in Pa)	Lossless working shock speed (in km/s)	Test time: inviscid (in μs)	Working shock speed (with wall losses, in km/s)	Wall loss velocity (in m/s)	Test time: viscous (Milne) (in μs)	Test time: viscous (Mirels) (in μs)
10	13.386	17.6	13.333	53.4	17.5	2.7
25	12.201	20.8	12.158	42.7	20.8	5.5
100	10.403	26.9	10.373	30.4	26.8	12.9

of 10 Pa, 25 Pa and 100 Pa, shock speeds only decrease 0.9%, 2.1% and 4.1%, while the test times increase more significantly by 1.1%, 2.7% and 5.7% (by Milne's theory) and 1.3%, 2.9% and 5.6% (by Mirels' theory), respectively.

For a double diaphragm configuration, the differences on the achievable shock speed become more noticeable. For working pressures of 10 Pa, 25 Pa and 100 Pa, the shock speeds decrease 7.0%, 7.6% and 9.0%, while the test times increase 9.0%, 10.1% and 9.3% (by Milne's theory) and 3.3%, 3.5% and 7.2% (by Mirels' theory).

Non optimized intermediate pressure

To obtain the weakest shock speeds, the initial driver pressure is decreased to 100 bar. All the other properties remain unchanged, except the intermediate pressures are chosen to obtain the lowest possible shock speeds. Based on figures 4.4 and 4.5, this intermediate pressure is 1 mbar. The obtained results are summarized in table 4.9.

For a single diaphragm configuration, comparing the results for driver pressures of 600 bar to driver pressures of 100 bar, the shock speeds decrease only 3.2%, 6.0% and 10.1%, respectively for 10 Pa, 25 Pa and 100 Pa, and the test times increase 4.0%, 8.4% and 15.0% (by Milne's theory) and 5.4%, 8.3% and 14.6% (by Mirels' theory).

For a double diaphragm configuration, the differences between the worst performance (driver pressure of 100 bar and intermediate pressure of 1 mbar) and the best performance (driver pressure of 600 bar and optimized intermediate pressure, from table 4.4) are highly significant. The shock speeds decrease 32.9%, 40.9% and 53%, comparing working pressures of 10 Pa, 25 Pa and 100 Pa, respectively, while the viscous test times increase 40.2%, 41.9% and 61.9% (by Milne's theory) and 3.4%, 32.1% and 60.9% (by Mirels' theory).

Comparing the extreme cases - 1) driver pressure of 600 bar, optimized intermediate pressure and

Table 4.9: Worst performance results, with and without wall losses, for Earth's atmosphere.

(a) Single diaphragm configuration.

Working pressure (p_1, in Pa)	Lossless working shock speed (in km/s)	Test time: inviscid (in μs)	Working shock speed (with wall losses, in km/s)	Wall loss velocity (in m/s)	Test time: viscous (Milne) (in μs)	Test time: viscous (Mirels) (in μs)
10	7.774	30.7	7.720	53.9	30.3	3.7
25	7.450	33.8	7.407	42.5	33.5	8.4
100	6.803	41.6	6.772	31.1	41.4	20.5

(b) Double diaphragm configuration.

Working pressure (p_1, in Pa)	Lossless working shock speed (in km/s)	Test time: inviscid (in μs)	Working shock speed (with wall losses, in km/s)	Wall loss velocity (in m/s)	Test time: viscous (Milne) (in μs)	Test time: viscous (Mirels) (in μs)
10	9.675	26.8	9.620	54.5	26.6	2.9
25	7.823	31.5	7.780	43.3	32.2	7.8
100	5.392	63.9	5.360	31.6	63.7	30.7

working pressure of 10 Pa and 2) driver pressure of 100 bar, intermediate pressure of 1 mbar and working pressure of 100 Pa - there is an overall increase of 62.6% in the obtained shock speed.

Wave diagrams

Figures 4.6 and 4.7 represent a position time ($x-t$) diagram for the different shock tube configurations (repeated in annex B.2, from figure B.1 to B.6), for the best performance case for Earth's atmosphere. To design the diagrams, a MATLAB code was devised for both single and double diaphragm shock tube configurations. The program calculates the achievable shock speed based on the optimal intermediate pressure extracted from STAGG, post shock states, based on Walenta [123], wall losses based on Milne's theory [139], and test times using both Milne and Mirels' [57] theories. The reflection of the expansion wave head on the wall and consequent interaction with the other expansion waves, which accelerates the expansion waves, is employed using the method of characteristics. For the second diaphragm opening, the *holding time* model is considered, with conservative hold time of 30 μs (based on Furukawa et al.[144] experiments).

The ideal and non-ideal shock waves are represented with black and red bold lines, respectively, and the ideal contact surface with a black dashed line. The contact surface calculated using Mirels' approach is represented with a dashed and point red line and, by Milne's method, with a dashed red line. The expansion waves are represented in black. Finally, the opening delay for the second diaphragm is represented by a dashed light blue line. The dashed dark blue line corresponds to the position for observation at $x = 4$ m and $x = 8$ for single and double diaphragm configurations, respectively.

1. Single diaphragm shock tube

For a single diaphragm shock tube, after diaphragm rupture, non-steady expansion waves expand into both sections, due to the pressure difference between sections. At diaphragm stage, the gas undergoes a sonic steady expansion (state 9) before it unsteadily expands into the driver section (becoming state 10) and into the working section (becoming state 3). For a constant cross-section area shock tube, state 10 of the gas is sonic, otherwise subsonic. The expansion waves that move into the high pressure section decrease continuously the pressure and temperature in region 11 to the lower pressure and temperature value in region 10. Moreover, a shock wave and contact surface are generated (state 1 and 2, respectively).

Following Tasissa et al.'s [140] algorithm to compute the Friedlander wave in a shock tube (section 3.3.3), the onset time and location of Friedlander waves are given in table 4.10. The time and location correspond to the instant and point, respectively, where the head wave encounters the shock front. In figures 4.6, these points correspond effectively to the intersection of the head of the expansion wave and the shock wave.

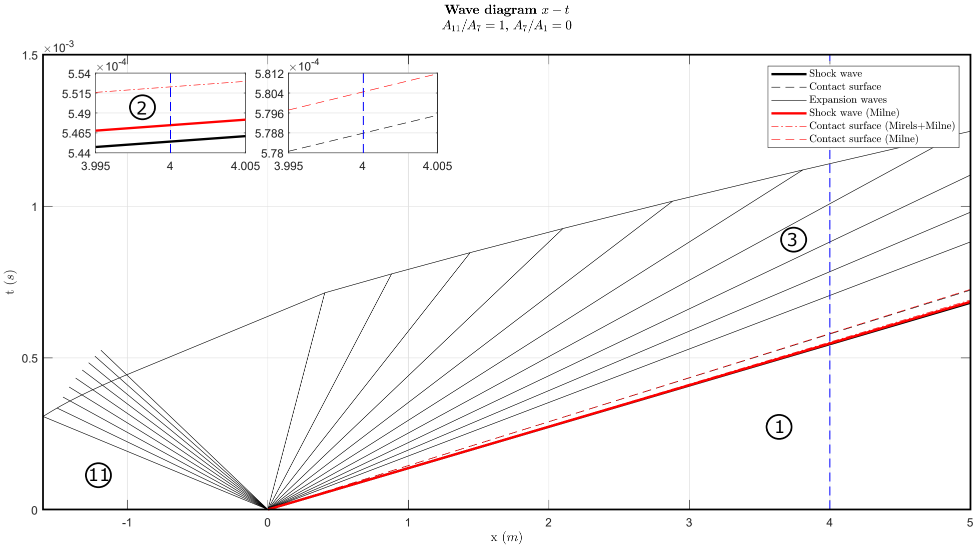

(a) Shock tube with constant area.

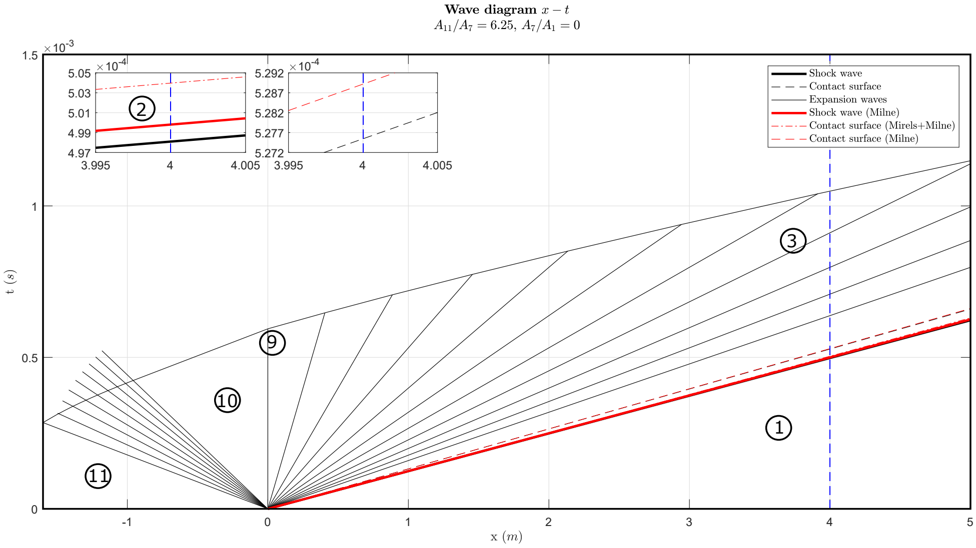

(b) Shock tube with variable area.

Figure 4.6: Wave diaphragms for single diaphragm shock tubes.

This method allows verifying that the intersection of the head of the expansion wave reflected on the left side wall with the shock wave occurs long after the observation window, at $x = 4$ m. Comparing

Table 4.10: Time of onset and location of Frielander wave.

Configuration	Time on onset (in s)	Location (in m)
1	0.108	796.6
2	0.099	799.8

figures 4.6a and 4.6b, for the latter, the reflected wave on the left side end wall reaches a higher velocity. Thereafter, the time before the blast wave can form is shorter than for the weaker shock wave. Indirectly, these results also validate the characteristic method employed in the wave diagram.

Summarizing based on theses results, for the ESTHER single diaphragm configuration, the blast wave initiation length is much longer than the actual shock tube length.

2. Double diaphragm shock tube

When the shock tube has two diaphragms, once the first one is ruptured, the non-steady expansion waves originate state 10 inside the driver section and state 8 inside the intermediate section, under the same conditions as in the simple diaphragm case. The primary shock wave originated has a velocity u_{s7} (becoming state 7). Once this shock wave reaches the secondary diaphragm, the primary shock wave reflects (state 5) and there is a delay before rupture. Hence, the *holding time* method is applied and local expansion waves are generated.

Once the diaphragm ruptures, the shock test gas (state 6) starts to unsteadily expand into the working section (from state 4 until becoming state 3), increasing the velocity and decreasing the pressure and temperature. The state 3 gas drives a shock wave through the test gas (state 1) and processes it to state 2, lowering the velocity and increasing the pressure and temperature.

Even though Tasissa et al.'s [140] algorithm is only applicable to single diaphragm configurations, figures 4.7 show that the intersection of the head of the expansion wave reflected on the left side wall and the shock wave occurs long after the test window.

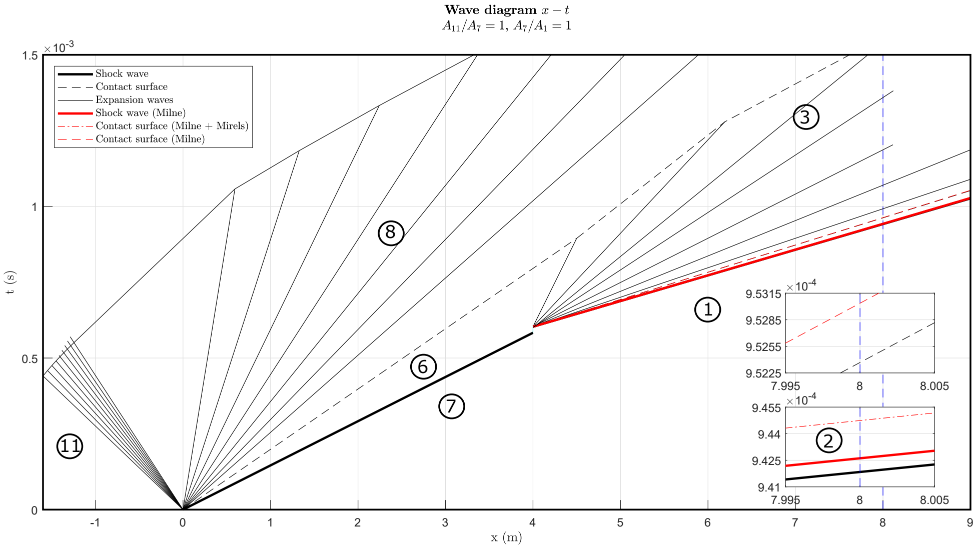

(a) Shock tube with no cross-section area reductions.

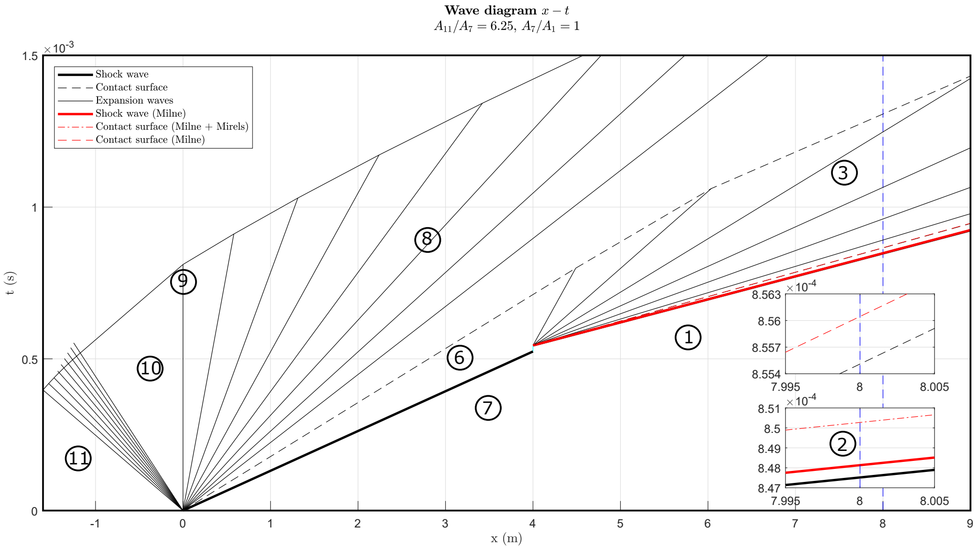

(b) Shock tube with cross-section area reduction at the first diaphragm.

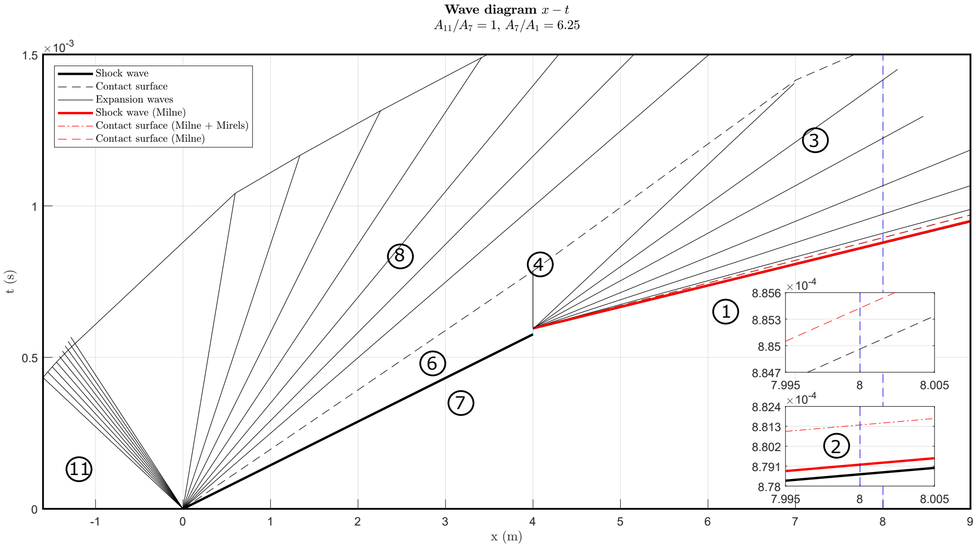

(c) Shock tube with cross-section area reduction at the second diaphragm.

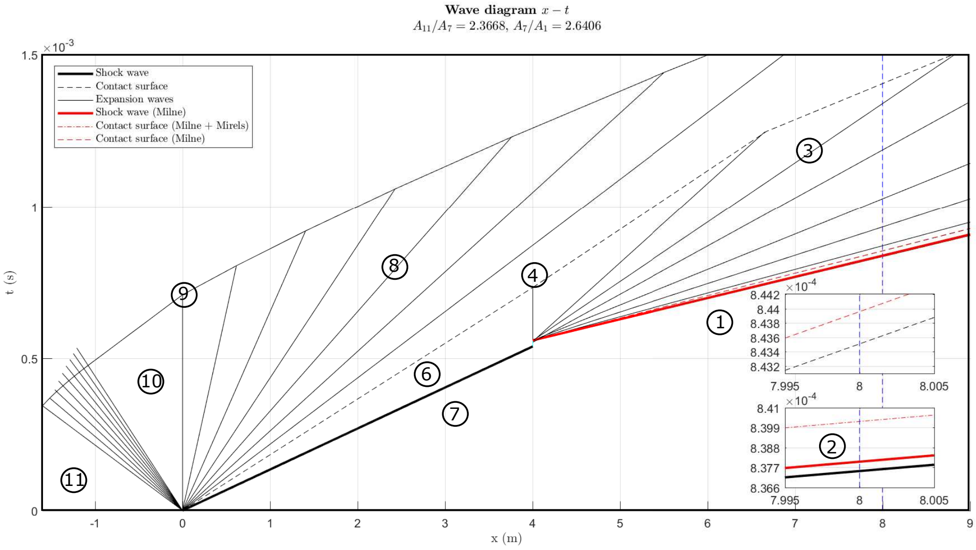

(d) Shock tube with cross-section area reduction at both diaphragms.

Figure 4.7: Wave diagrams for double diaphragm shock tubes.

Nevertheless, the algorithm is applicable considering the properties of intermediate shock (instead of the working pressure), determining where and when the head of the reflected wave intersects the primary shock wave. The results for the different configurations are presented in table 4.11. The time expected for the shock wave to reach the test window is also presented in the table.

Table 4.11: Onset time and location of Frielander wave.

Configuration	Onset time (in s)	Location (in m)	Experiment time (s)
3	0.021	147.1	9.5e-4
4	0.019	144.4	8.0e-4
5	0.022	154.8	8.3e-4
6	0.020	150.5	7.9e-4

Based on the observation of figures 4.7 and analysing table 4.11, the interaction of the head of the reflected expansion wave with the primary shock wave is expected to occur long after the experiment is over. Nevertheless, the results for double diaphragm configurations (table 4.11) predict that the interaction occurs sooner than for a single diaphragm one. For the double configuration, even though the expansion wave is slower, the contact surface is even slower. Once the interaction occurs, the expansion wave is accelerated, but the interaction with the shock wave will take longer to occur than for the single diaphragm configuration. Hence, for the double diaphragm configuration, the onset of the blast wave will occur much later.

After a few test campaigns successfully done in the nominal configuration, a reduction of the combustion chamber may be considered. Consequently, this would mean a reduction of the fill volume, filling time and, therefore, shot cost.

4.2.2 Test atmosphere: Mars and Venus

As presented in table 1.1, Mars and Venus' atmospheres are constituted by the same primary compounds and have a very similar mean molecular weight. Hence, even though STAGG's directory gathers Mars information, Venus can also be simulated using the same file.

From figure 4.3, Mars entry speeds may be simulated using a single diaphragm. On the other hand, Venus entry speeds are higher, and the second diaphragm configuration is necessary for simulating its entry speeds. Therefore, both ESTHER single and double diaphragm configurations are studied.

The driver pressure is 600 bar. The working gas has a molar composition of 95.7% CO_2, 2.7% N_2 and 1.6% Ar. The corresponding intermediate pressures for each working pressure are presented in table 4.12. For each case, the algorithms implemented in section 4.2.1 are repeated and the results obtained with and without wall losses are shown in table 4.13.

For a single diaphragm configuration, the expected shock speeds vary between 7.32 km/s and 7.88 km/s and the viscous test times between 26.0 μs and 32.4 μs, applying Milne's algorithm, and between 4.7 μs and 18.6 μs, using Mirels' theory.

Confronting the results for a working pressure of 10 Pa with a working pressure of 25 Pa, there is a decrease of the shock speeds by 1.9% and 8.6%, while the viscous test times increase 5.7% and

Table 4.12: Intermediate pressures for Mars' atmosphere.

Intermediate pressure (p_7, in mbar)	Working pressure (p_1, in Pa)
119.0	10
183.7	25
356.2	100

Table 4.13: Results, with and without wall losses, for Mars' atmosphere.

(a) Single diaphragm configuration.

Working pressure (p_1, in Pa)	Lossless working shock speed (in km/s)	Test time: inviscid (in μs)	Working shock speed (with wall losses, in km/s)	Wall loss velocity (in m/s)	Test time: viscous (Milne) (in μs)	Test time: viscous (Mirels) (in μs)
10	7.931	26.4	7.882	49.5	26.0	4.7
25	7.776	27.9	7.737	39.4	27.6	9.2
100	7.344	32.6	7.316	27.9	32.4	18.6

(b) Double diaphragm configuration.

Working pressure (p_1, in Pa)	Lossless working shock speed (in km/s)	Test time: inviscid (in μs)	Working shock speed (with wall losses, in km/s)	Wall loss velocity (in m/s)	Test time: viscous (Milne) (in μs)	Test time: viscous (Mirels) (in μs)
10	13.853	16.7	13.804	48.2	16.7	3.6
25	12.658	19.3	12.620	38.6	19.2	6.6
100	10.814	22.9	10.786	27.4	22.8	12.7

13.4% (by Milne's theory) and 49.0% and 45.0% (by Mirels' theory), for single and double diaphragm configurations, respectively. Comparing the working pressures of 100 Pa with 10 Pa, the shock speeds decrease 7.3% and 21.9%, while the viscous test times increase 19.7% and 27.0% (by Milne's theory) and 74.7% and 71.6% (by Mirels' theory).

For a double diaphragm configuration, the shock speeds vary between 10.79 km/s and 13.80 km/s, while the viscous test times vary between 16.7 μs and 22.8 μs (by Milne's theory) and 3.6 μs and 12.7 μs (by Mirels' theory). Comparing the results for 10 Pa with 25 and 100 Pa, there is a decrease of the shock speed of 8.58% and 21.86%, while there is an increase of the viscous test times by 13.41% and 27.02% (using Milne's approach) and 45.00% and 71.56% (using Mirels' theory), respectively.

As the driver to working ratio pressures with a single diaphragm configuration still produce higher shock speeds than encountered during Martian entry, the initial driver pressure is decreased. For a double diaphragm configuration, the initial driver pressure is also decreased to analyse if the results are still sufficient for Venusian entries.

Initial driver pressure change

For this simulation, the initial driver pressure is decreased to 250 bar and the remaining initial properties are unchanged. Table 4.14 shows the intermediate pressures for this case. Table 4.15 summarizes the results obtained, for both single and double diaphragm configuration.

Comparing the results from table 4.15a with table 4.13a (single diaphragm configuration), for working

Table 4.14: Intermediate pressures for Mars' atmosphere.

Intermediate pressure (p_7, in mbar)	Working pressure (p_1, in Pa)
79.5	10
122.8	25
238.3	100

Table 4.15: Results, with and without wall losses, for Mars' atmosphere.

(a) Single diaphragm configuration.

Working pressure (p_1, in Pa)	Lossless working shock speed (in km/s)	Test time: inviscid (in μs)	Working shock speed (with wall losses, in km/s)	Wall loss velocity (in m/s)	Test time: viscous (Milne) (in μs)	Test time: viscous (Mirels) (in μs)
10	7.825	26.9	7.776	49.5	26.5	4.8
25	7.575	29.1	7.535	39.5	28.8	9.6
100	7.008	35.0	6.980	28.0	34.8	19.9

(b) Double diaphragm configuration.

Working pressure (p_1, in Pa)	Lossless working shock speed (in km/s)	Test time: inviscid (in μs)	Working shock speed (with wall losses, in km/s)	Wall loss velocity (in m/s)	Test time: viscous (Milne) (in μs)	Test time: viscous (Mirels) (in μs)
10	12.833	18.2	12.785	48.4	18.1	3.5
25	11.614	20.5	11.575	38.6	20.4	6.6
100	9.765	23.4	9.738	27.6	23.3	13.2

pressures of 10 Pa, 25 Pa and 100 Pa, respectively, there is a decrease of only 1.3%, 2.6% and 4.6% of the shock speed and an increase of the viscous test times calculated by Milne's algorithm of 1.9%, 4.2% and 6.8% and of 1.7%, 3.9% and 6.6% calculated by Mirels' theory. Using this driver pressure, speeds between 7.0 km/s and 7.8 km/s are expected to be reached.

Comparing the results for driver pressures of 600 bar (table 4.15b) and 250 bar (table 4.13b), for working pressures of 10 Pa, 25 Pa and 100 Pa, there is a decrease of the shock speeds by 7.36%, 8.25% and 9.69%, respectively. The viscous test time, on the other hand, has smaller gains. Considering Milne's theory, there is an increase of 7.96%, 5.61% and 2.22%, while by Mirels' theory, there is an increase of 2.21%, 1.02% and 3.41%, respectively for 10 Pa, 25 Pa and 100 Pa.

Non optimized intermediate pressure

To obtain the weakest shock speeds, the initial driver pressure is decreased to 100 bar. The intermediate pressure is 1 mbar. All the other properties remain unchanged. The obtained results are summarized in table 4.16.

For a single diaphragm configuration, comparing the results for 100 bar with the ones for 600 bar, the shock speeds decreases 4.3%, 7.1% and 11.2%, respectively for 10 Pa, 25 Pa and 100 Pa, and the test times increase about 6.0%, 10.5% and 14.8%, for both theories.

For a double diaphragm configuration, there are gains of 36.9%, 44.6% and 57.4% for the shock

Table 4.16: Worst performance results, with and without wall losses, for Mars' atmosphere.

(a) Single diaphragm configuration.

Working pressure (p_1, in Pa)	Lossless working shock speed (in km/s)	Test time: inviscid (in μs)	Working shock speed (with wall losses, in km/s)	Wall loss velocity (in m/s)	Test time: viscous (Milne) (in μs)	Test time: viscous (Mirels) (in μs)
10	7.590	28.2	7.540	49.6	27.7	5.0
25	7.223	31.2	7.184	39.5	30.9	10.2
100	6.522	38.5	6.494	28.1	38.2	21.7

(b) Double diaphragm configuration.

Working pressure (p_1, in Pa)	Lossless working shock speed (in km/s)	Test time: inviscid (in μs)	Working shock speed (with wall losses, in km/s)	Wall loss velocity (in m/s)	Test time: viscous (Milne) (in μs)	Test time: viscous (Mirels) (in μs)
10	8.757	22.9	8.709	48.5	22.6	4.1
25	7.025	32.5	6.986	39.1	32.3	10.6
100	4.627	43.4	4.598	29.1	42.7	26.6

speeds, respectively for 10 Pa, 25 Pa and 100 Pa, and 26.1%, 40.6% and 46.6% (by Milne's theory) and 12.2%, 37.7% and 52.3% (by Mirels' theory) for the test times. When comparing the extreme cases, there is an overall gain of 66.7% for the shock speed.

4.2.3 Test atmosphere: Titan

As verified in figures 4.1 and 4.2 and as mentioned in section 4.1.3, for a single diaphragm configuration, shock speeds for Titan's atmosphere are only marginally lower than for Earth's atmosphere while for a double diaphragm configuration, the shock speeds are marginally higher. However, Titan entry speeds are lower than for Earth, hence the shock speeds to be reached using a driver pressure of 250 bar, with a single diaphragm shock tube, are expected to be fast enough. The simulated gas composition contains 98.5% N_2 and 1.5% CH_4. The results obtained with and without wall losses are presented in table 4.17.

Table 4.17: Results, with and without wall losses, for Titan's atmosphere.

Working pressure (p_1, in Pa)	Lossless working shock speed (in km/s)	Test time: inviscid (in μs)	Working shock speed (with wall losses, in km/s)	Wall loss velocity (in m/s)	Test time: viscous (Milne) (in μs)	Test time: viscous (Mirels) (in μs)
10	7.941	28.4	7.886	55.29	28.0	3.5
25	7.751	30.5	7.707	44.06	30.2	7.8
100	7.250	36.0	7.218	31.26	35.8	18.0

From table 4.17, for a single diaphragm configuration, the expected shock speeds are between 7.22 km/s and 7.89 km/s, for working pressures of 100 Pa and 10 Pa, respectively. The viscous test times vary between 28.0 μs and 35.8 μs, using Milne's theory and between 3.5 μs and 18.0 μs, using Mirels' theory.

Nevertheless, the results estimated are still higher than the speed encountered by Huygens, during its entry in Saturn's moon. Hence, the driver pressure is decreased to 100 bar.

Initial driver pressure change

The results obtained for a single diagram configuration and driver pressure of 100 bar are summarized in table 4.18.

Table 4.18: Results, with and without wall losses, for Titan's atmosphere.

Working pressure (p_1, in Pa)	Lossless working shock speed (in km/s)	Test time: inviscid (in μs)	Working shock speed (with wall losses, in km/s)	Wall loss velocity (in m/s)	Test time: viscous (Milne) (in μs)	Test time: viscous (Mirels) (in μs)
10	7.768	29.6	7.713	55.35	28.9	3.6
25	7.451	32.4	7.407	44.15	32.1	8.3
100	6.811	40.1	6.780	31.36	39.9	20.0

Using these properties, the shock speeds vary between 6.78 km/s and 7.71 km/s, while the test times vary between 28.9 μs and 39.9 μs, using Milne's algorithm and between 3.5 μs and 19.8 μs.

Comparing the results for driver pressures of 100 bar and 250 bar, for working pressures of 10 Pa, 25 Pa and 100 Pa, the shock speed decreases 2.2%, 3.9% and 6.0%, while the viscous test times increases 3.1%, 6.0% and 10.2% (by Milne's theory) and 2.9%, 6.0% and 9.8% (by Mirels' theory).

4.2.4 Test atmosphere: Gas Giants

As the entry speeds of the Gas Giants are very high, only a double diaphragm configuration shock tube is analysed, considering a driver pressure of 600 bar. The working gas is composed of 90% H_2 and 10% He[3]. The intermediate pressures and the results obtained for working pressures of 10, 25 and 100 Pa are presented, respectively, in tables 4.19 and 4.20.

Table 4.19: Intermediate pressures for Gas Giants' atmosphere.

Intermediate pressure (p_7, in mbar)	Working pressure (p_1, in Pa)
30.6	10
45.9	25
87.9	100

Table 4.20: Results, with and without wall losses, for Gas Giants' atmosphere.

Working pressure (p_1, in Pa)	Lossless working shock speed (in km/s)	Test time: inviscid (in μs)	Working shock speed (with wall losses, in km/s)	Wall loss velocity (in m/s)	Test time: viscous (Milne) (in μs)	Test time: viscous (Mirels) (in μs)
10	18.575	24.1	18.359	216.1	23.6	1.3
25	16.770	17.1	16.674	96.9	16.9	2.9
100	15.079	22.3	15.022	56.7	22.2	8.6

---

[3] This is representative enough for all the four Gas Giants (Jupiter, Saturn, Uranus and Neptune) composition.

The maximum achievable speeds is around 18.36 km/s, with viscous test times of 23.6 μs and 1.3 μs, for Milne and Mirels' theory, respectively. When increasing the working pressure to 25 Pa and 100 Pa, the shock speeds decrease 9.2% and 18.2%, respectively, while the viscous test time using Mirels' theory increases 55.4% and 85.1%. Contrarily to expected and verified in all previous atmosphere's cases, using Milne's theory, the highest test time is for the highest shock speed. This may mean that the theory underlying assumptions are less adapted for this gas composition.

Non optimized intermediate pressure

To analyse the lowest shock speeds expected, the initial driver pressure is decreased to 100 bar and the intermediate pressure to 1 mbar. All the other properties remain unchanged. The obtained results are summarized in table 4.21.

Table 4.21: Worst performance results, with and without wall losses, for Gas Giants' atmosphere.

Working pressure (p_1, in Pa)	Lossless working shock speed (in km/s)	Test time: inviscid (in μs)	Working shock speed (with wall losses, in km/s)	Wall loss velocity (in m/s)	Test time: viscous (Milne) (in μs)	Test time: viscous (Mirels) (in μs)
10	14.918	20.2	14.660	258.2	18.6	1.4
25	13.275	26.9	13.159	116.0	26.3	4.1
100	10.663	46.8	10.606	57.1	46.7	16.7

Comparing the results for a driver pressure of 600 bar to 100 bar, the shock speeds decrease 20.1%, 21.1% and 29.4%, respectively, while the viscous test times increase 21.2%, 35.7% and 52.5% (by Milne's theory) and 7.1%, 29.3% and 48.5% (by Mirels' theory). For these extreme cases, there is an overall difference of 42.2% in the shock speed.

4.3 Gas substitution

As the previous simulations show, the ESTHER shock tube is not expected to be able to recreate the speeds required to simulate Gas Giants entry. Thereafter, it is important to explore other venues to potentially allow the simulation of the entry conditions in this facility. This section examines how considering a higher amount of helium diluent that the actual entries and how a change to a heavier neon diluent would allow hotter shock layers to be simulated at shock speeds expected to the achievable in ESTHER shock tube. The effect of adding different amounts of argon diluent into air is also analysed. This work is inspired by the same study carried out by James at al. [127] for X2 at the University of Queensland.

4.3.1 Test gas mixtures

Stalker and Edward [126] proposed that for blunt bodies simulation of Gas Giant entry, increasing the molar percentage of helium above the true atmospheric composition, or substituting it with neon, could be used to create hotter shock layer conditions at slower speeds.

Hereafter, two theoretical studies are presented to analyse their respective influences for two specific flow conditions: 1) changing helium or neon diluent fraction in the test gas for Gas Giants condition; 2) adding argon for Earth entry condition. The results are computed using the test gas as ideal, changing the molecular weight and specific heats ratio to the corresponding of each composition. The simplified ideal gas model may be considered an example of a frozen flow model, since it is implied by these assumptions that no chemical change takes place [155]. The pressure driver gas is 600 bar; and three working pressures are considered: 10 Pa, 25 Pa and 100 Pa.

Higher amounts of helium diluent

Figure 4.8 shows how a changing helium diluent fraction affects the test gas composition and performance. The values from figure 4.8a are normalized by the results for 10% He.

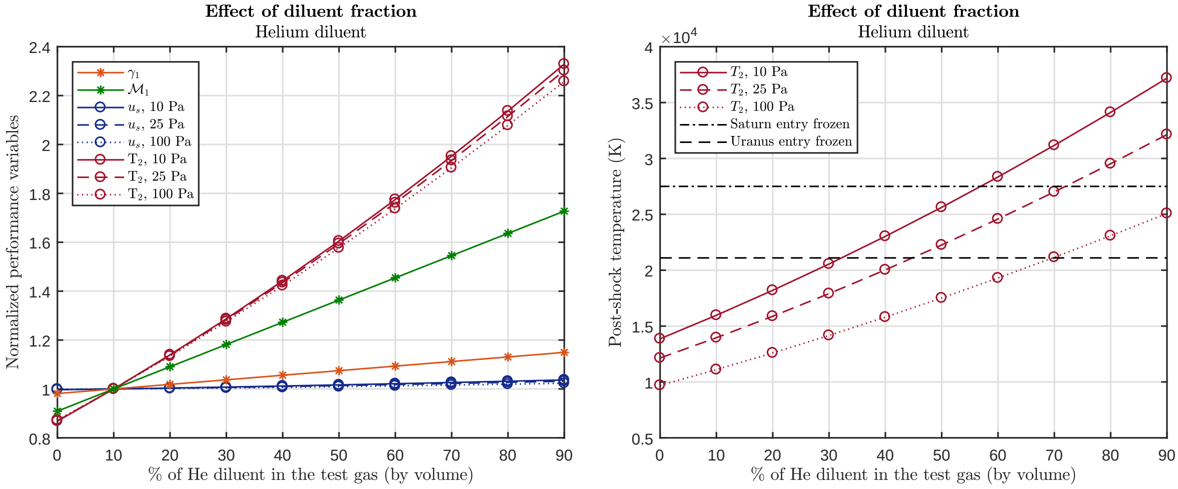

(a) Normalized performance variables.

(b) Post-shock temperature.

Figure 4.8: Effect of helium diluent.

Analysing the effect of the amount of helium diluent into the properties of the test gas (variables γ_1 and $\mathcal{M}_1$), over the full range of helium diluent values shown, there is a increase of around 13.0% in the working specific heat ratio and an increase of around 42.1% in the working molecular weight.

The shock speed (u_s) and post-shock temperature (T$_2$) increase fairly linearly with the amount of helium diluent. Changing from 10% He diluent to 90% He diluent, the shock speed increases only by about 3.8%, while the temperature increases about 56.5%, both almost independently of the working pressure. This shows that the main change made to the flow, by adding more diluent, is to increase the post-shock temperature, simulating a hotter entry.

Figure 4.8b gathers the post-shock temperature results for the different working pressures and Saturn and Uranus entry frozen temperature, extracted from James et al. [127]. The ideal temperature, that may be considered approximately the frozen temperature, varies from around 16, 13 and 11 thousand Kelvin with a 10% He diluent to around 37, 32 and 25 thousand Kelvin for 90% He diluent, respectively for working pressures of 10 Pa, 25 Pa and 100 Pa. To understand what this means practically, it is useful to compare these numbers to proposed Gas Giant entries. Looking to Uranus first, the frozen temperature could be recreated with 32-33%, 43-44% or 69-70% helium fraction in the test gas, depending if the working pressures is 10 Pa, 25 Pa or 100 Pa. Considering Saturn, percentages of 55-56% or 71-72% of helium diluent could be used for working pressures of 10 Pa or 25 Pa. For 100 Pa, the Saturn entry frozen temperature cannot be achieved.

Higher amounts of neon diluent

As previously discussed, Stalker and Edwards [126] examined the use of neon as a substitute for the helium inert diluent in Gas Giants's entry flow fields. This is possible because both helium and neon are noble gases, have similar excitation energy and their computational study showed that, unless the post-shock temperature was above 60 000 K (where the neon begins to ionize), the ionizing relaxation of H_2/Ne test flows were the same as H_2/He test flows. This is useful because neon has a weight five times higher than helium and, consequently, the same amount of neon diluent increases the test gas molecular weight ($\mathcal{M}_1$). This increase of molecular weight of the test gas mixture results in shock layer conditions with significant levels of dissociation and ionization, that can be reproduced at velocities achievable in ground test facilities [127]. This is shown in figure 4.9, where the results from figure 4.9a are normalized by 10% Ne.

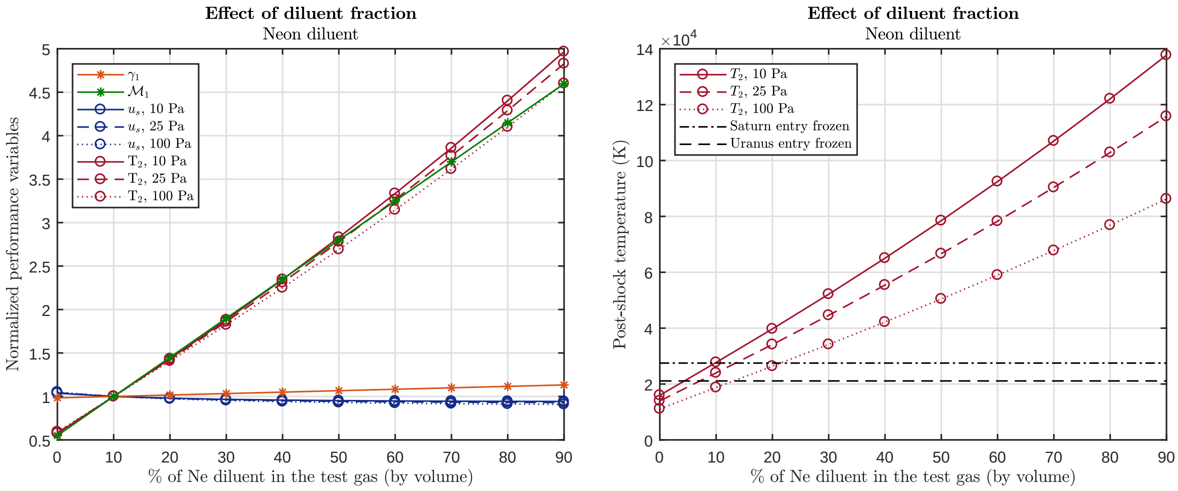

(a) Normalized performance variables.

(b) Post-shock temperature.

Figure 4.9: Effect of neon diluent.

Comparing the effects on the test gas properties with those from the equivalent H_2/He plot (figure 4.8a), much larger changes are seen over the range of different diluent fractions. There is an increase of 11% in the working section specific heat ratio and an increase of 78.3% in the working section molecular weight.

Comparing the molecular weights of the H_2/He and H_2/Ne test conditions, a H_2/He condition with 10% He diluent has a molecular weight of 2.2 g/mol and a H_2/He condition with 90% He diluent has a molecular weight of 3.8 g/mol. The equivalent H_2/Ne conditions have molecular weights of 4.0 g/mol and 18.4 g/mol, respectively. Therefore, the lightest H_2/Ne condition is heavier than the heaviest H_2/He condition considered previously. Regarding specific heat ratios, a H_2/He condition with 10% He diluent has a γ_1 of 1.427 and a 90% He diluent gas a γ_1 of 1.64. The equivalent H_2/Ne conditions have a γ_1 of 1.451 and 1.643. Hence, the specific heats are very similar.

Due to the much higher molecular weights when a H_2/Ne mixture test gas is considered, the flow conditions start to behave differently as the amount of diluent changes. The shock speed decreases linearly around 5.8%, 7.0% and 9.1%, respectively for 10 Pa, 25 Pa and 100 Pa, from the original 10% Ne diluent.

When adding only 10% neon to the H_2/He mixture, the post-shock temperature (T_2) increases around 42%. When introducing 90% He, the post-shock temperature has an increase of 79%, comparing with the original 10% Ne diluent. However, at a normalized temperature of around 2.16 (which corresponds to a temperature of 60 000K), neon begins to ionize and the results are not useful. For working pressures of 10 Pa, 25 Pa and 100 Pa, this phenomena starts at around 35%, 44% or 60% Ne diluent fraction, respectively. Nevertheless, analysing figure 4.9b, the entry frozen temperature of the planets considered are achievable with a percentage of neon considerable lower than those. For Uranus, percentages between 4% and 12% and for Saturn, between 9% and 21% are enough to simulate the planetary entry frozen temperature.

Higher amounts of argon diluent

Figure 4.10 shows how a changing argon diluent into an air mixture affects the test gas composition and the performance. In figure 4.10a, the values are normalized by the results for 10% Ar.

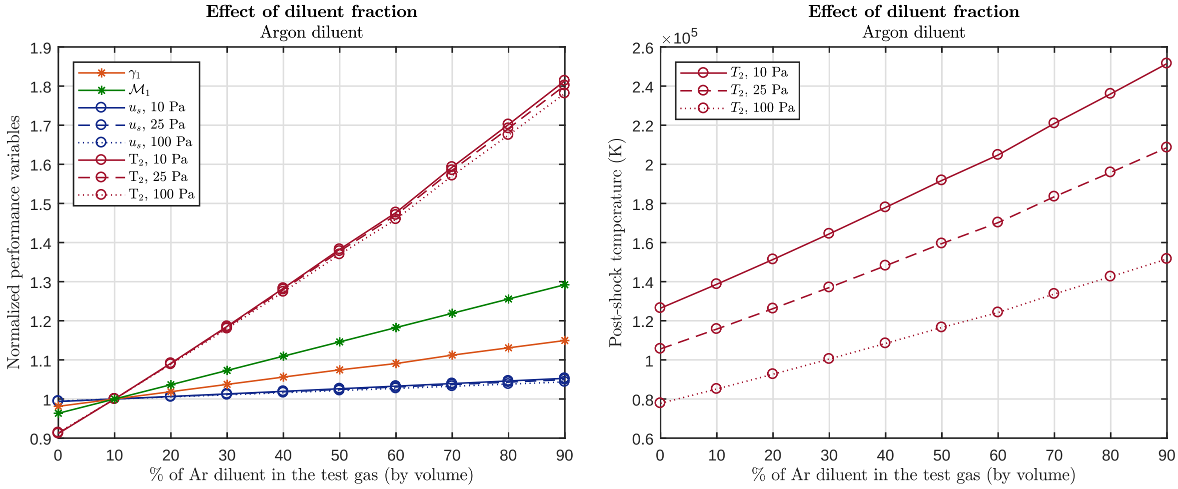

(a) Normalized performance variables.

(b) Post-shock temperature.

Figure 4.10: Effect of argon diluent.

As with the helium diluent in a H_2/He mixture, when introducing argon into air, from figure 4.10a, there is an increase of around 13.0% in the working specific heat ratio and an increase of around 22.6% in the working molecular weight, comparing with 10% Ar diluent.

The shock speed has an increase of around 5.0%, while the post-shock temperature increases around 44.9%. Once again, this shows that the main change made to the flow by adding more argon diluent is to increase the post-shock temperature, simulating a hotter entry, although there is also a slight increase in speed .

4.4 Performance discussion

In section 4.1, design parameters, such as the area ratio for both single and double diaphragm configurations, and optimal pressures for each section were analysed. For a single diaphragm configuration, the gains for consecutively higher area ratio become progressively lower and a area ratio of 6.25:1 was chosen. For this configuration, and considering the highest driver to working pressures ratio, the obtainable lossless shock speeds are 8.03 km/s, 7.93 km/s and 8.01 km/s for Earth, Mars and Titan's atmospheres, respectively. However, as discussed in section 4.2, the flow is perturbed by disturbance effects that reduce the shock speed. Accounting with wall losses, the real shock speeds are expected to be 7.98 km/s, 7.88 km/s and 7.96 km/s, for Earth, Mars and Titan's atmospheres.

As discussed in section 1.2.2, entry speeds on Earth have varied between 7.8 km/s from LEO and 12.9 km/s by Stardust capsule; both Venus missions reached around 11 km/s; Mars Pathfinder entered at 7.26 km/s; and Huygens entered Titan with a speed of 6.2 km/s. Thereafter, considering the highest driver to working pressures ratio, the obtainable speeds by ESTHER shock tube with single diaphragm configuration are not enough to simulate fast Earth reentry speeds, although these exceed LEO entry speeds. Mars and Titan entry speeds are also exceeded. As for Venus entries, which can be simulated using the same mixture as used at Mars, ESTHER in single diaphragm configuration is not capable of simulating Venusian entry speeds.

A way of increasing the shock speed, while keeping the driver to working area ratio, is through the addition of a compression tube. The maximum shock speed is achievable for an optimal driver to intermediate area ratio (figure 4.2) and for an optimal intermediate pressure (figures 4.4 and 4.5). Considering Earth's atmosphere, for a driver pressure of 600 bar, these optimizations correspond to gains of about 44.4% (comparing configurations 2 and 6 from table 4.4), 40.0% and 33.9 % (from table 4.6), respectively, for working pressures of 10 Pa, 25 Pa and 100 Pa. Hence, the expected shock speeds with losses vary between 11.43 km/s and 14.34 km/s. Thereafter, speeds similar to those encountered during the fastest Earth reentry are expected to be achieved.

In tables 4.3 and 4.4, non-optimized configurations are also considered. Analysing driver to working area ratios of 6.25 (configurations 4, 5 and 6), the worst performance of a double diaphragm configuration would be achievable for a driver to intermediate area ratio of 6.25 (configuration 4), as confirmed in figure 4.2. For this particular case, the configuration would represent a difference of 8.4% in the shock speed, when comparing with the optimal double diaphragm configuration. If the area ratio of 6.25:1 would only be in the second diaphragm (configuration 5), the shock speed would only be about 1.6% lower.

To simulate Mars and Titan's atmospheres with shock speeds lower than those obtained with a driver pressure of 600 bar and keeping the single diagram configuration, the driver pressure was decreased to 250 bar (for Mars) and to 100 bar (for Titan). Considering Mars' atmosphere, for working pressures of 10 Pa, 25 Pa and 100 Pa, the shock speeds expected are, respectively, 7.78 km/s, 7.54 km/s and

6.98 km/s. Thereafter, operating at a driver to working pressure ratio of one million (driver pressure of 250 bar and working pressure of 25 Pa) is expected to be able to simulate Mars entries. Regarding Titan's atmosphere, using a driver pressure of only 100 bar, shock speeds of 7.71 km/s, 7.41 km/s and 6.78 km/s are expected, respectively for working pressures of 10 Pa, 25 Pa and 100 Pa. Hence, the lowest driver to working pressures ratio with a single diaphragm configuration is expected to be enough to simulate Titan entry speed.

To simulate Venus entries, ESTHER in double diaphragm configuration is needed. Considering a driver pressure of 250 bar and working pressures of 10 Pa, 25 Pa and 100 Pa, shock speeds of 12.78 km/s, 11.58 km/s and 9.74 km/s are predicted to be reached. Thereafter, a driver to working pressures ratio of one million is expected to be enough to simulate Venus entry speeds.

To simulate the Gas Giants atmospheric entry using a 90% H_2 and 10% He test mixture, the highest driver to working pressures ratio is expected to create shock waves at 18.36 km/s. As the entry speed in Uranus' atmosphere is the lowest among the Gas Giants, occurring at 22.3 km/s, none of the entry speeds in the Gas Giants may be directly simulated under these conditions. Thus, a theoretical analysis was performed to investigate the possibility of reproducing hotter shock layers, while sticking to conditions capable of being simulated in the facility. Two possibilities were examined: replacing helium by neon or utilizing a higher amount of helium diluent than in the actual entries.

When adding helium diluent to the H_2/He mixture, the shock speeds increase about only 3.8%, while the post-shock temperature more than doubles, comparing the results for 90% He to those for 10% He. In the case of addition of neon to the H_2/He mixture, as a consequence of its five times higher molecular weight compared to helium, shock layer conditions with significant levels of dissociation and ionization may be reproduced at achievable speeds. Moreover, even though the shock speed decreases slightly, the post-shock temperature increases around 42%. Thereafter, despite the low shock speeds achieved when simulating Gas Giants entries, even with helium or neon diluent, the entry frozen temperature may be recreated in ground facilities.

Regarding wall losses, for all the results presented in section 4.2, a pattern was verified. When comparing the same working pressure, wall loss velocities are very similar, independently of the shock tube configuration: for 10 Pa, losses are around 50 m/s, for 25 Pa they are around 43 m/s and for 100 Pa they are around 30 m/s. The only exception observed is for Gas Giants, possibly due to their higher shock speed, where wall losses of the order of 200 m/s, 100 m/s and 57 m/s, respectively for 10, 25 and 100 Pa, are predicted. The viscosity model, based on air gases, may also be questionable in this specific case.

Regarding viscous test times, there is a large discrepancy between the results obtained by Milne and Mirels's theories. As Mirels's theory presents the more pessimistic results, these should be the ones considered prior to getting actual experimental results.

The worst estimated test times correspond to Gas Giants' atmosphere, as expected, since the test time decreases proportionally with the increase of the shock speed. As previously mentioned, adding neon diluent into the H_2/He gas decreases the shock speed. Thereafter, this addition is expected to also increase the test time.

Summarizing, the performance of the single diaphragm shock tube satisfies the requirements for slowest entry speeds. Thereafter, in single diaphragm mode, most Mars, Titan and LEO entries are expected to be simulated. For higher performance, it becomes necessary to operate in double diaphragm mode. Under this design, ESTHER should be capable of most Earth return and Venus entry mission profiles. Performing Gas Giants entry simulations requires gas substitutions techniques to simulate the post-shock flow.

4.5 Performance for different planetary atmospheres

Analysing the operation range of the ESTHER shock tube, gathering both single and double diaphragm configurations, yields the performance envelope presented in figure 4.11. This considers Earth, Mars and Venus, Titan and Gas Giants test gases for working pressures between 10 Pa and 100 Pa. The driver pressures were varied between 100 bar, 250 bar and 600 bar. For the double diaphragm configuration, the intermediate pressures were changed between the worst case and the optimized values, respectively, 1 mbar (as concluded in figure 4.5) and the optimal value in each case.

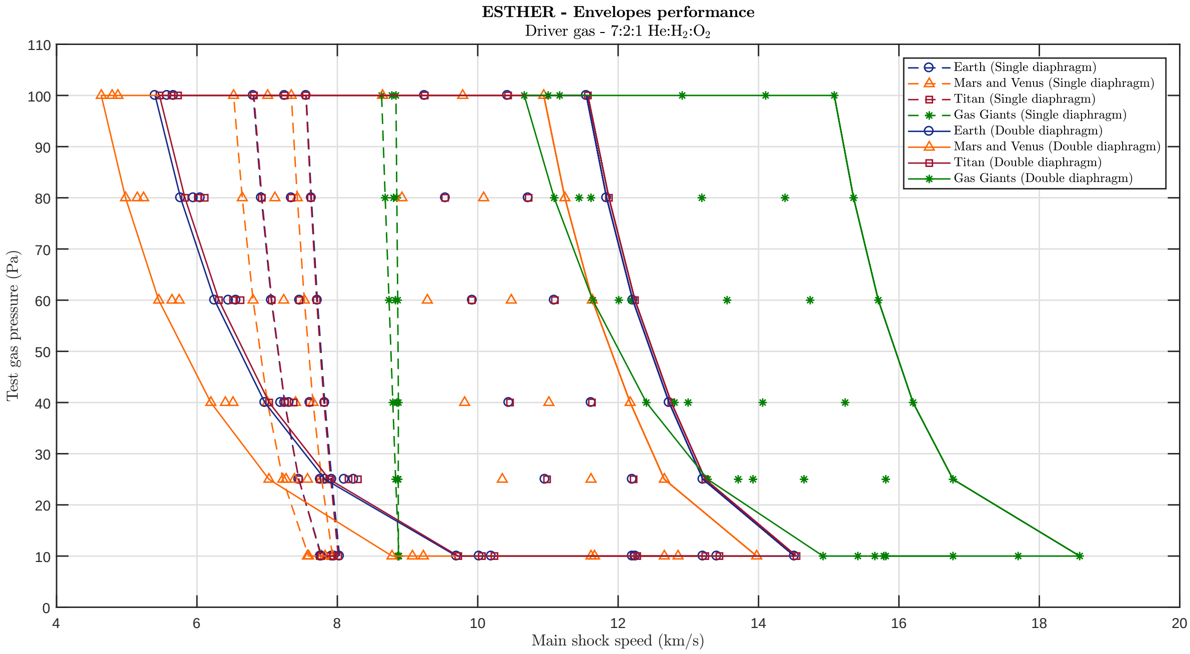

Figure 4.11: ESTHER shock tube performance envelopes for different planetary atmospheres.

Comparing the envelopes for single and double diaphragm configurations, for all speeds achievable by the single diaphragm configuration, there is a trio of working, intermediate and driver pressures for the double diaphragm configuration that can achieve that same speed. Thereafter, it does not seems necessary to change the assembly of the shock tube to achieve the speeds obtainable through the single diaphragm configuration.

Considering the driver gas composition of 7:2:1 He:H_2:O_2, the lowest shock speeds are achievable for a driver pressure of 100 bar, an intermediate pressure of 1 mbar and a working pressure of 100

Pa, corresponding to 5.37 km/s, 4.60 km/s, 5.44 km/s and 10.5 km/s, respectively for Earth, Mars and Venus, Titan and Gas Giants' atmospheres as test gases. As verified in sections 4.2.1 to 4.2.4, the highest velocities achievable are expected to be 14.44 km/s, 13.85 km/s, 14.50 km/s and 18.36 km/s, respectively for Earth, Mars and Venus, Titan and Gas Giants' atmospheres as test gas mixtures.

4.5.1 Low speed performance enhancement

A side effect of having a high performance facility is its lack of capabilities to properly perform at lower speeds. These speed ranges might still be desirable for flight testing, one good example being the atmospheric entry in Mars, where peak radiative heat fluxes (due to CO_2 IR radiation) are expected to occur at significantly lower speeds then peak convective heating, around 3 km/s [157].

Lower shock speeds may be achieved resorting to two possible techniques: 1) changing the intermediate pressure to its lowest possible value; and 2) changing the driver gas for a heavier mixture.

The first technique was considered when designing the envelope performance in figure 4.11. As the highest working pressure is 100 Pa, the lowest intermediate pressure that may be considered is 1 mbar (100 Pa), because this pressure should not be inferior to the working pressure. When considering the lowest driver to working pressures ratio and an non optimized intermediate pressure, the low driver to intermediate pressures ratio creates a weak primary shock wave, which will be then slowly accelerated in the working section, resulting in the slowest shock obtainable.

Focusing on the second technique, to try to achieve shock speeds lower than 4.60 km/s, the lowest expected using a driver mixture of 7:2:1 He:H_2:O_2, the helium in the previous mixture can be substituted by nitrogen, keeping the ratio (7:2:1 N_2:H_2:O_2). Consequently, not only the driver gas becomes heavier, but also the rotational-vibrational modes of N_2 will absorb a certain amount of heat. Hence, the shock speed is expected to be lower. This second technique has not been considered in this work due to the lack of time for constructing a thermodynamic database for the STAGG code, in the case of this specific mixture.

Chapter 5

Trigger system

The ESTHER shock tube is expected to achieve high temperatures of the post-shock gases and shock speeds up to 14 km/s in air and 18 km/s in H_2/He. Consequently, the available test time is very small before the arrival of interference waves from the contact surface and upstream sections.

Following the final installation of the shock tube, its main experimental physics diagnostic will consist on spectroscopic measurements of the radiation emitted and absorbed by the plasma in the wake of the shock wave at the test section windows, using a streak camera. Combining with the short test times available, this requires an accurate trigger system. In this chapter, the development and explanation of that trigger system and respective sensors to be used are discussed.

5.1 Background

Originally, the Institute Universitaire des Systèmes Thermiques Industriels (IUSTI), from University of Provence, was responsible for the streak camera trigger system for the ESTHER shock tube. The original design was presented by Stéphane Martinez and was composed by five piezoelectric sensors, four before and one after the camera, as shown in figure 5.1.

The system employed emitter-coupled logic (ECL), which is the fastest logic circuit family available for conventional logic-system design [159]. High speed is achieved by operating all bipolar transistors out of saturation, thus avoiding storage-time delays, and by keeping the logic signal swings relatively small, thus reducing the time required to charge and discharge the various load and parasitic capacitances.

Once the front wave reached the first sensor, the ”sample” block would compute the minimum and maximum wave pressures, the average value being then calculated. Through the rapid electronic ECL, the ”trigger” output would be generated and processed, being then sent to the streak camera. The ”control box” corresponded to a microcontroller, which would still needed to be programmed using the software environment for microchips and microcontrollers, MPLAB. Then, it would be connected to a computer with LABVIEW or EPICS [160], by optical fiber.

As previously discussed, the streak camera system was designed by Stéphane Martinez, who worked at IUSTI. However, he left the project and it became responsibility of Instituto de Plasmas e

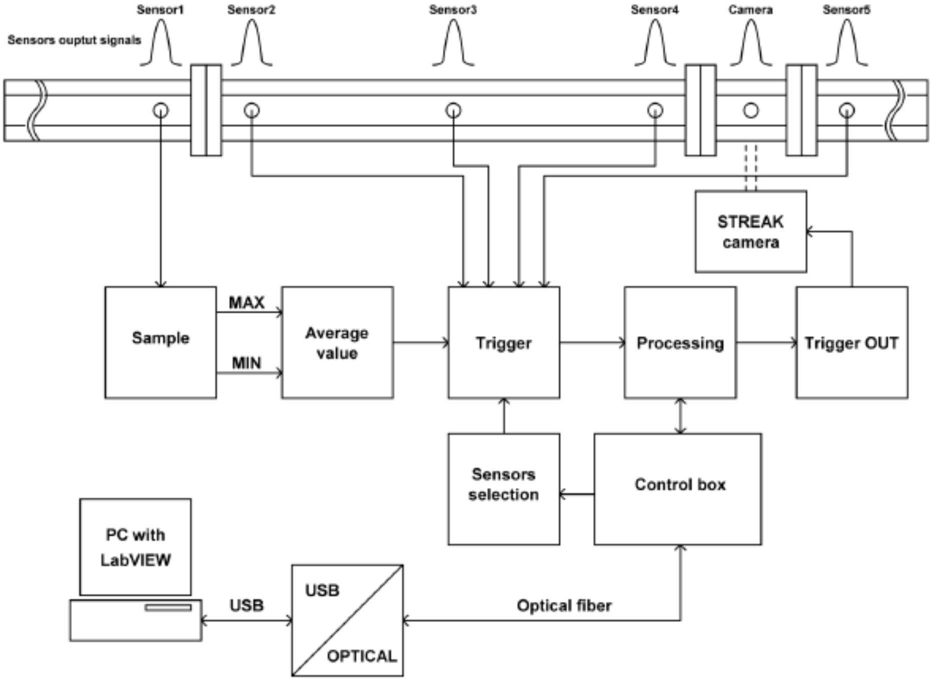

Figure 5.1: Streak camera trigger - original block diagram [158].

Fusão Nuclear (IPFN) from Instituto Superior Técnico, in Lisbon.

Despite the schematic design being already finished and some components already bought, there were disadvantages inherent to IUSTI project. The schematic was designed in PROTEUS software, which is not available at IST. Moreover, there was still no PCB layout, which could lead to two alternatives: 1) buy PROTEUS software, learn how to use it and finish the layout; 2) redraw from start using an available software and finish the layout. Additionally, as mentioned before, the microcontroller was still not programmed; the design was still not tested and the details of the original design were unknown. The final design would still have the disadvantage of not saving the waveform, since it would generate only digital signals. Therefore, it was chosen to abandon this schematic and design a new one, using FPGA based hardware and fast analogue to digital converter (ADC), commonly implemented in Fusion Plasmas, at IPFN.

5.2 IST-IPFN streak camera trigger proposal

The IST-IPFN streak camera trigger system proposes the use of only four sensors (three before and one after the camera) and the use of a FPGA rapid development board, a FMC fast ADC converter and a signal conditioning system, as shown in figure 5.2.

For this project, it was selected the KC705 evaluation board, which provides a hardware environment for developing and evaluating designs targeting the Kintex-7 FPGA [161]. FPGAs, field-programmable gate arrays, are semiconductor devices that are based around a matrix of configurable logic blocks connected via programmable interconnects [162].

The FMC-based development board, model AD-FMCJESDADC1-EBZ, is a high speed data acqui-

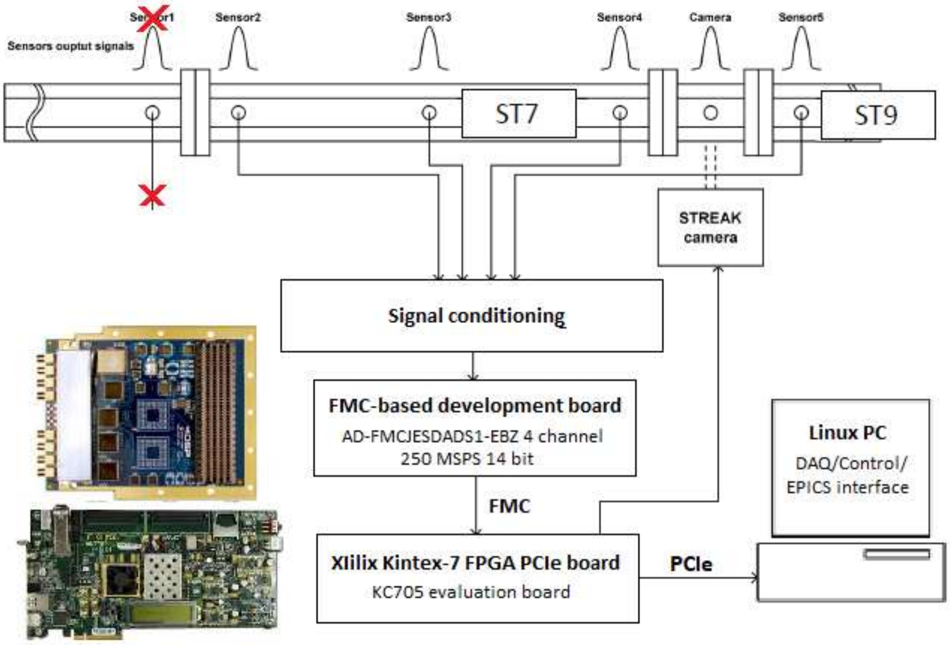

Figure 5.2: Streak camera trigger.

sition that comprises four 14-bit ADC channels with sampling speeds up to 250 MS/s, in an FMC form factor, which has two high speed JESD204B analog to digital converters (AD9250). This development board also provides two DAC channels (AD9129), an on-board clocking and power supplies to facilitate seamless connectivity with the Xilinx KC705 development platform [163, 164]. The firmware for this system was developed in Vivaldo based on a reference design project available from Analog Devices (FMC-176 [164]) .

As the FMC-176 board only has four ADC channels, the number of sensors that can be connected is limited to four, being chosen three before and one after the camera. Only two before the camera are absolutely essential to measure the delays, being the third an auxiliary to confirm the time threshold before sending it to the camera. The sensor after the camera is used to validate and correct the results, downstream of the camera. However, the sensors cannot be directly connected to the FMC development board, hence, a ”signal conditioning” system needs to be developed.

The ”signal conditioning” system can be divided into two parts, depending on two types of available sensors that is connected to: piezoelectric (PE) sensors or integrated electronics piezoelectric (IEPE) sensors. PE sensors use the piezoelectric properties of quartz to convert an applied pressure into an analogous electrical charge. The latter type is packed with a built-in charge or voltage amplifier [165].

The schematic for integrated electronic piezoelectric (IEPE) sensors is presented in figure 5.3 (and repeated in section D.1, from appendix D), where block 1 corresponds to the input of the sensors directly installed on the shock tube, using SMA type connectors. The system includes a IEPE power supply (block 2), at a constant current (between 2 mA and 20 mA [167] and a maximum voltage of 28 V, which is responsible for supplying the appropriated power required by the sensors. The signal then passes through a AC coupling capacitor (block 3), where the DC signal components are filtered out. In block 4, the signal is amplified by a factor controlled by the user, being thereafter integrated using a low noise

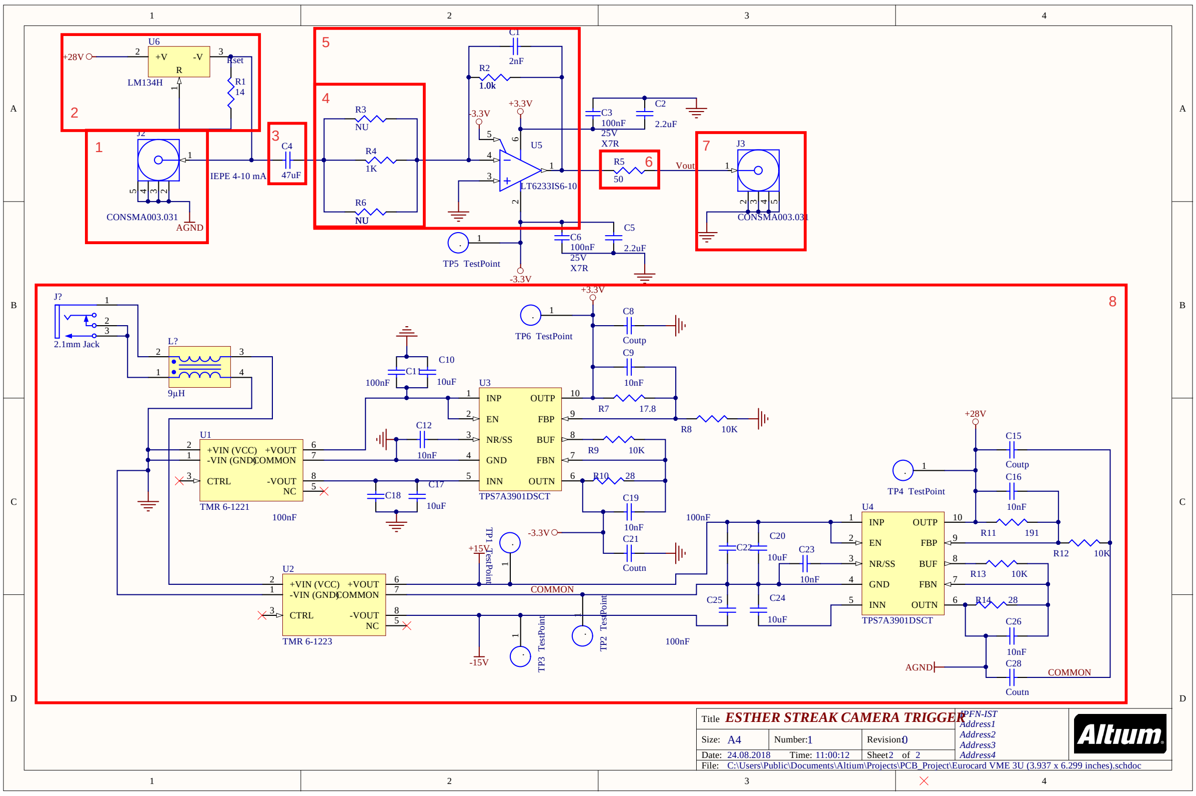

Figure 5.3: Signal conditioning system [166].

adjustable op-amp integrator with DC gain control (block 5), to avoid the saturation of the output voltage. Before reaching the output (block 7) where the signal conditioning system is connected to the FMC-176 board, using SMA connectors, the signal passes through a 50Ω resistance (block 6) for impedance matching for the ADC board. Block 8 corresponds to a high precision power supply.

The second schematic for piezoelectric (PE) sensors is still under development. Nonetheless, this type of sensors require a charge amplifier to convert the charge into pressure. As it has high impedance, it requires a high-input impedance amplifier [168], connected through a high impedance cable.

The combination of the KC705 evaluation board with the FMC-176 development board is built on a microblaze system parametrized for LINUX. A functional block diagram of the design is given in figure 5.4. The reference design contains both ADC and DAC pcores, but for this project, the DAC can be ignored.

The FPGA board, which is installed on a PCIe slot of the LINUX PC and connected by an Ethernet cable, generates the trigger signals by digital pulse processing (DPP), using VERILOG. Then, the trigger signals of the PFGA DPP are sent to the streak camera by SMA connectors.

This system is expected to precisely detect the speed of the passing wave and generate an accurate time trigger signal for the diagnostic at a clock speed of 125 MHz.

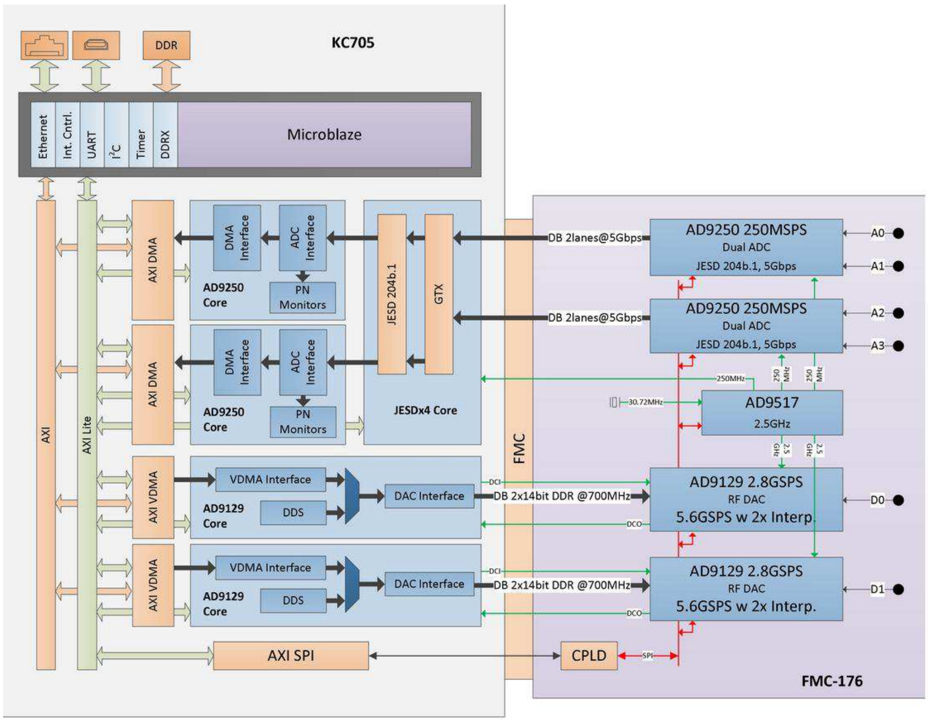

Figure 5.4: Functional block diagram, extracted from Analog Devices [164].

5.3 Trigger generation

5.3.1 Heaviside signal

To explain the FPGA algorithm, first a simplified model is analysed. For this model, there are three input signals (corresponding to the sensors before the camera) considered to be heavisides: initially at zero, increasing immediately to one once the wave intercepts the sensor. The outputs of the sensors are modelled by the response of a Butterworth second order filter, with cutoff frequency ω_n, and simulated white noise. The results are illustrated in figure 5.5.

The dash-dotted line corresponds to the threshold voltage level which is arbitrarily chosen. As the rise time of the different filtered signals can be considered equal, this level can be altered, theoretically, without influencing the time delay. Once the first signal output (orange signal) reaches that value, the system starts counting the time until the second signal output (red signal) exceeds it as well. The difference between the passage of both signals corresponds to the delay time.

As previously discussed, the sample frequency of the FMC-176 board is 250 MS/s. However, as presented in section 5.2, there are two signals samples transmitted simultaneously by the ADC converters (AD9250) and, therefore, the cycle frequency of the reference design is effectively 125 MS/s, which corresponds to a 8 ns resolution. For this example, the delay time corresponds to 30 μs, which means that there is a difference of 3750 FPGA clock cycles, between the first two signals.

For the third signal, instead of using the previous algorithm, the constant fraction zero-crossing discriminator (CFD zero-crossing) method is implemented. The advantage of this algorithm is that the delay has a lower dependency on the amplitude of the filtered signal, than with the threshold algorithm.

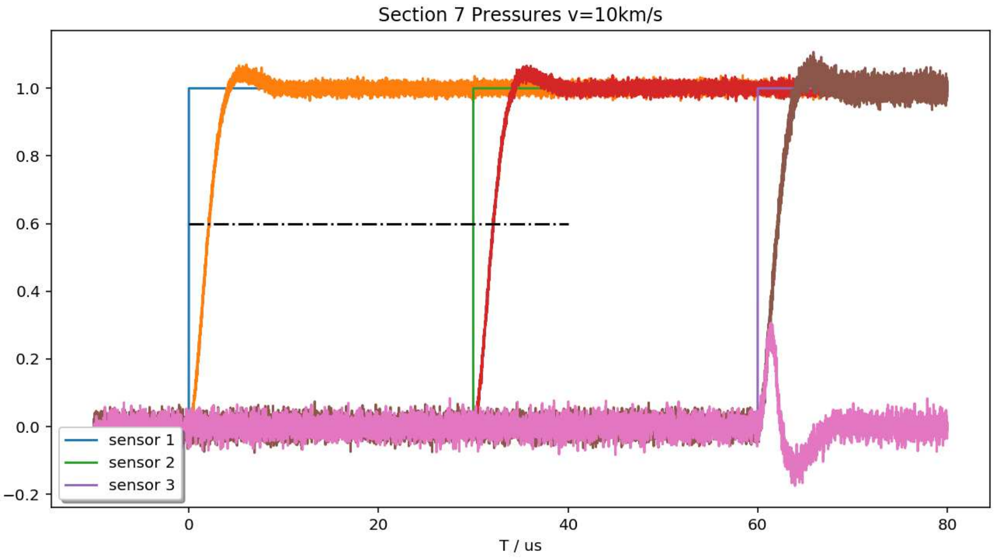

Figure 5.5: Simulation with a heaviside signal.

Alongside the third filtered signal (brown signal), a new signal (pink signal) is generated at the FPGA. The pink signal is a double differentiation of a moving average of the brown signal and its maximum pressure is dependent on a parameter F. If F equals the inverse of the cutoff frequency of the filter ($F = \text{int}(1/\omega_n)$), the pink signal reaches the same amplitude as the brown. In figure 5.5, the parameter F is lower than the inverse of the cutoff frequency and, thereafter, the maximum amplitude is also lower.

For the CFD zero-crossing method, the instant when the pink signal crosses the zero is measured and to that value, the threshold time calculated previously is summed and multiplied by two constants, one gain and an offset. These constants allow correcting the results in function of the F parameter and exact distances between the sensors. The resulting time corresponds to the instant at which the front wave will pass and, therefore, the streak camera should record the values. The forth sensor is placed after the camera to verify if the instant at which the camera recorded the values was correct. If not, it also provides data to adjust that value.

5.3.2 Real signal

In a real shock tube, the signals received by the sensors are not heavisides, as considered in the previous section. To more accurately study and predict the behaviour of the trigger system, a representative signal from the X2 expansion tube (University of Queensland) was extracted from James et al. [149]. Their results correspond to measured acceleration tube wall pressure traces by eight different transducers ('at1' to 'at8'). The locations of the wall transducers from the first diaphragm can be found in table 5.1 and the measured pressure traces are shown in figure 5.6. In the experiment, piezoelectric pressure sensors from PCB Piezotronics were used [149].

As the ESTHER shock tube will have at most three sensors before the streak camera, the aforementioned algorithms will only be implemented on the first three signals.

Table 5.1: X2 wall transducers locations, extracted from Gildfind et al. [169] and James et al. [149].

Transducer	'at1'	'at2'	'at3'	'at4'	'at5'	'at6'	'at7'	'at8'
x-location (mm)	6437	6615	6796	7590	7846	8096	8157	8197

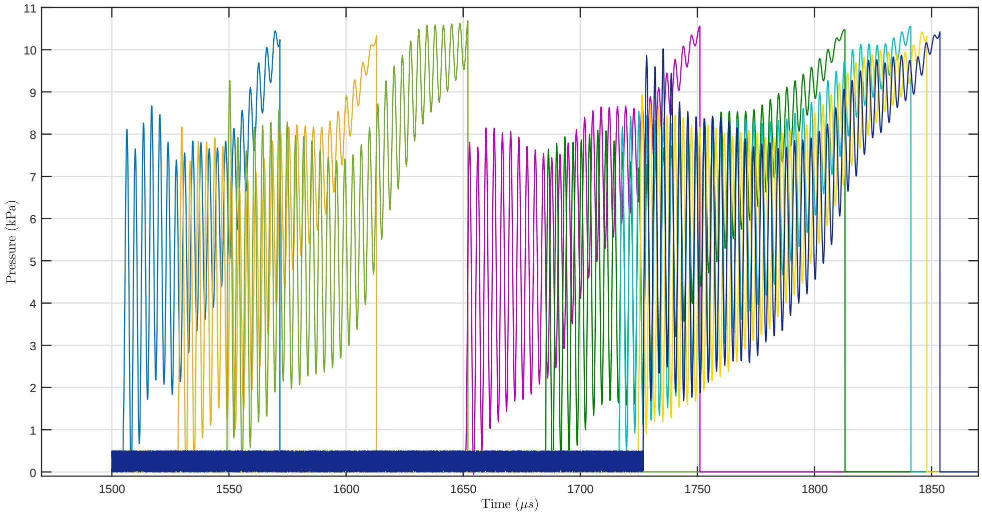

Figure 5.6: Measured acceleration tube wall pressure traces using experimentally measured shock speeds, extracted from James et al. [149].

Cutoff frequency influence

As previously discussed, the Butterworth filters have a cutoff frequency ω_n, which must be $0 < \omega_n < 1$, with 1 corresponding to the Nyquist frequency. To analyse its influence on the output signal, this parameter was altered between $\omega_n = 0.0005$, 0.001 and 0.002. Applying the low-pass filter on the first two signals, figures 5.7a, 5.7b and 5.7c are obtained.

From figures 5.7, when decreasing the cutoff frequency, there is a reduction of oscillations of the filtered signal. However, there is an increase of the rise time of the filtered signal and also an attenuation of the maximum frequency that passes the filter, which alters the value of the maximum post-shock wave pressure, by almost 12% (when comparing the extreme cases analysed).

Nevertheless, for the trigger system to measure the threshold time, the relevant information is the time difference between two point at the same level, hence the same pressure, from the first two consecutive sensors. Therefore, the cutoff frequency must be chosen such that the signal oscillations due to noise do not intersect the threshold level more than once. Analysing this particular example, those oscillations are clearly visible for higher cutoff frequencies.

For the third signal (figure 5.8), the cutoff frequency influences slightly the maximum post-shock wave pressure (only 3%). However, the signal resulting from the CFD zero-crossing (red signal) is significantly altered.

For low cutoff frequencies, the differentiated signal is critically attenuated and the zero-crossing can even not occur for the shock front wave signal (as seen in the zoom of the signal for $\omega_n = 0.0005$, in the smallest view from figure 5.8a). When increasing the cutoff frequency, the intersection with zero occurs

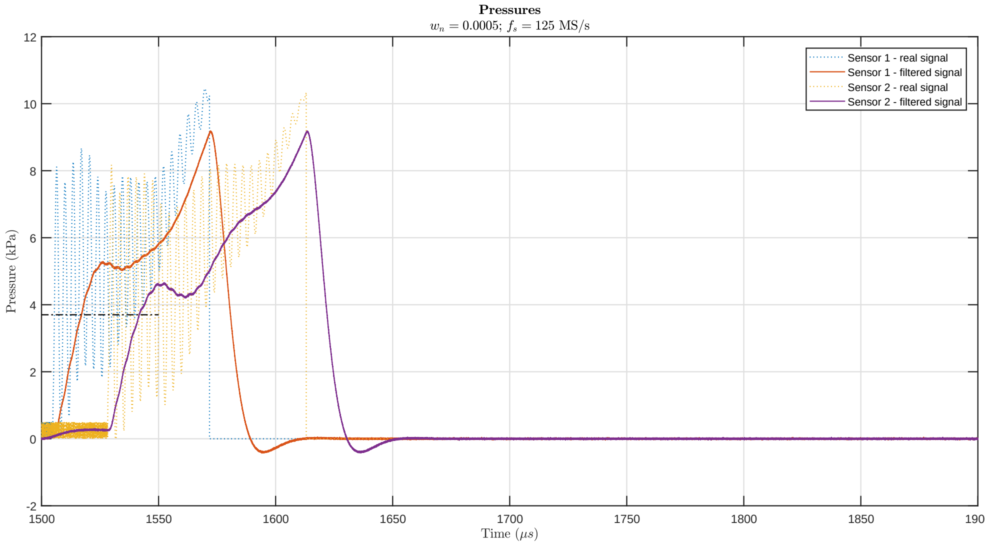

(a) $\omega_n = 0.0005$

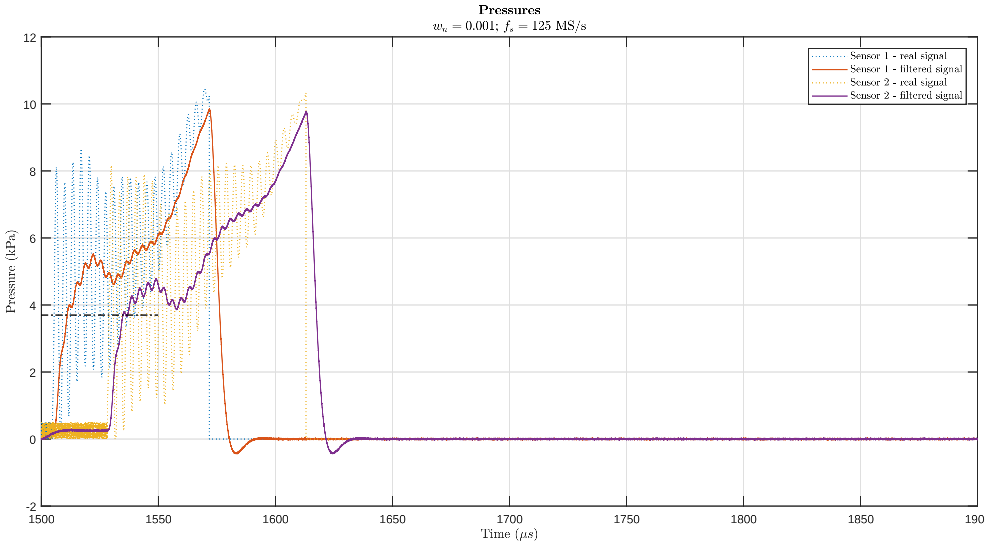

(b) $\omega_n = 0.001$

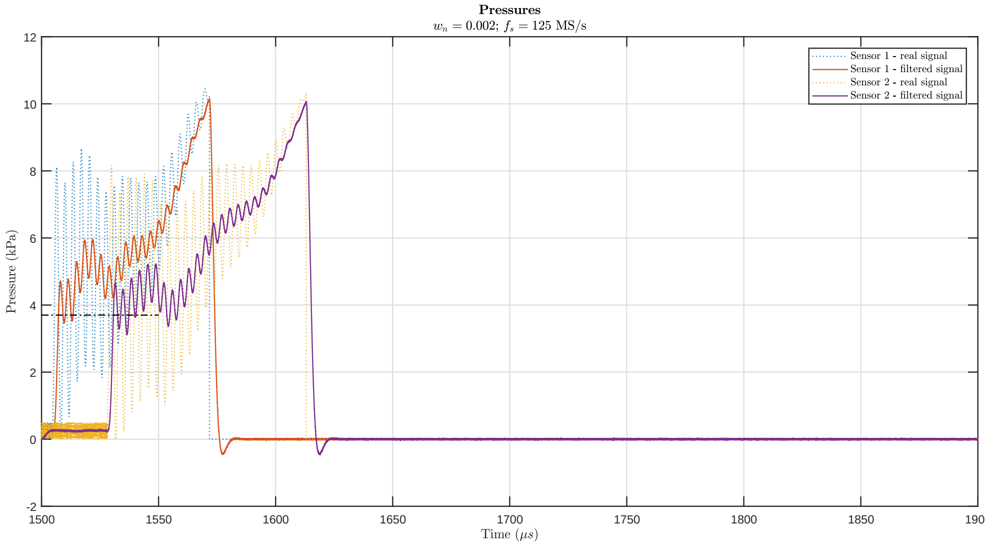

(c) $\omega_n = 0.002$

Figure 5.7: Influence of cutoff frequency on the filtered signal pressure from the first and second sensors.

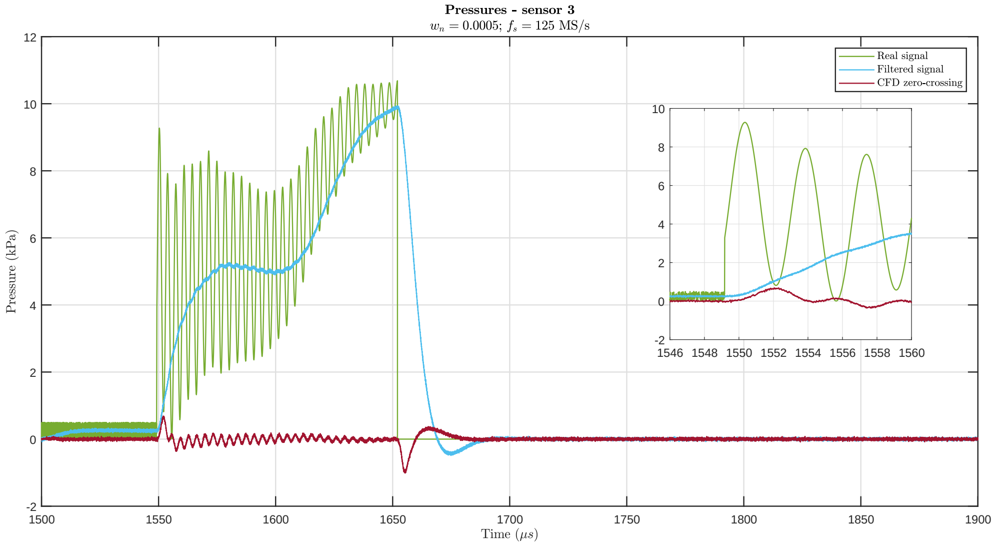

(a) $\omega_n = 0.0005$

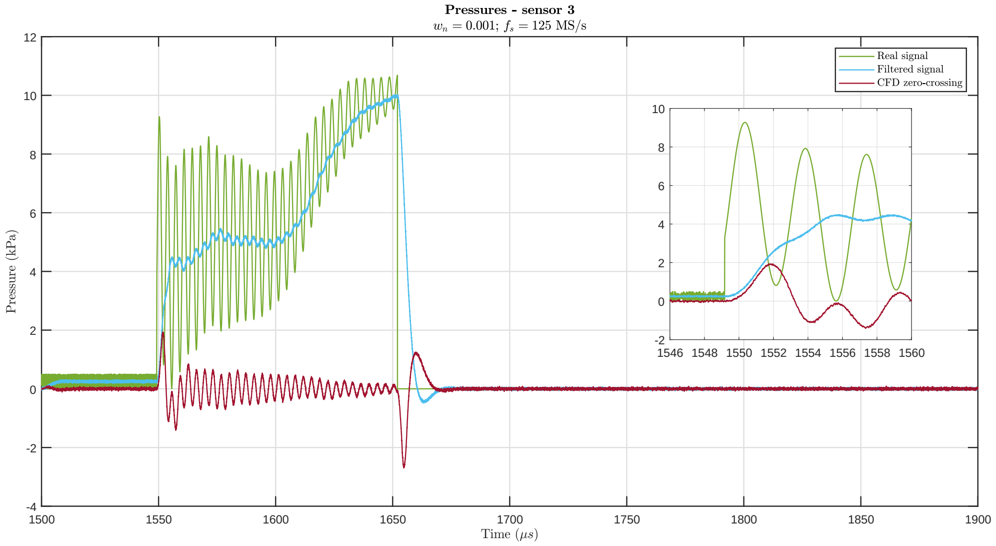

(b) $\omega_n = 0.001$

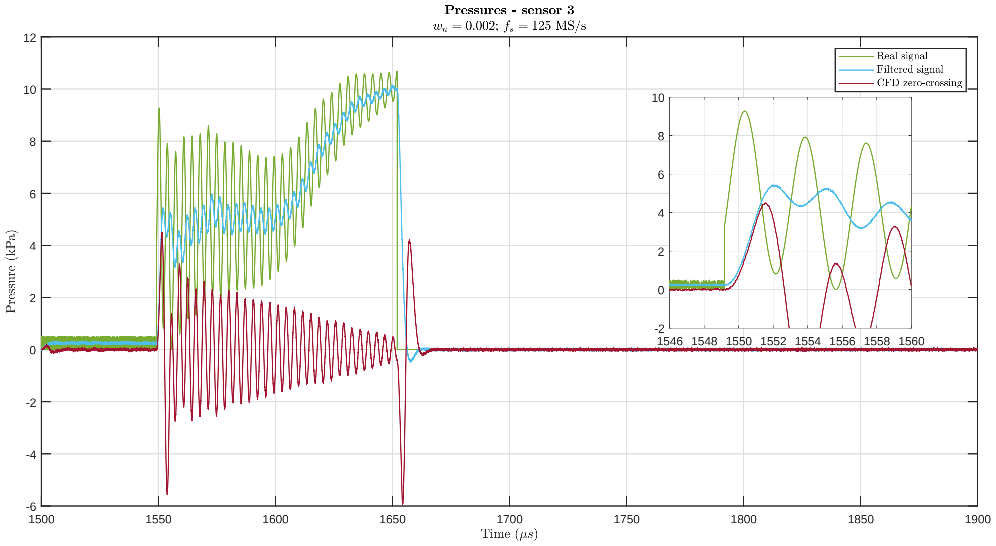

(c) $\omega_n = 0.002$

Figure 5.8: Influence of cutoff frequency on the filtered signal pressure from the third sensor and on the CFD zero-crossing method.

earlier than for an inferior frequency. This intersection instant is then corrected by the constants, for the calculation of the final instant sent to the streak camera.

5.3.3 Sensors positioning

The ESTHER working section is constituted by nine different parts ('ST1' to 'ST9'), being 'ST8' the section where the observation window will be. The assembly of the parts until the camera will remain unchanged, being attached by the following order: 'ST1'-'ST2'-'ST3'-'ST4'-'ST7'-'ST8'. However, after the camera, there are three possible configurations: 1) 'ST8bis'-'ST5'-'ST6'-ST9'; 2) 'ST5'-'ST8bis'-'ST6'-'ST9'; and 3) 'ST6'-'ST8bis'-'ST5'-'ST9'. The working section is expected to have three sensors in the section before and one in the section after the observation window.

The locations of the sensors before the camera, measured from the second diaphragm and according to the latest CAD designs from March 2018, are presented in table 5.2a. The streak camera will be installed 4297 mm from the second diaphragm. The possible locations of the forth sensor dependent on the configuration are presented is table 5.2b. These distances are essential when simulating the algorithms with expected waveforms for ESTHER.

Table 5.2: ESTHER pressure sensors location.

(a) Sensors before the camera.

Sensor	1	2	3
x-location (mm)	3399	3699	3999

(b) Sensor after the camera.

Configuration	1	2	3
x-location (mm)	4577	4578	4536.5

5.4 Timing system

There are several options for measuring the shock speed and, hence, triggering the optical instrumentation at the working section. As previously discussed, for this project, two options for gauges may be considered: piezoelectric (PE) sensors and integrated electronics piezoelectric (IEPE) sensors. The PE and IEPE gauges considered to this project and their properties are summarized in tables 5.3a and 5.3b, respectively.

The pressure rise across the shock is very fast requiring only a few collisions for pressure and translational temperature rise. To directly measure the pressure output, the timing gauges require a suitable high natural frequency.

For the working section before the camera, three IEPE sensors Kistler 603CBA000014.0 seem to be the most appropriate since they have a very high natural frequency and a small rise time. Moreover, IEPE sensors have the advantage of providing low impedance voltage output from a constant current supply and of needing a less expensive conditioning circuitry and cabling. After the camera, PE sensors may be used. Nevertheless, these solutions are still under evaluation and can be changed until their installation.

Table 5.3: Sensors characteristics.

(a) PE sensors, respectively from data sheets [170–175].

Gauge	Sensitivity (pC/bar)	Natural frequency (kHz)	Pressure range (bar)	Overload pressure (bar)	Rise time (μs)
Kistler 601CAA	-37	> 215	$0 - 250$	300	< 1.4
Kistler 603B	-5	400	$0 - 200$	350	1
Kistler 603CAA	-5	> 500	$0 - 1000$	1100	< 0.4
Kistler 701A	-80	70	$0 - 250$	400	6
Kistler 7001	-80	70	$0 - 250$	350	6

(b) IEPE sensors, respectively from data sheets [170, 172, 175].

Gauge	Sensitivity (mV/bar)	Natural frequency (kHz)	Pressure range (bar)	Overload pressure (bar)	Rise time (μs)
Kistler 601CBA000014.0	357	> 215	$0 - 250$	300	< 1.4
Kistler 603CBA000014.0	357	> 500	$0 - 1000$	1100	< 0.4
PCB 113 B21	360	> 500	$0 - 14$	70	< 1
PCB 113 A31	2000	> 1000	$0 - 3.4$	56	< 3.0, < 0.5 (reflected)

As well as the shock tube timing, measurements in the compression tube are also needed as a diagnostic. Since there is no working section in this tube, the only measurements needed are the shock speed and post-shock pressure, as a diagnostic. Hence, for the diagnostic, only two PE (charge coupled) gauges seem appropriate, since this type of sensors detects both the final level and the transitory signal.

Chapter 6

Conclusions

This chapter discusses the final conclusions for this thesis, its major achievements and recommended future work.

6.1 Conclusions

The primary objective of this thesis was to estimate the performance design for the new European shock tube, ESTHER. For different planetary atmospheres, the lossless shock speeds have been simulated, using the STAGG code. The wall drag losses were computed applying Milne's algorithm and the test times were predicted based on Mirels' work. As the ESTHER shock tube is expected to have a very small test time, an accurate trigger system was discussed and devised.

The initial theoretical predictions have shown that the best performance is achieved for optimal area ratio and intermediate pressure. This is, in fact, the major advantage of ESTHER shock tube: the cross-area reduction at the diaphragm is equivalent to an increase of the driver gas temperature, which accelerates the gas; and the intermediate section allows the main shock wave to be produced from a primary shock wave, reaching higher velocities. When comparing the best and the worst performance cases, the overall gains amount to between 60% and 70%.

Simulations for Earth, Mars, Titan and Gas Giants' were performed and analysed. With the exception for Gas Giants, the respective atmospheric entry velocities are expected to be reached, using a double diaphragm configuration. The influence of adding argon diluent into an air mixture, as a way of boosting speeds and post-shock temperatures, was analysed. This change has shown that the main change made to the flow is the increase of the post-shock temperature, simulating hotter entries, with only a slight increase in speed.

As previously discussed, the wall drag loss effects were also analysed. The estimates predict wall losses to be only dependent on working pressure, around 50 m/s, 43 m/s and 30 m/s, respectively, for working pressures of 10 Pa, 25 Pa and 100 Pa. The only observed exception was for Gas Giants, possibly due to their higher shock speeds, where wall losses were of the order of 200 m/s, 100 m/s and 57 m/s, respectively for 10 Pa, 25 Pa and 100 Pa. Since this is only a theoretical model, it may be questionable in this latter case and must therefore be validated.

The estimates for the test times through Mirels' theory are also questionable as his theory was deducted for weak shock speeds in air mixtures. Nevertheless, considering these results as pessimistic, the test times may vary between 3.5 μs and 21.7 μs, for single diaphragm configuration, and between 1.3 μs and 30.7 μs, for double diaphragm configuration.

Tasissa et al.'s theory was applied to the ESTHER single diaphragm configuration and comparing to the $x-t$ wave diagrams obtained independently, it was verified that the formation of the blast wave occurs after the observation window. For ESTHER in double diaphragm configuration, the algorithm was applied considering the properties of the intermediate section and it was also verified that the intersection of the head of the expansion wave with the primary shock wave occurs much after the main shock wave reaches the observation window. Hence, it may be possible to reduce the combustion chamber length, after a few test campaigns successfully done in the nominal configuration.

As the Gas Giants entry speeds are not expected to be achieved, the possibility for creating hotter shock layer conditions at slower speeds was analyzed. When changing the percentage of helium diluent in the H_2/He mixture and considering ideal gas, it was verified that the shock speeds increased only slightly while the post-shock temperature more than doubled. When using high percentages of helium, frozen temperatures may be recreated. When replacing the helium by neon, even though the shock speeds decreased, the post-shock temperature increased significantly. In fact, percentages of neon between 4% and 21% may be enough to simulate the planetary entry frozen temperature.

Even though ESTHER in single diaphragm configuration is able to simulate LEO and most of Mars and Titan entry speeds, based on the envelope performance, it was verified that for all the achievable shock speeds, there is a combination of driver, intermediate and working pressures that can achieve the same speed using ESTHER in double diaphragm configuration.

As already discussed, the expected test times are very small, hence a very accurate trigger system is necessary. The FPGA algorithm developed by IST-IPFN was implemented for a simplified model and then on a representative signal. The influence of the cutoff frequency on the latter was analysed and it was verified that, when decreasing the cutoff frequency, there is a reduction of oscillations of the filtered signal. However, the rise time increases and there is an attenuation of the maximum frequency, which alters the value of the maximum post-shock wave pressure. When implementing the CFD zero-crossing method, it was verified that the cutoff frequency influences slightly the maximum post-shock pressure, while the differentiated signal is critically attenuated for low cutoff frequencies.

The different sensors available were studied and it was concluded that three IEPE sensors may be used for the working section, before the camera, and one PE sensor may be implemented after the camera. For the compression tube measurements, two PE sensors may be used.

6.2 Achievements

The main objective of this work was to estimate the performance of the ESTHER shock tube. Simulations for different planetary atmospheres, on single and double stage configurations, were carried and the results were corroborated with the initial performance estimations (for air as an ideal gas). Considering equilibrium gases, the results were satisfactory, estimating velocities capable of reproducing the entry conditions in Earth, Mars and Titan's atmospheres. The maximum expected shock speeds in air are 8.0 km/s and 14.4 km/s, respectively for single and double diaphragm configurations. Hence the speed requirement of 12 km/s is expected to be exceeded.

Gas Giants simulations were also carried out using a pessimistic equilibrium gas model and a maximum shock speed of 18.4 km/s was predicted. As this speed is not enough to simulate Gas Giants entries, gas substitutions were analysed and it was concluded that both neon and helium may simulate the frozen entry temperatures.

As ESTHER is a facility tailored for high-speed performance, it was verified that low speeds are difficult to reach, and it is hence necessary to study the performance of a heavier driver mixture.

The blast wave initiation lengths were confirmed using the characteristics code implemented, which open the possibility of decreasing the nominal volume of the combustion chamber.

The FPGA algorithm implemented into a signal behaved as initially expected and the critical aspects to decide the cutoff frequency of the filter were discussed.

6.3 Recommendations for future work

In terms of estimations of the ESTHER shock tube performance much work remains to be done. The follow-up work is recommended:

- Introducing wall losses algorithms in STAGG, to estimate the real shock speeds;
- Changing the driver pressure gas to a heavier mixture, to reproduce lower speeds;
- Updating STAGG to simulate the intermediate gas in equilibrium conditions;
- Modifying the intermediate gas for hydrogen, to try to verify if faster shock speeds may be achieved;
- Simulating the argon, helium and neon gas substitutions using equilibrium gas files.

After ESTHER is commissioned and based on its experimental results, the following work is proposed to improve the theoretical models:

- Performing semi-empirical correlations for high speed velocities, updating Mirels' theory;
- Validating Milne's wall drag effect theory for the different test gas mixtures;
- Verifying if the blast wave formation does not influence the shock wave;
- Studying the effect of secondary diaphragm rupture on the driver performance and optimizing the diaphragm opening model on $x-t$ diaphragms.

For the trigger system:

- Finishing the schematic for piezoelectric sensors and assembling the boards;
- Verifying if the proposed algorithm properly works for real ESTHER pressure signals;
- Studying the influence of the attenuation of the post-shock signal comparing the experimental results with the numerical predictions;
- Verifying if the rise time of the signal is inferior to the test time available, specially for high shock speeds.

Bibliography

[1] S. F. de Córdoba. 100km altitude boundary for astronautics. `https://www.fai.org/page/icare-boundary`, accessed August 25, 2018.

[2] European Space Agency. `http://www.esa.int/Our_Activities/Space_Science/Rosetta_overview`, accessed September 13, 2018.

[3] NASA Jet Propulsion Laboratory. `https://voyager.jpl.nasa.gov/mission/`, accessed September 4, 2018.

[4] R. J. Stalker. Hypervelocity aerodynamics with chemical equilibrium. *Annual Review of Fluid Mechanics*, 21, 1989. `https://doi.org/10.1146/annurev.fl.21.010189.000345`.

[5] P. A. Gnoffo, C. O. Johnston, and B. Kleb. Challenges to computational aerothermodynamic simulation and validation for planetary entry vehicle analysis. Technical report.

[6] National Research Council. *Vision and Voyages for Planetary Science in the Decade 2013-2022*, chapter 7 - The Giant Planets: Local Laboratories and Ground Truth for Planets Beyond. The National Academies Press, 2011.

[7] National Research Council. *New Frontiers in the Solar System: An Integrated Exploration Strategy*, chapter 4 - Giant Planets: Keys to Solar System Formation. The National Academies Press, 2003. `https://doi.org/10.17226/10432`.

[8] P. A. Gnoffo. Planetary-entry gas dynamics. *Annual Review of Fluid Mechanics*, 31(1):459–494. `https://doi.org/10.1146/annurev.fluid.31.1.459`.

[9] A. Seiff, E. Venkatapathy, B. L. Haas, and P. Intrieri. Galileo probe aerodynamics. In *14th AIAA Applied Aerodynamics Conference*, number AIAA-96-2451, June 1996. `https://doi.org/10.2514/6.1996-2451`.

[10] NASA Official: Kristen Erickson. `https://solarsystem.nasa.gov/planets/mercury/in-depth/`, accessed August 25, 2018.

[11] F. W. Taylor. Planetary atmospheres. *Meteorological Applications*, 17(4):393–403, 2010. `https://doi.org/10.1002/met.212`.

[12] Rauf KM, Majeed D, and Ibrahim R. Comparing the atmospheric compositions of all planets and giant moons in solar system. *Journal of Astrobiology & Outreach*, 3(136), 2015. `https://doi.org/10.4172/2332-2519.1000136`.

[13] S. J. Billet and A. J. Smith. STAGG user manual. Confidential and property product of Fluid Gravity Engineering Ltd., April 2013.

[14] NASA Official: David R. Williams. NASA planetary fact sheets, . `https://nssdc.gsfc.nasa.gov/planetary/factsheet/index.html`, accessed August 25, 2018.

[15] T. R. Spilker, C. S. Borden, M. Adler, M. M. Munk, R. W. Powell, R. D. Braun, P. M. Beauchamp, J. A. Cutts, P. F. Wercinski, and the A-Team. An assessment of aerocapture and application to future missions. Technical report, NASA, February 2016.

[16] G. Herdrich, S. Löhle, and M. Fertig. Experimental simulation of high enthalpy planetary entries. *The Open Plasma Physics Journal*, pages 150–164, 2009. `https://doi.org/10.2174/1876534300902010150`.

[17] P. N. Desai, D. T. Lyons, J. Tooley, and J. Kangas. Entry, descent, and landing operations analysis for the Stardust entry capsule. *Journal of Spacecraft and Rockets*, 45(6):1262–1268, November-December 2008. `https://doi.org/10.2514/1.37090`.

[18] A. M. Brandis. *Experimental Study and Modelling of Non-equilibrium Radiation During Titan and Martian Entry*. PhD thesis, The University of Queensland, 2009.

[19] T. S. Balint. Overview of mission architecture options for jupiter deep entry probes. In *Outer Planets Advisory Group Meeting*, June 2005.

[20] R. Beebe and L. Dudzinski. Saturn atmospheric entry probe trade study. Mission concept study, NASA, September 2010.

[21] W. B. Hubbard. *Vision and Voyages for Planetary Science in the Decade 2013-2022*, chapter Ice Giants Decadal Study. National Academy Press, Washington, 2010.

[22] B. R. Hollis and S. Borrelli. Aerothermodynamics of blunt body entry vehicles. Chapter 3. Technical report, NASA Langley Research Center, November 2011.

[23] Federal Aviation Administration. Chapter 4.1.7 - Returning from space. Available online: `https://www.faa.gov/about/office_org/headquarters_offices/avs/offices/aam/cami/library/online_libraries/aerospace_medicine/tutorial/media/III.4.1.7_Returning_from_Space.pdf`.

[24] F. Mazoue and L. Marraffa. Determination of the radiation emission during the FIRE II entry. In *The 2nd International Workshop on Radiation of High Temperature Gases in Atmospheric Entry*, number SP-629. University 'La Sapienza', November 2006.

[25] L. C. Hartung, R. A. Mitcheltree, and P. A. Gnoffo. Survey of high-enthalpy shock facilities in the perspective of radiation and chemical kinetics investigations. *Journal of Thermophysics and Heat Transfer*, 6(3), July-September 1992.

[26] M. Wright, M. Loomis, and P. Papadopoulos. Aerothermal analysis of the project Fire II afterbody flow. *Journal of Thermophysics and Heat Transfer*, 17(2), April-June 2003. `https://doi.org/10.2514/2.6757`.

[27] D. Liechty, C. Johnston, and M. Lewis. Comparison of DSMC and CFD Solutions of Fire II including radiative heating. In *42nd AIAA Thermophysics Conference*, 2011. `https://doi.org/10.2514/6.2011-3494`.

[28] E. R. Hillje and R. Savage. Status of aerodynamic characteristics of the Apollo entry configuration. In *AIAA Entry Vehicle Systems and Technology Meeting*, number 68-1143, December 1968. `https://doi.org/10.2514/6.1968-1143`.

[29] M. Wright, D. K. Prabhu, and E. R. Martinez. Analysis of Apollo Command Module afterbody heating part i: AS-202. *Journal of Thermophysics and Heat Transfer*, 20(1), January-March 2006. `https://doi.org/10.2514/1.15873`.

[30] M. J. Wright, J. L. Brown, K. Sinha, G. V. Candler, F. S. Milos, and D. K. Prabhu. Validation of afterbody aeroheating predictions for planetary probes: Status and future work. In *2nd International Planetary Probe Workshop*, number NASA/CP-2004-213456. NASA Ames Research Center, April 2005.

[31] R. C. Ried Jr., W. C. Rochelle, and J. D. Milhoan. Radiative heating to the Apollo Command Module: Engineering prediction and flight measurement. Technical report, NASA Manned Spacecraft Center, April 1972.

[32] E. R. Hillje. Entry aerodynamics at lunar return conditions obtained from the flight of Apollo 4 (AS-501). Technical Report NASA TN D-5399, NASA Manned Spacecraft Center, October 1969.

[33] NASA Official: David R. Williams, . `https://nssdc.gsfc.nasa.gov/nmc/spacecraftDisplay.do?id=1970-060A`, accessed September 14, 2018.

[34] D. Leverington. *New Cosmic Horizons: Space Astronomy from the V2 to the Hubble Space Telescope*. Cambridge University Press, 2000. ISBN: 9780521658331.

[35] NASA Official: Jim Wilson. `https://www.nasa.gov/mission_pages/pioneer-venus/`, accessed July 29, 2018.

[36] NASA Goddard Space Flight Center: David R. Williams. `https://nssdc.gsfc.nasa.gov/planetary/pioneer_venus.html`, accessed July 29, 2018.

[37] L. J. Nolte and S. Sommer. Probing a planetary atmosphere: Pioneer Venus spacecraft description. In *AIAA/AGU Conference on the Exploration of the Outer Planets*, number 75-1160, September 1975. `https://doi.org/10.2514/6.1975-1160`.

[38] NASA Official: David R. Williams, . `https://nssdc.gsfc.nasa.gov/nmc/spacecraftDisplay.do?id=1978-078D`, accessed July 29, 2018.

[39] C. Davies and M. Arcadi. Planetary mission entry vehicles quick reference guide. Version 3.0. Technical Report NASA/SP-2006-3401, NASA Ames Research Center, January 2006.

[40] B. J. Bienstock. Pioneer venus and galileo entry probe heritage. In A. Wilson, editor, *International Workshop Planetary Probe Atmospheric Entry and Descent Trajectory Analysis and Science*, number ESA SP-544, pages 37–45. ESA Publications Division, 2004. ISBN: 92-9092-855-7.

[41] NASA Goddard Space Flight Center: David R. Williams. `https://nssdc.gsfc.nasa.gov/nmc/spacecraftDisplay.do?id=1978-078E`, accessed July 29, 2018.

[42] J. J. Givens, L. J. Nolte, and L. R. Pochettino. Galileo atmospheric entry probe system: Design, development, and test. In *AIAA 21st Aerospace Sciences Meeting*, number AIAA-83-0098. NASA Ames Research Center, January 1983.

[43] NASA Jet Propulsion Laboratory. `https://www.jpl.nasa.gov/missions/galileo/`, accessed July 30, 2018.

[44] NASA Goddard Space Flight Center: David R. Williams. `https://nssdc.gsfc.nasa.gov/nmc/spacecraftDisplay.do?id=1989-084E`, accessed July 30, 2018.

[45] NASA: Mars Exploration. `https://mars.nasa.gov/programmissions/missions/past/pathfinder/`, accessed August 10, 2018.

[46] D. A. Spencer and R. D. Braun. Mars Pathfinder atmospheric entry: Trajectory design and dispersion analysis. *Journal of Spacecraft and Rockets*, 33(5), September-October 1996. `https://doi.org/10.2514/3.26819`.

[47] D. A. Spencer, R. C. Blanchard, R. D. Braun, P. H. Kallemeyn, and S. W. Thurman. Mars Pathfinder entry, descent, and landing reconstruction. *Journal of Spacecraft and Rockets*, 36(3), May-June 1999. `https://doi.org/10.2514/2.3478`.

[48] Cassini Science Communications Team. `https://saturn.jpl.nasa.gov/mission/spacecraft/huygens-probe/`, accessed August 10, 2018.

[49] G. Colombatti, A. Aboudan, F. Ferri, and F. Angrilli. Huygens probe entry dynamic model and accelerometer data analysis. *Planetary and Space Science*, 56:601–612, 2008. `https://doi.org/10.1016/j.pss.2007.11.018`.

[50] M. J. Wright, B. R. Hollis, D. Rose, and L. Walpnot. Post-flight aerothermal analysis of Huygens probe. In *3rd International Planetary Probe Workshop*. National Center for Scientific Research 'Demokritos', June-July 2005.

[51] W. H. Willcockson. Stardust sample return capsule design experience. *Journal of Spacecraft and Rockets*, 36(3), May-June 1999.

[52] M. W. Lo, B. Williams, W. E. Bollman, D. Han, Y. Hahn, J. L. Bell, E. A. Hirst, R. A. Corwin, P. E. Hong, K. C. Howell, B. Barden, and R. Wilson. Genesis mission design. In *AIAA/AAS Astrodynamics Specialist Conference*, number AIAA-98-4468, August 1998. `https://doi.org/10.2514/6.1998-4468`.

[53] J. H. Grinstead, P. Jenniskens, A. M. Cassell, J. Albers, and M. W. Winter. Airborne observation of the Hayabusa Sample Return capsule re-entry. In *42nd AIAA Thermophysics Conference*, number ARC-E-DAA-TN3704, June 2011.

[54] A. M. Cassell, M. W. Winter, G. A. Allen, Jr, J. H. Grinstead, M. E. Antimisiaris, J. Albers, and P. Jenniskens. Hayabusa re-entry: Trajectory analysis and observation mission design. In *42nd AIAA Thermophysics Conference*, number ARC-E-DAA-TN3813, June 2011.

[55] P. Vieille. Sur les discontinuites produites par la de'tente brusque de gas comprimes. *Comptes Rendus de l'Academie des Sciences de Paris*, 129:1228–1230, 1899.

[56] R. Brun. Shock tubes and shock tunnels: Design and experiments. Technical report, Université dAix-Marseille, September 2009.

[57] H. Mirels. Test time in low-pressure shock tubes. *The Physics of Fluids*, 6(9):1201–1214, September 1963. `https://doi.org/10.1063/1.1706887`.

[58] H. Mirels. Laminar boundary layer behind a strong shock moving into air. Technical Note D-291, NASA Washington, February 1961.

[59] R. G. Morgan. A review of the use of expansion tubes for creating superorbital flows. In *AIAA, Aerospace Sciences Meeting & Exhibit, 35th*, January 1997. `http://doi.org/10.2514/6.1997-279`.

[60] E. L. Resler and D. E. Blossom. Very high mach number flows by unsteady flow principles. *Cornell Graduate School of Aerodynamic Engineering*, 1952. `https://doi.org/10.2514/6.1992-3943`.

[61] C. I. Morris. *Shock-induced combustion in high-speed wedge flows*. PhD thesis, Stanford University, December 2001.

[62] A. Dufrene. High enthalpy studies of capsule heating in an expansion tunnel facility. Technical report, CUBRC, 2012.

[63] R. Morgan. Free-piston driven expansion tubes. *Handbook of Shock Waves*, 1:603–622, 2001. `https://doi.org/10.1016/B978-012086430-0/50014-2`.

[64] P. Reynier. Survey of high-enthalpy shock facilities in the perspective of radiation and chemical kinetics investigations. *Progress in Aerospace Sciences*, 85, 2016.

[65] J. H. Grinstead, M. C. Wilder, D. C. Reda, C. J. Cornelison, B. A. Cruden, and D. W. Bogdanoff. Shock tube and ballistic range facilities at NASA Ames Research Center. Technical report, NASA, 2010.

[66] D. W. Bogdanoff. Shock tube experiments for Earth and Mars entry conditions. Technical report, NASA, September 2009.

[67] R. Martinez, . `https://www.nasa.gov/ames/thermophysics-facilities/electric-arc-shock-tube`, accessed September 6, 2018.

[68] C. James, D. E. Gildfind, R. G. Morgan, P. A. Jacobs, and F. Zander. Designing and simulating high enthalpy expansion tube conditions. Technical report, The University of Queensland, 2013.

[69] P. Jacobs, R. Morgan, A. Brandis, David, Buttsworth, A. Dann, M. D'Souza, T. E. D. Gildfind, R. Gollan, C. Jacobs, M. McGilvray, T. McIntyre, N. Mudford, H. Porat, D. Potter, and F. Zander. Design, operation and testing in expansion tube facilities for super-orbital re-entry. Technical report, The University of Queensland, May 2013.

[70] M. N. Macrossan, H.-H. Chiu, and D. J. Mee. A test facility for hypervelocity rarefied flows. In *AIP Conference Proceedings*, volume 585. American Institute of Physics, 2001. https://doi.org/10.1063/1.1407637.

[71] M. Bugel, P. Reynier, and A. Smith. Survey of european and major isc facilities for supporting mars and sample return mission aerothermodynamics and tests required for thermal protection system and dynamic stability. *International Journal of Aerospace Engineering*, 2011. `https://doi.org/10.1155/2011/937629`.

[72] O. Igra and F. Seiler, editors. *Experimental Methods of Shock Wave Research*, volume 9. Springer, 2016. `https://doi.org/10.1007/978-3-319-23745-9`.

[73] Center of Hypersonics, University of Queensland, . `http://hypersonics.mechmining.uq.edu.au/x2`, accessed September 6, 2018.

[74] R. Morgan. Development of X3, a superorbital expansion tube. *AIAA Journal*, 38, January 2000. `https://doi.org/10.2514/6.2000-558`.

[75] A. Dufrene. Experimental characterization of the LENS expansion tunnel facility including blunt body surface heating. In *49th AIAA Aerospace Sciences Meeting including New Horizons Forum and Aerospace Exposition*, volume 626, January 2011. `https://doi.org/10.2514/6.2011-626`.

[76] CUBRC. `https://www.cubrc.org/`, accessed July 10, 2018.

[77] M. S. Holden. The LENS facilities and experimental studies to evaluate the modeling of boundary layer transition, shock/ boundary layer interaction, real gas, radiation and plasma phenomena in contemporary CFD codes. Technical report, CUBRC, 2010.

[78] G. Yamada, T. Suzuki, H. Takayanagi, and K. Fujita. Development of shock tube for ground testing reentry aerothermodynamics. *Trans. Japan Soc. Aero. Space Sci.*, 54(183):51–61, 2011.

[79] S. Numura, A. Lemal, T. Kawakami, and K. Fujita. Shock-tube investigation on precursor electron ahead of hypersonic shock wave. *2018 AIAA Aerospace Sciences Meeting*, January 2018. `http://doi.org/10.2514/6.2018-0741`.

[80] T. Abe, A. Matsuda, K. Fujita, and S. Sato. Experimental study of nonequilibrium phenomena behind strong shock waves generated in super-orbital reentry flight. SP 17, The Institute of Space and Astronautical Science, February 2003.

[81] M. Bugel, P. Reynier, and A. Smith. Review of european aerodynamics and aerothermodynamics capabilities for sample return missions, January 2009.

[82] A. Chikhaoui and J. M. Félio. ESTHER design kinetic shock-tube for planetary exploration. Technical Report IUSTI-UP ESTHER-TN-01-2011, IUSTI - Université de Provence, October 2011.

[83] M. Lino da Silva, B. Brotas de Carvalho, A. Smith, and L. Marraffa. High-pressure H_2/He/O_2 combustion experiments for the design of the ESTHER shock-tube driver. In *46th AIAA Thermophysics Conference*, number AIAA 2016-4156, 2016. `https://doi.org/10.2514/6.2016-4156`.

[84] M. McGilvray, L. J. Doherty, R. G. Morgan, and D. E. Gildfind. T6: The Oxford University stalker tunnel. In *20th AIAA International Space Planes and Hypersonic Systems and Technologies Conference*, July 2015. `https://doi.org/10.2514/6.2011-626`.

[85] Oxford Thermofluids Institute, Department of Engineering Science. `http://oti.eng.ox.ac.uk/facilities/t6-stalker-tunnel/`, accessed August 20, 2018.

[86] R. J. Stalker and R. W. Besant. A method for production of strong shocks in a gas driven shock tube. Technical Report GD-81, National Research Council, Ottawa, Canada, 1959.

[87] F. K. Lu and D. E. Marren. *Advanced Hypersonic test facilities*, volume 198. Progress in Astronuatics and Aeronautics, January 2002. `https://doi.org/10.2514/4.866678`.

[88] H. G. Hornung. Performance data of the new free-piston shock tunnel at GALCIT. *AIAA 17th Aerospace Ground Testing Conference*, (92-3943), July 1992. `https://doi.org/10.2514/6.1992-3943`.

[89] K. Hannemann, J. M. Schramm, S. Laurence, and S. Karl. Shock tunnel free flight force measurements using a complex model configuration. In *Proceedings of the 8th European Symposium on Aerothermodynamics for Space Vehicles*. German Aerospace Center, 2015.

[90] K. Hannemann. The high enthalpy shock tunnel (heg). In *Workshop on Facilities*. ESA-ESTEC, March 2008.

[91] L. Labracherie, M. Billiotte, and L. Houas. Nonequilibrium determination of temperature profiles by emission spectroscopy. *J. Quant. Spectrosc. Radiat. Transfer*, 54(3):573–579, 1995. `https://doi.org/10.1016/0022-4073(95)00027-I`.

[92] R. O. Foelsche, R. C. Rogers, C.-Y. Tsai, R. J. Bakos, and A. T. Shih. Hypervelocity capability of the HYPULSE shock-expansion tunnel for scramjet testing. In *International Symposium on Shock Waves*, number 23, July 2001.

[93] R. Chue, C.-Y. Tsai, R. Bakos, J. Erdos, and R. Rogers. *NASA's HYPULSE facility at GASL – a dual mode dual driver reflected-shock/expansion tunnel*, volume 198, chapter 3. Progress. Astronaut. Aeronaut., 2002.

[94] C.-Y. Tsai, R. Chue, C. Nicholson, and J. Tyll. Hypervelocity capability of HyPulse shock-tunnel for radiative measurements at Lunar reentries. *47th AIAA Aerospace Sciences Meeting*, (1516), January 2009.

[95] T. Hideyuki, K. Tomoyuki, S. Kazuo, and I. Katsuhiro. Wind tunnel test comparison between JAXA-HIEST and ONERA-S4MA with HYFLEX lifting-body. *7th European Conference for Aeronautics and Space Sciences (EUCASS)*, 2017. `https://doi.org/10.13009/EUCASS2017-187`.

[96] H. Tanno, T. Komuro, K. Sato, K. Itoh, and M. Takahashi. Aerodynamic testing with accelerometers in the high enthalpy shock tunnel HIEST. *46th AIAA Aerospace Sciences Meeting*, (AIAA Paper 2008- 252), January 2008. `https://doi.org/10.2514/6.2008-252`.

[97] K. Reddy, M. Hegde, and V. Jayaram. Material processing and surface reaction studies in free piston driven shock tube. In K. Hannemann and F. Seiler, editors, *The 26th International Symposium on Shock Waves*. Springer-Verlag Berlin Heidelberg, July 2007. `https://doi.org/10.1007/978-3-540-85168-4`.

[98] H. Deconinck, O. Chazot, J. Anthoine, P. Rambaud, C. Asma, S. Paris, M. Playez, V. V. der Haegen, and P. Collin. Aerothermodynamic and aerothermochemical testing in VKI facilities. In *Workshop on Facilities*. ESA-ESTEC, March 2008.

[99] Shock Wave Laboratory, RWTH Aachen University. `http://www.swl.rwth-aachen.de/en/research/test-facilities/hypersonic-shock-tunnel-th2.php`, accessed July 25, 2018.

[100] J. Traineau, C. Pélissier, V. Fomin, A. Kharitonov, V. Lapygin, and V. Gorelov. Review of european facilities for space aerothermodynamics. Technical report, ONERA, May 2003.

[101] P. G. P. Toro, M. A. S. Minucci, J. B. C. Jr, A. C. Oliveira, F. A. A. GomesL, N. MyraboHenry, and T. Nagamatsu. New hypersonic shock tunnel at the laboratory of aerothermodynamics and hypersonics prof. Henry T. Nagamatsu. In *AIP Conference Proceedings*, volume 173, 2008. `https://doi.org/10.1063/1.2931888`.

[102] J. F. de Araujo Martos, I. da Silveira Rêgo, S. N. P. Laiton, B. C. Lima, F. J. Costa, and P. G. de Paula Toro. Experimental investigation of brazilian 14-X B hypersonic scramjet aerospace

vehicle. *International Journal of Aerospace Engineering*, 2017, January 2017. `https://doi.org/10.1155/2017/5496527`.

[103] Center of Hypersonics, University of Queensland, . `http://hypersonics.mechmining.uq.edu.au/t4`, accessed July 25, 2018.

[104] C. Park, K. Chang, and K. Takayama. Shock-tube experiment for carbon nanotude production. In *Symposium on Interdisciplinary Shock Wave Research*, Sendai, Japan, March 2004.

[105] Institute of Mechanics, Chinese Academy of Sciences. `http://english.imech.cas.cn/Equipment/201711/t20171128_186631.html`, accessed July 26, 2018.

[106] Aerospace testing facilities in India, University of Delhi. `http://atfi.dlis.du.ac.in/`, accessed July 25, 2018.

[107] C. Jacobs. *Radiation in low density hypervelocity flows*. PhD thesis, The University of Queensland, 2011.

[108] NASA Official: Nancy Hall. Earth Atmosphere Model, . `https://www.grc.nasa.gov/WWW/K-12/airplane/atmosmet.html`, accessed August 16, 2018.

[109] M. A. Kendall, R. G. Morgan, and P. J. Petrie-Repar. A study of free-piston driven double-diaphragm drivers for expansion tubes. In *AIAA, Aerospace Sciences Meeting & Exhibit*, 1997.

[110] A. L. Smith and D. J. Mee. Drag measurement in flows of 50 microsecond duration. In *Twelfth Australian Fluid Mechanics Conference*, pages 791–794. The University of Sydney, 1995.

[111] M. McGilvray. *Scramjet testing at high enthalpies in expansion tube facilities*. PhD thesis, The University of Queensland, 2008.

[112] S. Gu, R. G. Morgan, and T. J. McIntyre. Study of afterbody radiation during mars entry in an expansion tube. *55th AIAA Aerospace Meeting*, January 2017. `https://doi.org/10.2514/6.2017-0212`.

[113] K. Fujita, S. Sato, T. Abe, and Y. Ebinuma. Experimental investigation of air radiation from behind a strong shock wave. *Journal of Thermophysics and Heat Transfer*, 16(1), January-March 2002. `https://doi.org/10.2514/2.6654`.

[114] G. Yamada, H. Takayanagi, T. Suzuki, and K. Fujita. Shock layer radiation analysis using a hypervelocity shock tube (HVST). *Trans. Japan. Soc. Aero. Space Sci.*, 55(1):37–43, 2012. `https://doi.org/10.2322/tjsass.55.37`.

[115] M. Lino da Silva. Shock tubes simulations. Private communication, 2008.

[116] M. Lino da Silva. Experimental parameters for Titan atmosphere series. Private communication, 2011.

[117] P. Leyland, T. McIntyre, R. Morgan, P. Jacobs, F. Zander, U. Sheikh, T. Eichmann, E. Fahy, O. Joshi, G. Duffa, D. Potter, N. Banerji, J. Mora-Monteros, and V. Marguet. Radiation-ablation coupling for capsule reentry heating via simulation and expansion tube investigations. In *5th European Conference for Aeronautics and Space Sciences (EUCASS)*, July 2013.

[118] K. T. Edquist, A. A. Dyakonov, M. J. Wright, and C. Y. Tang. Aerothermodynamic design of the Mars science laboratory backshell and parachute cone. In *41st AIAA Thermophysics Conference*, 2009. `https://doi.org/10.2514/6.2009-4078`.

[119] A. Gülhan, T. Thiele, F. Siebe, T. Schleutker, and R. Kronen. Post flight analysis of the COMARS+ data and backcover heating of the ExoMars schiaparelli capsule. In *International Planetary Probe Workshop IPPW-15*, The University of Colorado Boulder, USA, June 2018.

[120] NASA Official: Nancy Hall. Mars Atmosphere Model, . `https://www.grc.nasa.gov/www/k-12/airplane/atmosmrm.html`, accessed October 9, 2018.

[121] J. C. Camm and P. H. Rose. Electric arc-driven shock tube. *Physics of Fluids*, 6(5):663, May 1963. `https://doi.org/10.1063/1.1706797`.

[122] S. P. Sharma and C. Parka. Operating conditions of a 60- and 10-cm electric arc-driven shock tube — Part I: The driver. *Journal of Thermophysics and Heat Transfer*, 4(3):259–265, July 1990. `https://doi.org/10.2514/3.175`.

[123] Z. A. Walenta. Optimization of the parameters of a double-diaphragm shock tube. *Archiwm Mechaniki Stosowanej*, 19(5):665–685, 1967.

[124] A. J. Smith. ESTHER performance estimation. Technical Report CR111/11, Fluid Gravity Engineering, October 2011.

[125] R. A. Alpher and D. R. White. Flow in shock tubes with area change at the diaphragm section. *Journal of Fluid Mechanics*, 3(5):457–470, 1958. `https://doi.org/10.1017/S0022112058000124`.

[126] R. J. Stalker and B. P. Edwards. Hypersonic blunt-body flowns in hydrogen-neon mixtures. *Journal of Spacecraft and Rockets*, 35(6):729–735. `http://doi.org/10.2514/2.3399`.

[127] C. M. James, D. E. Gildfind, R. G. Morgan, S. W. Lewis, E. J. Fahy, and T. J. McIntyre. On the current limits of simulating gas giant entry flows in an expansion tube. In *20th AIAA International Space Planes and Hypersonic Systems and Technologies Conferences*, July 2015. `http://doi.org/10.2514/6.2015-3501`.

[128] R. L. Trimpi and N. B. Cohen. A theory for predicting the flow of real gases in shock tubes with experimental verification. Technical Report NACA-TN-3375, National Advisory Committee for Aeronautics, March 1955.

[129] H. Mirels. Attenuation in a shock tube due to unsteady-boundary-layer action. Technical Report 1333, National Advisory Committee for Aeronautics, 1957.

[130] Y. A. Dem'yanov. The influence of the boundary layer on the character of the flow of gas in a tube behind a moving shock wave. Technical Report 796, R.A.E. Library Translation, 1959.

[131] D. A. Spence and B. A. Woods. Boundary layer and combustion effects in shock tube flows. In *Proceedings XI Symposium of the Colston Research Society*. Butterworths Sci. Pub., 1959.

[132] D. A. Spence and B. A. Woods. A review of theoretical treatments of shock tube attenuation. Technical Report TN Aero 2899, R.A.E., 1963.

[133] R. E. Duff. Shock tube performance at low initial pressure. *The Physics of Fluids*, 2(2):207–216, March 1959. `https://doi.org/10.1063/1.1705910`.

[134] G. F. Anderson. Shock-tube testing time. *Journal of the Aerospace Sciences*, 26(3):184–185, 1959. `https://doi.org/0.2514/8.7989`.

[135] A. Roshko. On flow duration in low-pressure shock tubes. *The Physics of Fluids*, (3), 1960. `https://doi.org/10.1063/1.1706147`.

[136] W. J. Hooker. Testing time and contact-zone phenomena in shock-tube flows. *The Physics of Fluids*, 12(4), 1961. `https://doi.org/10.1063/1.1706147`.

[137] H. Mirels. Shock tube test time limitation due to turbulent wall boundary layer. *AIAA Journal*, 2 (84), 1964.

[138] J. A. D. Ackroyd. A study on the running times in shock tubes. Technical report, Department of Aeronautics, Queen Mary College, 1964.

[139] A. Milne. Wall effects in a 1D shock tube. Private communication, July 2017.

[140] A. F. Tasissa, M. Hautefeuille, J. H. Fitek, and R. A. Radovitzky. On the formation of Friedlander waves in a compressed-gas-driven shock tube. In *Proc. R. Soc. A*, volume 472, 2016. `http://doi.org/10.1098/rspa.2015.0611`.

[141] R. G. Morgan and R. J. Stalker. Double diaphragm free piston driven expansion tube. In *Proceedings of the 19th International Symposium on ShockWaves*, pages 1031–1038, July 1991.

[142] P. Petrie-Repar. *Numerical Simulation of Diaphragm Rupture*. PhD thesis, The University of Queensland, December 1997. 1997.

[143] M. Wegener, M. Sutcliffe, and R. Morgan. Optical study of a light diaphragm rupture process in an expansion tube. *Shock Waves*, pages 167–178, April 2000. `https://doi.org/10.1007/s001930050003`.

[144] T. Furukawa, T. Aochi, and A. Sasoh. Expansion tube operation with thin secondary diaphragm. *AIAA Journal*, 45(1), January 2007. `https://doi.org/10.2514/1.23846`.

[145] K. V. Haggard. Free-stream temperature, density and pressure measurements in an expansion tube flow. Technical Note 502-27-01-03, NASA Langley Research Center, Hampton, Va. 23665, October 1973.

[146] G. Wilson. Time-dependent quasi-one-dimensional simulations of high enthalpy pulse facilities. *AIAA Journal*, 92, December 1992.

[147] W. L. Roberts, M. G. Allen, R. Howard, G. Wilson, and R. Trucco. Measurement and prediction of nitric oxide concentration in the HYPULSE expansion tube facility. *AIAA*, 94, June 1994.

[148] R. J. Bakos and R. G. Morgan. Chemical recombination in an expansion tube. *AIAA Journal*, 32 (32), June 1994. `https://doi.org/10.2514/3.12135`.

[149] C. M. James, D. E. Gildfind, S. Lewis, R. G. Morgan, and F. Zander. Implementation of a state-to-state analytical framework for the calculation of expansion tube flow properties. *Shock Waves*, 28:349–377, 2018. `http://doi.org/10.1007/s00193-017-0763-3`.

[150] J. D. A. Jr. *Hypersonic and high temperature gas dynamics*, chapter 11. McGraw-Hill, 1989. ISBN: 1-56347-459-X.

[151] G. G. Chernyi, S. A. Losev, S. O. Macheret, and B. V. Potapkin. *Physical and chemical processes in gas dynamics: physical and chemical kinetics and thermodynamics of gases and plasmas - volume II*, volume 197. Progress in Astronautics and Aeronautics, 2004. ISBN: 1-56347-519-7.

[152] G. G. Chernyi, S. A. Losev, S. O. Macheret, and B. V. Potapkin. *Physical and chemical processes in gas dynamics: cross sections and rate constants - volume I*, volume 196. Progress in Astronautics and Aeronautics, 2004. ISBN: 1-56347-518-9.

[153] K. C. Hendershot. Development of a combustion driven shock tunnel. In *Symposium on Hypersonic Tecniques*. University od Denver Research Insitute, October 1960.

[154] NASA Official: Christopher A. Snyder, 2016. Available online: https://www.grc.nasa.gov/www/CEAWeb/.

[155] M. Martinez-Sanchez. Lecture 14 - Non-equilibrium flows. Available online: `https://ocw.mit.edu/courses/aeronautics-and-astronautics/16-512-rocket-propulsion-fall-2005/lecture-notes/lecture_14.pdf`.

[156] B. D. Henshall. *The Use of Multiple Diaphragms in Shock Tubes*. ARC 18.062. Aeronautical Research Council, Ministry of Supply, Her Majesty's Stationaery Office, 1995.

[157] M. Lino da Silva and J. Beck. Contribution of CO_2 IR radiation to martian entries radiative wall fluxes. In *49th AIAA Aerospace Sciences Meeting Including the New Horizons Forum and Aerospace Exposition*, January 2011. `http://doi.org/10.2514/6.2011-135`.

[158] S. Martinez. Streak camera trigger system. Private communication, .

[159] A. Sedra and K. Smith. *Microelectronic Circuits*, chapter 15.4. Oxford University Press, 2009. ISBN: 978-0195323030.

[160] A. N. Laboratory. Experimental physics and industrial control system engineering software. Available online: `https://www.aps.anl.gov/Epics`.

[161] Xilinx. KC705 Evaluation Board for the Kintex-7 FPGA, July 2018. Available online: `https://www.xilinx.com/support/documentation/boards_and_kits/kc705/ug810_KC705_Eval_Bd.pdf`.

[162] Xilinx. `https://www.xilinx.com/products/silicon-devices/fpga/what-is-an-fpga.html`, accessed August 20, 2018.

[163] Analog Devices. `http://www.analog.com/en/design-center/evaluation-hardware-and-software/evaluation-boards-kits/eval-ad-fmcjesdadc1-ebz.html#`, accessed August 21, 2018.

[164] Analog Devices. `https://wiki.analog.com/resources/fpga/xilinx/fmc/ad-fmcjesdadc1-ebz`, accessed August 21, 2018.

[165] National Instruments. `http://www.ni.com/white-paper/54500/en/`, accessed August 22, 2018.

[166] B. B. de Carvalho. ESTHER streak camera trigger. Private communication, September 2018.

[167] Texas Instruments. IEPE vibration sensor interface reference design for PLC analog input.

[168] J. Karki. Signal conditioning piezoelectric sensors. Application report, Texas Instruments, September 2000. Available online: `https://www.ti.com/lit/an/sloa033a/sloa033a.pdf`.

[169] D. E. Gildfind, P. A. Jacobs, and R. G. Morgan. Vibration isolation in a free-piston driver expansion tube facility. *Shock Waves*, 23(5):431–438, 2013. `http://doi.org/10.1007/s00193-013-0433-z`.

[170] Kistler. *Datasheet: type 601C*, . Available online: `https://www.kistler.com/?type=669&fid=79587&model=document`.

[171] Kistler. Datasheet: type 603B, . Available online: `https://www.process-controls.com/intertechnology/Kistler/pdfs/Pressure_Model_603B1.pdf`.

[172] Kistler. *Datasheet: type 603C*, . Available online: `https://www.kistler.com/?type=669&fid=79737&model=document`.

[173] Kistler. Datasheet: type 701A, . Available online: `https://www.process-controls.com/intertechnology/Kistler/pdfs/Pressure_Model_701A.pdf`.

[174] Kistler. Datasheet: type 7001, . Available online: `http://www.helmar.com.pl/helmar/plik/7001_nn3891.pdf`.

[175] Kistler. *Pressure Sensors for Test and Measurement*, . Available online: `http://kincob.cl/assets/presion.pdf`.

Appendix A

Ideal shock tube equations

A.1 Single diaphragm with constant area shock tubes

Moving normal shock waves

For the one dimensional normal shock wave, the continuity, momentum and energy equations are given, respectively, by

$$\rho_1 u_s = \rho_2(u_s - u_2), \tag{A.1}$$

$$p_1 + \rho_1 u_s^2 = p_2 + \rho_2(u_s - u_2)^2, \tag{A.2}$$

$$h_1 + \frac{1}{2}u_s^2 = h_2 + \frac{1}{2}(u_s - u_2)^2, \tag{A.3}$$

where u_s is the velocity of the gas ahead of the shock wave and $(u_s - u_2)$ is the velocity of the gas behind the shock wave, both relative to the wave.

If the conditions achieved in the shock tube are high enough such that dissociation, ionization or recombination occur, the real gas equation must be used. Otherwise, the calorically perfect gas equation

$$p = \rho R T \tag{A.4}$$

where R is the ideal gas constant, can be applied and the temperature and density ratio equations across the shock wave as a function of the pressure are, respectively, given by

$$\frac{T_2}{T_1} = \frac{p_2}{p_1}\left(\frac{\frac{\gamma_1+1}{\gamma_1-1} + \frac{p_2}{p_1}}{1 + \frac{\gamma_1+1}{\gamma_1-1}\frac{p_2}{p_1}}\right), \tag{A.5}$$

$$\frac{\rho_2}{\rho_1} = \frac{1 + \frac{\gamma_1+1}{\gamma_1-1}\frac{p_2}{p_1}}{\frac{\gamma_1+1}{\gamma_1-1} + \frac{p_2}{p_1}}. \tag{A.6}$$

For a stationary shock, defining the moving shock Mach number as

$$M_s = \frac{u_s}{a_1} \tag{A.7}$$

and incorporating it into equations A.1 through A.3, the pressure ratio across the shock wave is given by

$$\frac{p_2}{p_1} = \frac{2\gamma_1 M_s^2 - (\gamma_1 - 1)}{\gamma_1 + 1}. \tag{A.8}$$

Then, replacing p_2/p_1 into A.5 and A.6, the temperature and density ratios, as function of M_s, can be written as

$$\frac{T_2}{T_1} = \left[1 + \frac{2\gamma_1}{\gamma_1 + 1}(M_s^2 - 1)\right]\left[\frac{2 + (\gamma_1 - 1)M_s^2}{(\gamma_1 + 1)M_s^2}\right], \tag{A.9}$$

$$\frac{\rho_2}{\rho_1} = \frac{(\gamma_1 + 1)M_s^2}{2 + (\gamma_1 - 1)M_s^2}. \tag{A.10}$$

As mentioned before, a shock wave propagating into a stagnant gas induces a mass motion with velocity u_2 behind the wave. Substituting equations A.4, A.5, A.6 and 3.1 into A.1 and simplifying, the mass-motion velocity is given by

$$u_2 = \frac{a_1}{\gamma_1}\left(\frac{p_2}{p_1} - 1\right)\sqrt{\frac{\frac{2\gamma_1}{\gamma_1+1}}{\frac{p_2}{p_1} + \frac{\gamma_1 - 1}{\gamma_1 + 1}}}. \tag{A.11}$$

Region 3 contains the driver gas processed by the unsteady expansion wave. From the relation between the head and tail of the expansion wave and since $p_3 = p_2$, the velocity in this region can be obtained by the following relation:

$$u_3 = a_4\left(\frac{2}{\gamma_4 - 1}\right)\left[1 - \left(\frac{p_3}{p_1}\frac{p_1}{p_4}\right)^{\frac{\gamma_4 - 1}{2\gamma_4}}\right]. \tag{A.12}$$

Reflected shock wave

The continuity, momentum and energy equations for the reflected shock can be written, respectively, as

$$\rho_2(u_r + u_2) = \rho_5 u_r \tag{A.13}$$

$$p_2 + \rho_2(u_r + u_2)^2 = p_5 + \rho_5 u_r^2 \tag{A.14}$$

$$h_2 + \frac{1}{2}(u_r + u_2)^2 = h_5 + \frac{1}{2}u_r^2 \tag{A.15}$$

where $(u_r + u_2)$ is the velocity of the gas ahead of the shock wave and u_r the velocity of the gas behind the shock wave, both relative to the wave.

Incident and reflected expansion waves

For a simple centred expansion wave, the speed of sound ratio is given by

$$\frac{a}{a_4} = 1 - \frac{\gamma - 1}{2}\left(\frac{u}{a_4}\right) \tag{A.16}$$

and because $a = \sqrt{\gamma R T}$, the temperature ratio is

$$\frac{T}{T_4} = \left[1 - \frac{\gamma - 1}{2}\left(\frac{u}{a_4}\right)\right]^2 \tag{A.17}$$

and also, since the flow is isentropic, $p/p_4 = (\rho/\rho_4)^\gamma = (T/T_4)^{\gamma/(\gamma-1)}$, the pressure and density ratios are, respectively, given by

$$\frac{p}{p_4} = \left[1 - \frac{\gamma - 1}{2}\left(\frac{u}{a_4}\right)\right]^{\frac{2\gamma}{\gamma-1}}, \tag{A.18}$$

$$\frac{\rho}{\rho_4} = \left[1 - \frac{\gamma - 1}{2}\left(\frac{u}{a_4}\right)\right]^{\frac{2}{\gamma-1}}. \tag{A.19}$$

A.2 Single diaphragm with variable area shock tubes

To expand the ratios from equation 3.8, applying the Riemann invariant across a unsteady isentropic wave results in

$$\frac{p_a}{p_b} = \left(\frac{\rho_a}{\rho_b}\right)^\gamma = \left(\frac{a_a}{a_b}\right)^{\frac{2\gamma}{\gamma-1}} = \left[\frac{2 + (\gamma - 1)M_b}{2 + (\gamma - 1)M_a}\right]^{\frac{2\gamma}{\gamma-1}} \tag{A.20}$$

while the relation applied across a steady isentropic process results in

$$\frac{p_a}{p_b} = \left(\frac{\rho_a}{\rho_b}\right)^\gamma = \left(\frac{a_a}{a_b}\right)^{\frac{2\gamma}{\gamma-1}} = \left[\frac{2 + (\gamma - 1)M_b^2}{2 + (\gamma - 1)M_a^2}\right]^{\frac{\gamma}{\gamma-1}}. \tag{A.21}$$

Applying equation A.20 across the non-steady expansion wave (regions $4 - 3a$ and $3b - 3$) and equation A.21 through the supersonic nozzle, equation 3.8 yields

$$\frac{p_4}{p_1} = \left\{\left[\frac{2 + (\gamma_4 - 1)M_{3a}}{2}\right]\left[\frac{2 + (\gamma_4 - 1)M_{3b}^2}{2 + (\gamma_4 - 1)M_{3a}^2}\right]^{1/2}\left[\frac{2 + (\gamma_4 - 1)M_3}{2 + (\gamma_4 - 1)M_{3b}}\right]\right\}^{\frac{2\gamma_4}{\gamma_4-1}} \frac{p_2}{p_1}. \tag{A.22}$$

Since the previous relation involves M_3, M_{3a} and M_{3b} as well as p_4/p_1 and p_2/p_1, additional equations are needed. The overall area ratio in the transition section can be written as

$$\frac{A_4}{A_1} = \frac{M_{3b}}{M_{3a}}\left[\frac{2 + (\gamma_4 - 1)M_{3a}^2}{2 + (\gamma_4 - 1)M_{3b}^2}\right]^{\frac{\gamma_4+1}{2(\gamma_4-1)}}. \tag{A.23}$$

Expanding M_3 in the same way as p_4/p_1 in equation 3.8

$$M_3 = \frac{u_3}{a_3} = \frac{u_2}{a_3} = \frac{\frac{u_2}{a_1}}{\frac{a_3}{a_1}} = \frac{\frac{u_2}{a_1}}{\frac{a_3}{a_{3b}}\frac{a_{3b}}{a_{3a}}\frac{a_{3a}}{a_4}\frac{a_4}{a_1}}, \tag{A.24}$$

substituting for the sound velocity ratios across the unsteady expansion waves and through the supersonic nozzles from equations A.20 and A.21, respectively,

$$M_3 = \frac{\frac{u_2}{a_1}}{\left[\frac{2+(\gamma_4-1)M_{3b}}{2+(\gamma_4-1)M_3}\right]\left[\frac{2+(\gamma_4-1)M_{3a}^2}{2+(\gamma_4-1)M_{3b}^2}\right]^{1/2}\left[\frac{2}{2+(\gamma_4-1)M_{3a}}\right]\frac{a_4}{a_1}} \tag{A.25}$$

and reorganizing, M_3 yields

$$M_3 = \left\{ \frac{a_1}{u_2}\frac{a_4}{a_1} g^{\frac{\gamma_4-1}{2\gamma_4}} - \frac{\gamma_4-1}{2} \right\}^{-1}. \tag{A.26}$$

The quantity g is the equivalence factor defined by Alpher and White [125] and it is equivalent to

$$g = \left\{ \left[\frac{2+(\gamma_4-1)M_{3a}^2}{2+(\gamma_4-1)M_{3b}^2}\right]^{1/2} \left[\frac{2+(\gamma_4-1)M_{3b}}{2+(\gamma_4-1)M_{3a}}\right] \right\}^{\frac{2\gamma_4}{\gamma_4-1}}. \tag{A.27}$$

$\bar{k}$ is defined by Walenta [123] and is given by

$$\bar{k} = \left[\frac{2+(\gamma_4-1)M_{3a}^2}{\gamma_4+1}\right]^{\frac{1}{2}} \left[\frac{\gamma_4+1}{2+(\gamma_4-1)M_{3a}}\right]. \tag{A.28}$$

A.3 Double diaphragm shock tube

Shock tube with cross section area reduction at both diaphragms

Firstly, the value u_2/a_1 must be iterated for required M_{s1} and then, knowing a_1/a_7 and recalling that $u_2 = u_3$ across the contact surface, $u_3/a_7 = (u_2/a_1)(a_1/a_7)$ is found. Thus, in order to obtain the given velocity ratio u_3/a_7, the primary shock Mach number M_{s7} (and consequently the pressure ratio p_{11}/p_7), for which the pressure ratio p_{11}/p_3 reaches its minimum value, is calculated. Therefore, the optimum value of the primary shock Mach number M_{s7} is calculated from the condition, that for given u_3/a_7, the pressure ratio p_{11}/p_3 reaches its minimum for that value of M_{s7}, that is,

$$\frac{\partial}{\partial M_{s7}}\left[\ln\left(\frac{p_{11}}{p_3}\right)\right] = 0, \tag{A.29}$$

where the pressure ratio p_{11}/p_3 can be expressed as

$$\frac{p_{11}}{p_3} = \frac{p_{11}}{p_8}\frac{p_8}{p_6}\frac{p_6}{p_5}\frac{p_5}{p_4}\frac{p_4}{p_3} \tag{A.30}$$

being p_{11}/p_8 given by

$$\frac{p_{11}}{p_8} = \left[k - \frac{\gamma_{11}-1}{\gamma_7+1}\frac{a_7}{a_{11}}\left(M_{s7} - \frac{1}{M_{s7}}\right)\right]^{-\frac{2\gamma_{11}}{\gamma_1{}^{1-1}}}, \tag{A.31}$$

where

$$k = \left[\frac{2+(\gamma_{11}-1)M_{10}^2}{\gamma_{11}+1}\right]^{\frac{1}{2}} \left[\frac{\gamma_{11}+1}{2+(\gamma_{11}-1)M_{10}}\right] \tag{A.32}$$

and M_{10} can be calculated from

$$\frac{1}{M_{10}}\left[\frac{2}{\gamma_{11}+1}\left(1+\frac{\gamma_{11}-1}{2}M_{10}^2\right)\right]^{\frac{\gamma_{11}+1}{2(\gamma_{11}-1)}} = \frac{A_{11}}{A_7}. \tag{A.33}$$

As explained before, across the contact surface, there is a continuity of the pressure, thus

$$\frac{p_8}{p_6} = 1. \tag{A.34}$$

Moreover, the relation between p_6 and p_5 can be written as

$$\frac{p_6}{p_5}=\frac{\gamma_7+1}{\gamma_7-1}\left(\frac{2\gamma_7}{\gamma_7-1}X^2-1\right)^{-1}, \tag{A.35}$$

where X, an adimensionalized variable,

$$X=\frac{U_R+u_6}{a_6}$$

can be calculated from

$$\left(X^2+\frac{2}{\gamma_7-1}\right)\left(\frac{2\gamma_7}{\gamma_7-1}X^2-1\right)-\left(\frac{2}{\gamma_7-1}\right)^2\frac{1}{M_5^2}\left(1+\frac{\gamma_7+1}{2}M_6X-X^2\right)^2=0 \tag{A.36}$$

and

$$M_6=\frac{M_{s7}^2-1}{\left[\left(\gamma_7M_{s7}^2-\frac{\gamma_7-1}{2}\right)\left(\frac{\gamma_7-1}{2}M_{s7}^2+1\right)\right]^{1/2}}. \tag{A.37}$$

Similarly to M_{10}, M_5 can be calculated from

$$\frac{1}{M_5}\left[\frac{2}{\gamma_7+1}\left(1+\frac{\gamma_7-1}{2}M_5^2\right)\right]^{\frac{\gamma_7+1}{2(\gamma_7-1)}}=\frac{A_7}{A_1}. \tag{A.38}$$

Then, the pressure ratios p_5/p_4 and p_4/p_3 are given by

$$\frac{p_5}{p_4}=\left[\frac{2}{\gamma_7+1}\left(1+\frac{\gamma_7-1}{2}M_5^2\right)\right]^{-\frac{\gamma_7}{\gamma_7-1}}, \tag{A.39}$$

$$\frac{p_4}{p_3}=\left[\frac{\gamma_7+1}{2}-\frac{\gamma_7-1}{2}\frac{u_3/a_7}{a_4/a_7}\right]^{-\frac{2\gamma_7}{\gamma_7-1}} \tag{A.40}$$

where

$$\frac{a_4}{a_7}=\frac{a_6}{a_7}\frac{a_5}{a_6}\frac{a_4}{a_5} \tag{A.41}$$

can be calculated from

$$\frac{a_6}{a_7}=\frac{1}{M_6}\frac{u_6}{a_7}=\frac{1}{M_6}\left[\frac{2}{\gamma_7+1}\left(M_{s7}-\frac{1}{M_{s7}}\right)\right], \tag{A.42}$$

$$\frac{a_5}{a_6}=\left\{\frac{\frac{\gamma_7+1}{2}X}{\left[\left(\gamma_7X^2-\frac{\gamma_7-1}{2}\right)\left(\frac{\gamma_7-1}{2}X^2+1\right)\right]^{\frac{1}{2}}}\right\}^{-1} \tag{A.43}$$

and

$$\frac{a_4}{a_5}=\left[\frac{2}{\gamma_7+1}\left(1+\frac{\gamma_7-1}{2}M_5^2\right)\right]^{\frac{1}{2}}. \tag{A.44}$$

To obtain the required primary shock Mach number M_{s7}, the pressure ratio p_{11}/p_7 can be calculated from

$$\frac{p_{11}}{p_7}=\frac{p_{11}}{p_8}\frac{p_8}{p_6}\frac{p_6}{p_7}, \tag{A.45}$$

where

$$\frac{p_6}{p_7}=\frac{2\gamma_7}{\gamma_7+1}\left(M_{s7}^2-\frac{\gamma_7-1}{2\gamma_7}\right). \tag{A.46}$$

All the above equations are found in Walenta [123] and are valid if the following conditions are satisfied:

a) the flow in region 8 is sonic or supersonic:

$$M_{s7} \geq \frac{\gamma_7+1}{\gamma_{11}+1}\frac{a_{11}}{a_7}\frac{k}{2} + \left[1 + \left(\frac{\gamma_7+1}{\gamma_{11}+1}\frac{a_{11}}{a_7}\frac{k}{2}\right)^2\right]^{1/2}; \tag{A.47}$$

b) the primary shock wave reflects from the second diaphragm as a shock:

$$M_6 \geq M_5; \tag{A.48}$$

c) the flow in region 3 is sonic or supersonic:

$$\frac{u_3}{a_7} \geq \frac{a_4}{a_7}; \tag{A.49}$$

d) no liquefaction of gas, that is, conversion of the gas to liquid state, can occur in any region of the flow.

The regions where liquefaction is likely to occur are 8 and 3. Using the following equations is possible to check if this phenomenon occurs in each of those regions, applying, respectively:

$$\frac{T_8}{T_{11}} = \left[k - \frac{\gamma_{11}-1}{\gamma_7+1}\frac{a_7}{a_{11}}\left(M_{s7} - \frac{1}{M_{s7}}\right)\right]^2, \tag{A.50}$$

$$\frac{T_3}{T_7} = \left[\frac{\gamma_7-1}{2}\frac{a_4}{a_7} - \frac{\gamma_7-1}{2}\frac{u_2}{a_7}\right]^2. \tag{A.51}$$

Shock tube with cross-section area reduction only at the first diaphragm

For this case, the pressure ratio p_{11}/p_3 necessary for obtaining the velocity ratio u_3/a_7 can be expressed as

$$\frac{p_{11}}{p_3} = \frac{p_{11}}{p_8}\frac{p_8}{p_6}\frac{p_6}{p_3}. \tag{A.52}$$

The values for p_{11}/p_8 and p_8/p_6 can be calculated from the same expressions (equations A.31 to A.34) and the ratio p_6/p_3 is modified to

$$\frac{p_6}{p_3} = \left[1 - \frac{\gamma_7-1}{2}\left(\frac{a_3/a_7}{a_6/a_7} - M_6\right)\right]^{-\frac{2\gamma_7}{\gamma_7-1}}, \tag{A.53}$$

where M_6 and a_6/a_7 can also be computed from equations A.37 and A.42.

The pressure ratio p_{11}/p_7

$$\frac{p_{11}}{p_7} = \frac{p_{11}}{p_8}\frac{p_8}{p_6}\frac{p_6}{p_7} \tag{A.54}$$

necessary to obtain the required primary shock Mach number M_{s7} can be calculated from equations A.31, A.34 and A.46.

After applying equations A.52 and A.34, the optimum value of the primary shock Mach number M_{s7} can be calculated from the same condition as in the case from section 3.1.3, by manipulating the following condition:

$$\frac{\partial}{\partial M_{s7}}\left(\ln\frac{p_6}{p_3}\right) = -\frac{d}{dM_{s7}}\left(\ln\frac{p_{11}}{p_8}\right). \tag{A.55}$$

The above equations are valid if the condition from equation A.47 is verified. On the other hand, the conditions represented by equations A.48 and A.49 are no longer necessary.

To verify if liquefaction occurs in region 8, equation A.50 can be applied together with equations A.31 and A.33. For region 3, the expression is altered to

$$\frac{T_3}{T_7} = \left\{\left[1 - \frac{\gamma_7 - 1}{2}\left(\frac{u_3/a_7}{a_6/a_7} - M_6\right)\right]\frac{a_6}{a_7}\right\}^2, \tag{A.56}$$

which can be combined with equations A.53 and A.46.

The minimum lengths for this configuration are given by:

$$\left(\frac{x_{11}}{x_7}\right)_{min} = \left(\frac{M_{10}+1}{4}\right)\frac{a_{11}}{a_7}\left(\frac{1 - \frac{M_6-1}{M_{s7}}\frac{a_6}{a_7}}{\frac{a_6}{a_7}}\right)\left\{\frac{\gamma_{11}+1}{k[(\gamma_{11}-1)M_{10}+2]}\left[k - \frac{\gamma_{11}-1}{\gamma_7+1}\frac{a_7}{a_{11}}\left(M_{s7} - \frac{1}{M_{s7}}\right)\right]\right\}^{\frac{\gamma_{11}+1}{2(\gamma_{11}-1)}}, \tag{A.57}$$

$$\left(\frac{x_7}{x_{test}}\right)_{min} = \left(\frac{\gamma_7+1}{2(\gamma_7-1)}\right)\frac{a_6}{a_7}\frac{\left[1 - \frac{\gamma_7-1}{2}\left(\frac{u_3/a_7}{a_6/a_7} - M_6\right)\right]^{\frac{\gamma_7+1}{2(\gamma_7-1)}}}{\left[\frac{2}{(\gamma_7-1)M_{s7}^2+1}\right]\frac{u_3}{a_7}}. \tag{A.58}$$

.

Appendix B

Results for a test atmosphere with 78% N_2, 21% O_2 and 1% Ar at 10 Pa and a driver pressure of 600 bar

B.1 Properties

In the following tables, for a single diaphragm shock tube, state 10 corresponds to state 3a, state 9 to 3b and state 8 to 3, in figure 3.2. States 6 and 7 occur on the intermediate section and, therefore, only exist for double diaphragm shock tubes.

Table B.1: State 11 - driver section initial properties.

Conf.	Constant heat ratio (γ_{11})	Density (ρ_{11}, in kg/km^3)	Velocity (u_{11}, in m/s)	Mach number (Ma$_{11}$)	Pressure (p_{11}, in bar)	Temperature (T_{11}, in K)
1	1.358	18.2996	0	0	600	2800
2	1.358	18.2996	0	0	600	2800
3	1.358	18.2996	0	0	600	2800
4	1.358	18.2996	0	0	600	2800
5	1.358	18.2996	0	0	600	2800
6	1.358	18.2996	0	0	600	2800

Table B.2: State 10.

Conf.	Constant heat ratio (γ_{10})	Density (ρ_{10}, in g/m^3)	Velocity (u_{10}, in m/s)	Mach number (Ma$_{10}$)	Pressure (p_{10}, in bar)	Temperature (T_{10}, in K)
1	1.420	7260.304	1807.143	1.000	167.152	1969.794
2	1.355	16694.490	190.420	0.092	530.462	2712.419
3	1.420	7260.304	1807.143	1.000	167.152	1969.794
4	1.355	16694.490	190.420	0.092	530.462	2712.419
5	1.420	7260.304	1807.143	1.000	167.152	1969.794
6	1.368	14239.668	516.047	0.255	427.332	2563.939

Table B.3: State 9.

Conf.	Constant heat ratio (γ_9)	Density (ρ_9, in g/m^3)	Velocity (u_9, in m/s)	Mach number (Ma$_9$)	Pressure (p_9, in mbar)	Temperature (T_9, in K)
1	1.420	6728.453	1807.729	1.000	154884.797	1969.436
2	1.392	9497.368	1930.980	1.000	254366.461	2289.559
3	1.420	6728.453	1807.729	1.000	154884.797	1969.436
4	1.392	9497.368	1930.980	1.000	254366.461	2289.559
5	1.420	6728.453	1807.729	1.000	154884.797	1969.436
6	1.403	8378.958	1888.921	1.000	213134.028	2175.437

Table B.4: State 8.

Conf.	Constant heat ratio (γ_8)	Density (ρ_8, in g/m^3)	Velocity (u_8, in m/s)	Mach number (Ma$_8$)	Pressure (p_8, in mbar)	Temperature (T_8, in K)
1	1.492	19.104	6911.088	10.184	58.970	264.344
2	1.497	22.670	7582.350	11.087	70.824	267.550
3	1.515	718.778	5028.550	4.565	5757.319	685.955
4	1.509	854.486	5619.253	4.853	7591.457	760.835
5	1.517	675.796	5094.631	4.692	5252.567	665.619
6	1.512	770.473	6476.120	5.745	6476.120	719.826

Table B.5: State 7 - primary shock wave properties.

Conf.	Constant heat ratio (γ_7)	Density (ρ_7, in g/m^3)	Velocity (u_7, in m/s)	Mach number (Ma$_7$)	Pressure (p_7, in mbar)	Temperature (T_7, in K)
1	-	-	-	-	-	-
2	-	-	-	-	-	-
3	1.667	16.401	6857.095	6.726	102.266	300
4	1.667	17.454	7629.444	7.483	108.832	300
5	1.667	14.592	6943.330	6.810	90.987	300
6	1.667	15.773	7413.332	7.271	98.357	300

Table B.6: State 6 - intermediate post-shock properties.

Conf.	Constant heat ratio (γ_6)	Density (ρ_6, in g/m^3)	Velocity (u_6, in m/s)	Mach number (Ma$_6$)	Pressure (p_6, in mbar)	Temperature (T_6, in K)
1	-	-	-	-	-	-
2	-	-	-	-	-	-
3	1.667	61.501	5028.501	1.273	5757.319	4503.906
4	1.667	66.242	5619.199	1.286	7591.457	5513.719
5	1.667	54.802	5094.581	1.275	5252.567	4611.320
6	1.667	59.685	5454.157	1.282	6476.120	5220.323

Table B.7: State 2 - working post-shock properties.

Conf.	Constant heat ratio (γ_2)	Density (ρ_2, in g/m^3)	Velocity (u_2, in m/s)	Mach number (Ma$_2$)	Pressure (p_2, in mbar)	Temperature (T_2, in K)
1	1.136	2.014	6911.027	3.790	58.970	6174.228
2	1.153	2.081	7582.297	3.828	70.824	6601.483
3	1.163	2.031	11141.117	3.764	153.013	11119.339
4	1.163	2.074	12452.330	3.806	190.889	12261.954
5	1.172	2.128	13383.744	3.844	220.163	12934.020
6	1.174	2.113	13608.180	3.845	227.576	13108.937

Table B.8: State 1 - main shock wave properties.

Conf.	Constant heat ratio (γ_1)	Density (ρ_1, in g/m^3)	Velocity (u_1, in m/s)	Mach number (Ma$_1$)	Pressure (p_1, in mbar)	Temperature (T_1, in K)
1	1.4	0.116	7333.903	21.124	0.100	300
2	1.4	0.116	8030.562	23.131	0.100	300
3	1.4	0.116	11816.780	34.036	0.100	300
4	1.4	0.116	13191.223	37.995	0.100	300
5	1.4	0.116	14156.375	40.775	0.100	300
6	1.4	0.116	14391.877	41.545	0.100	300

B.2 Wave diagrams

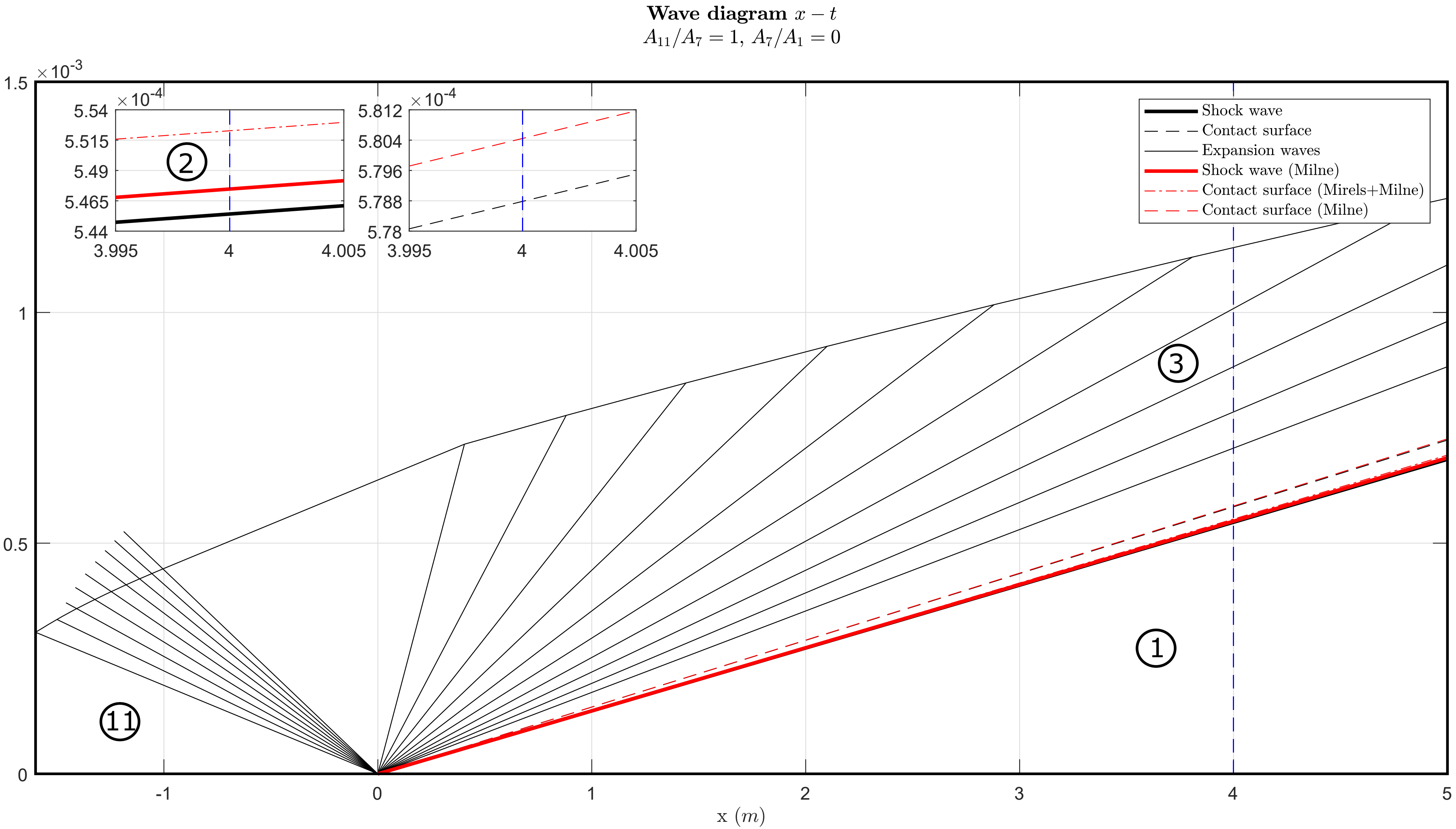

Figure B.1: Wave diagram - single diaphragm shock tube with constant area.

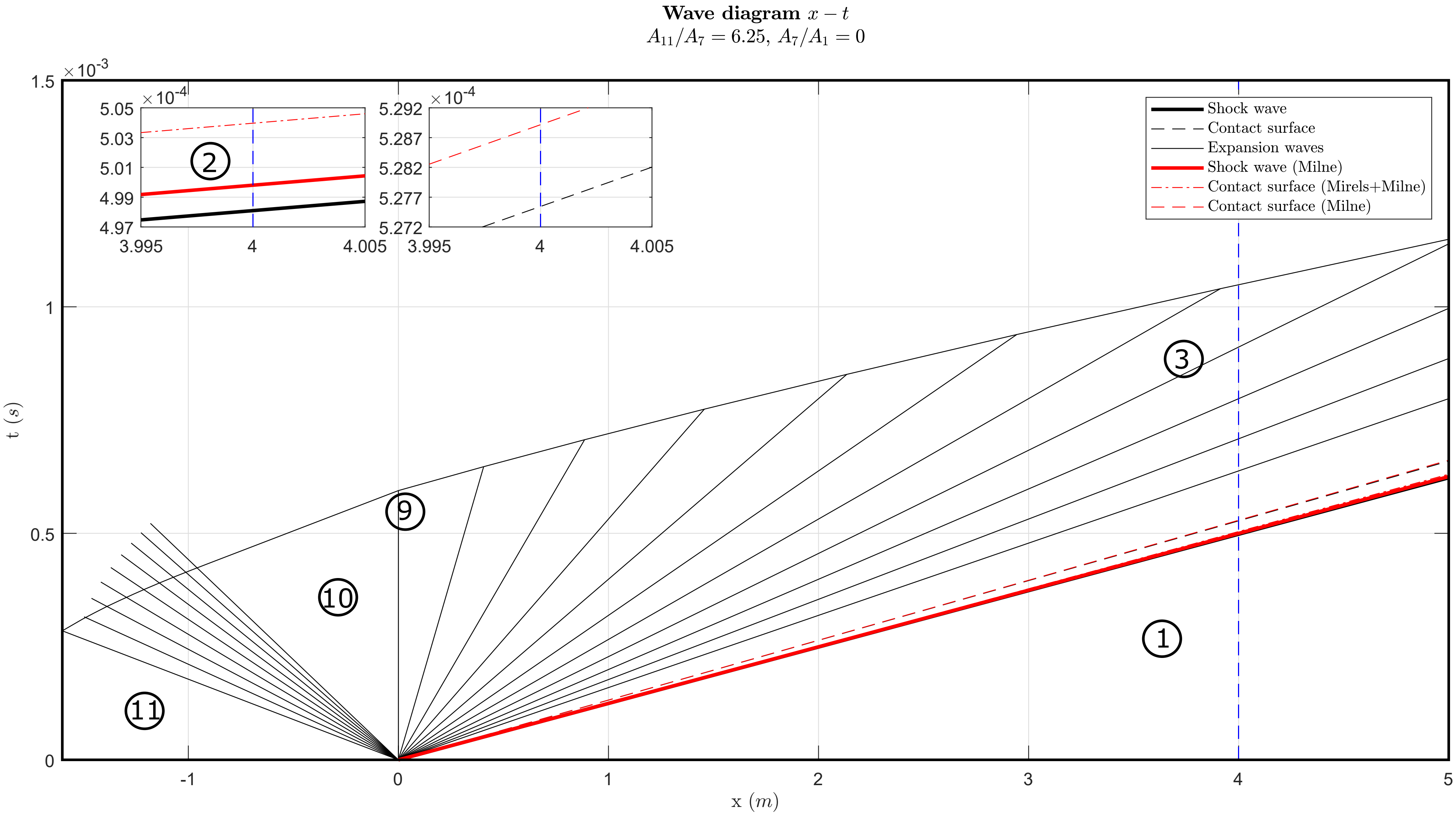

Figure B.2: Wave diagram - single diaphragm shock tube with variable area.

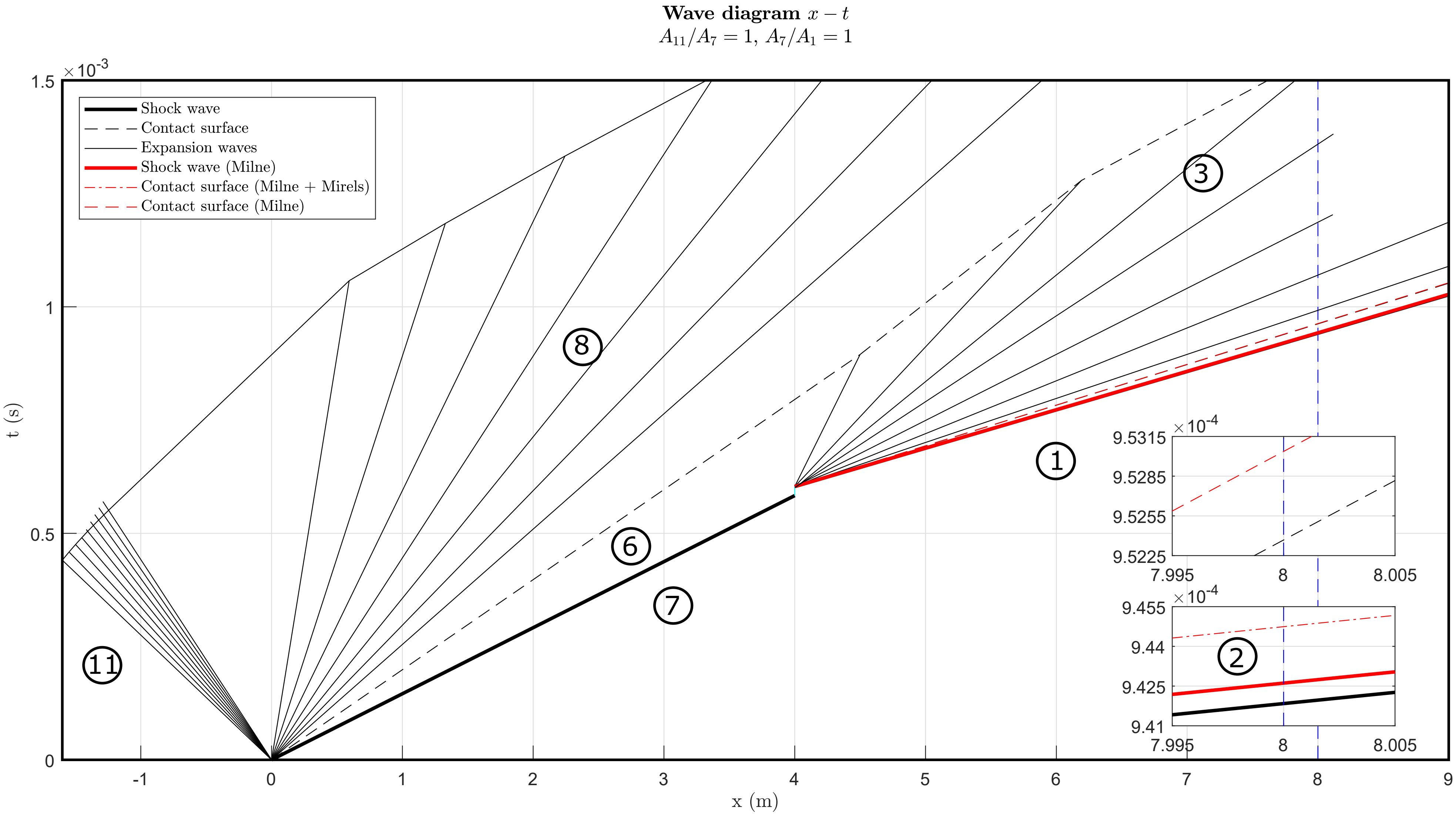

Figure B.3: Wave diagram - double diaphragm shock tube with no cross-section area reductions.

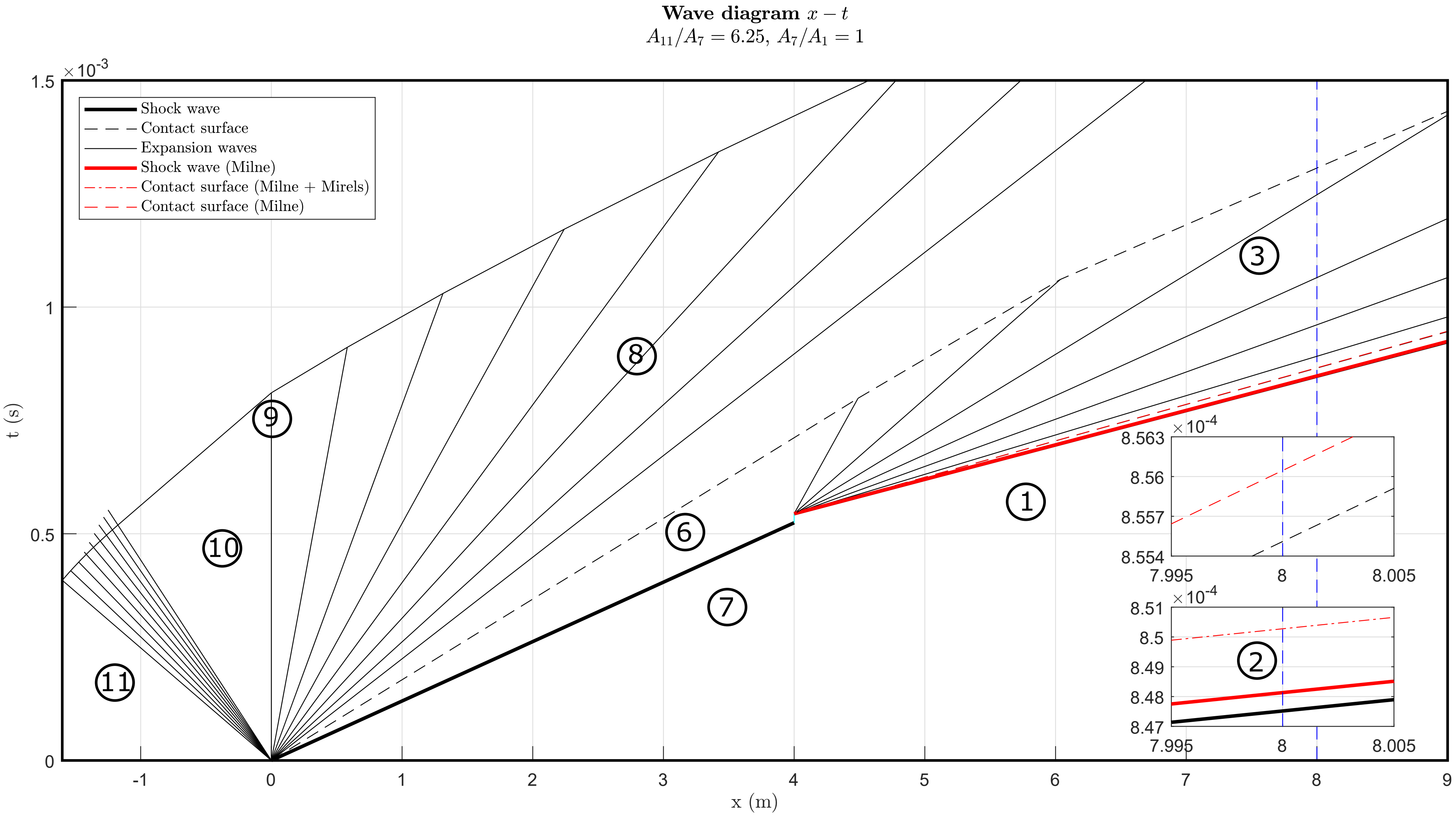

Figure B.4: Wave diagram - double diaphragm shock tube with cross-section area reductions at the first diaphragm.

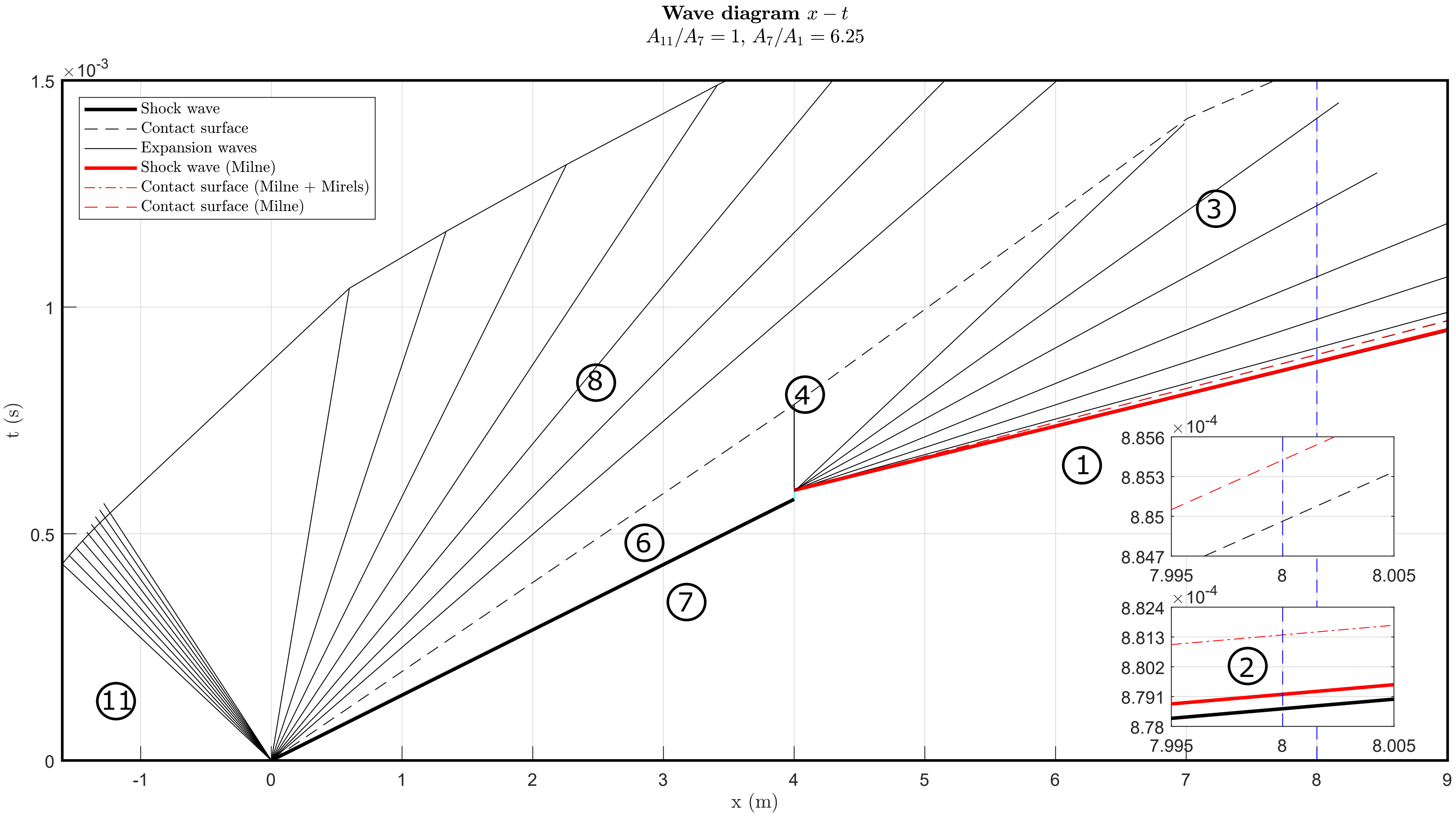

Figure B.5: Wave diagram - double diaphragm shock tube with cross-section area reductions at the second diaphragm.

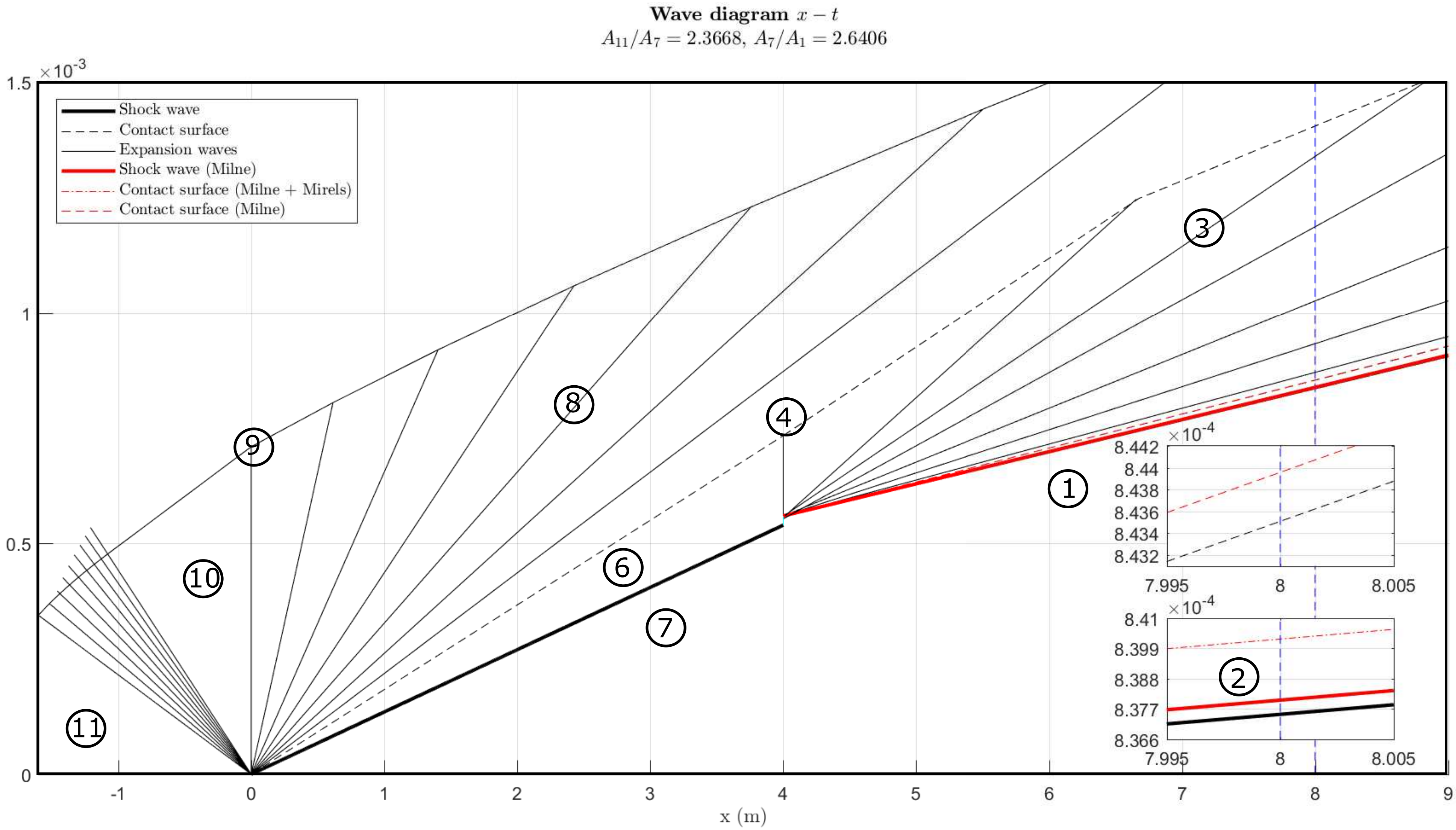

Figure B.6: Wave diagram - double diaphragm shock tube with cross-section area reductions at both diaphragms.

Appendix C

ESTHER performance envelope

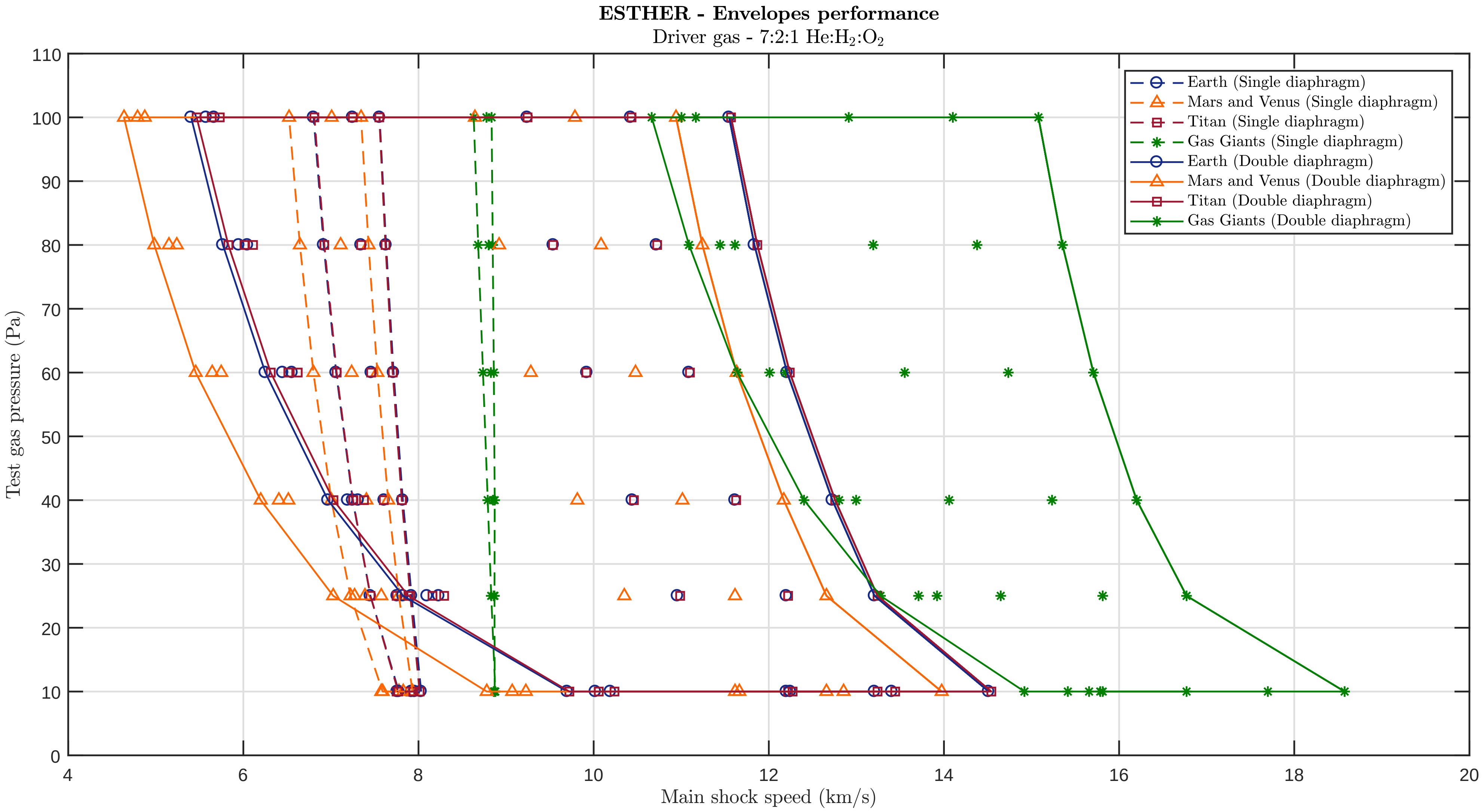

Figure C.1: ESTHER shock tube envelope performance for different planetary atmospheres.

Appendix D

Trigger system

D.1 Signal conditioning system schematic

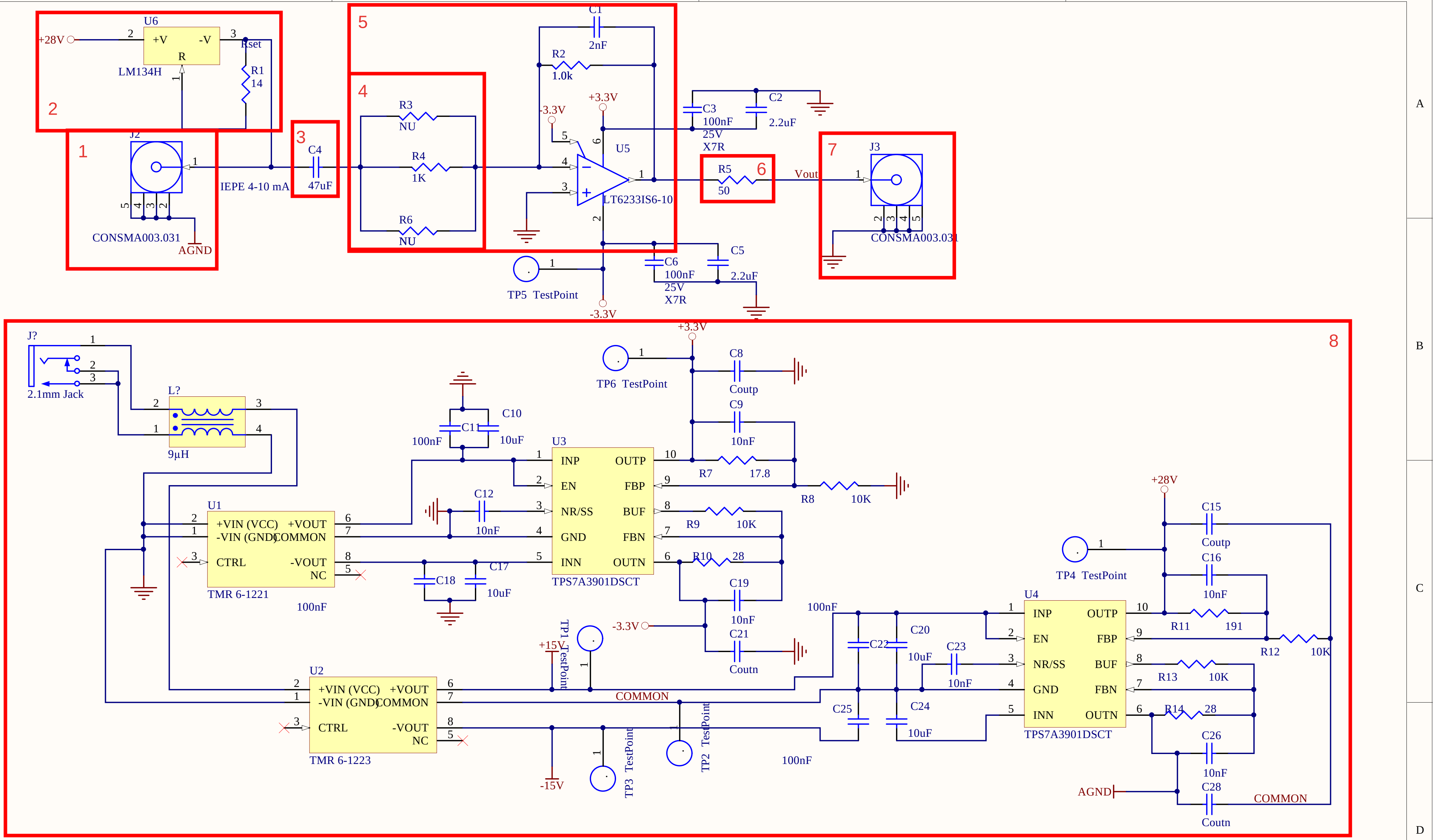

Title **ESTHER STREAK CAMERA TRIGGER**

IPFN-IST
Address1
Address2
Address3
Address4

Size: A4 Number: 1 Revision: 0

Date: 24.08.2018 Time: 11:00:12 Sheet 2 of 2

File: C:\Users\Public\Documents\Altium\Projects\PCB_Project\Eurocard VME 3U (3.937 x 6.299 inches).schdoc